Negative Ions and Operation Modes in Capacitively Coupled RF Oxygen Discharges

I n a u g u r a l d i s s e r t a t i o n

zur

Erlangung des akademischen Grades eines

Doktors der Naturwissenschaften

der

Mathematisch-Naturwissenschaftlichen Fakultät

der

Ernst-Moritz-Arndt-Universität Greifswald

vorgelegt von

Christian Küllig

geboren am 02. Juni 1984

in Schwerin

Greifswald, 25. April 2013

Dekan:	Prof. Dr. K. Fesser
1. Gutachter:	Prof. Dr. J. Meichsner
2. Gutachter:	Prof. Dr N. St. J. Braithwaite
Tag der Promotion:	10.09.2013

"Wissenschaft ist keine Frage der Nützlichkeit,
sondern des Fortschritts!"

Bernhard Victor Christoph Carl von Bülow
(* 12.11.1923 † 22.8.2011)

Contents

List of Figures

List of Notations

All quantities are in International System (SI).

$k_{<a,d,r,c>}$	rate coefficients for attachment, detachment, recombination and charge transfer
$\tilde{n}_{<index>}$, $n_{<index>}$	line integrated density, absolute density
$< index > = O_2^+$, O^-, O_2^-, $-$, e^-, O, X, Δ	positive molecular ion, negative atomic ion, negative molecular ion, negative ion, electron, atomic oxygen, molecular ground state ($O_2\left(X^3\Sigma_g^-\right)$), molecular metastable state ($O_2\left(a^1\Delta_g\right)$) oxygen

Symbol	Name / Explanation	Unit & if applicable Value
a	spatial axial distance	$[a] = \mathrm{m}$
a_{mwi}	optical axis position, 20 mm above the RF electrode	$a_{\mathrm{mwi}} = 20\,\mathrm{mm}$
α	electronegativity	$[\alpha] = 1$
A_{l}	laser beam cross section	$[A_{\mathrm{l}}] = \mathrm{m}^2$
$\vec{B}$	magnetic flux	$[\vec{B}] = \mathrm{T}$
b_+	ion mobility	$[b_+] = \mathrm{m}^2/(\mathrm{V}\cdot\mathrm{s})$
f_{mwi}	microwave frequency	$f_{\mathrm{mwi}} = 160.28\,\mathrm{GHz}$
f_{rf}	radio frequency	$f_{\mathrm{rf}} = 13.56\,\mathrm{MHz}$
c	speed of light	$c = 2.99792458 \times 10^8\,\mathrm{m/s}$
D_{a}	ambipolar diffusion coefficient	$[D_{\mathrm{a}}] = \mathrm{m}^2/\mathrm{s}$
d_{coll}	mean RF sheath thickness	$[d_{\mathrm{coll}}] = \mathrm{m}$
ΔL_{opt}	difference of the optical mean free path length	$[\Delta L_{\mathrm{opt}}] = \mathrm{m}$
$\Delta\Phi$	phase shift of the MWI	$[\Delta\Phi] = \mathrm{rad}$
δn_{e}	detached electron density	$[\delta n_{\mathrm{e}}] = \mathrm{m}^{-3}$
e	elementary charge	$e = 1.60217733 \times 10^{-19}\,\mathrm{C}$
e	Euler's number	$\mathrm{e} = 2.718281828459\ldots$
$\vec{E}$	electrical field strength	$[\vec{E}] = \mathrm{V/m}$
$\lvert\vec{E}_0\rvert$	amplitude of the electrical field strength	$[\lvert\vec{E}_0\rvert] = \mathrm{V/m}$
E_{l}	laser energy	$[E_{\mathrm{l}}] = \mathrm{J}$
ϵ_0	electric field constant	$\epsilon_0 = 8.854187817 \times 10^{-12}\,\mathrm{C}/(\mathrm{V}\cdot\mathrm{m})$
h	Planck constant	$h = 6.6260755 \times 10^{-34}\,\mathrm{J\,s}$

Symbol	Name / Explanation	Unit & if applicable Value
i	imaginary unit	$\mathrm{i}^2 = -1$
I_l	laser intensity	$[I_\mathrm{l}] = \mathrm{W/m^2}$
$j_{+\mathrm{rf}}$	ion current density	$[j_{+\mathrm{rf}}] = \mathrm{A/m^2}$
$j_{+\mathrm{Bohm}}$	Bohm current density	$[j_{+\mathrm{Bohm}}] = \mathrm{A/m^2}$
k_w	wavenumber	$[k_\mathrm{w}] = \mathrm{1/m}$
κ	ionization degree	$[\kappa] = 1$
k_B	Boltzmann constant	$k_\mathrm{B} = 1.380658 \times 10^{-23}\,\mathrm{J/K}$
$\tilde{K}_\mathrm{a}$	effective attachment rate coefficient	$[\tilde{K}_\mathrm{a}] = \mathrm{s^{-1}}$
$\tilde{K}_\mathrm{d}$	effective detachment rate coefficient	$[\tilde{K}_\mathrm{d}] = \mathrm{s^{-1}}$
L_d	diffusion length	$[L_\mathrm{d}] = \mathrm{m}$
λ_e	mean free path length of electrons	$[\lambda_\mathrm{e}] = \mathrm{m}$
λ_+	mean free path length of positive ions	$[\lambda_+] = \mathrm{m}$
λ_D	electron DEBYE length	$[\lambda_\mathrm{D}] = \mathrm{m}$
λ_l	laser wavelength	$\lambda_\mathrm{l} = 532\,\mathrm{nm}$
λ_mwi	microwave wavelength	$\lambda_\mathrm{mwi} = 1.87\,\mathrm{mm}$
m_e	electron mass	$m_\mathrm{e} = 9.1093897 \times 10^{-31}\,\mathrm{kg}$
m_+	positive ion mass	$[m_+] = \mathrm{kg}$
n_c	critical electron density, corresponding to microwave frequency	$n_\mathrm{c} = 3.2 \times 10^{20}\,\mathrm{m^{-3}}$
n_e	electron density	$[n_\mathrm{e}] = \mathrm{m^{-3}}$
n_eP	electron afterglow peak density	$[n_\mathrm{eP}] = \mathrm{m^{-3}}$
n_-	negative ion density	$[n_-] = \mathrm{m^{-3}}$
n_{-0}	steady state negative ion density	$[n_{-0}] = \mathrm{m^{-3}}$
n_n	neutral particle density	$[n_\mathrm{n}] = \mathrm{m^{-3}}$
n_+	positive ion density	$[n_+] = \mathrm{m^{-3}}$
n_{+0}	positive ion density at the sheath edge	$[n_{+0}] = \mathrm{m^{-3}}$
ν_l	laser frequency $\nu_\mathrm{l} = c/\lambda_\mathrm{l}$	$\nu_\mathrm{l} = 5.6352 \times 10^{14}\,\mathrm{Hz}$
N_air	refraction index of air	$N_\mathrm{air} = 1$
N_pl	refraction index of the plasma	$[N_\mathrm{pl}] = 1$
ω_e	electron plasma frequency	$[\omega_\mathrm{e}] = \mathrm{Hz}$
ω_mwi	angular frequency of the MWI	$\omega_\mathrm{mwi} = 2\pi\, f_\mathrm{mwi}$
ω_rf	angular radio frequency	$\omega_\mathrm{rf} = 2\pi\, f_\mathrm{rf}$

Symbol	Name / Explanation	Unit & if applicable Value
ω_0	difference frequency of the microwave interferometer	$\omega_0 = 30\,\mathrm{MHz}$
$\bar{\phi}_{\mathrm{rf}}$	mean RF sheath voltage	$[\bar{\phi}_{\mathrm{rf}}] =$ V
φ_0	phase shift of the electrical field	$[\varphi_0] =$ rad
R	curvature radius of the wave front	$[R] =$ m
R_{l}	laser beam radius	$R_{\mathrm{l}} = 6.5\,\mathrm{mm}$
t	time	$[t] =$ s
τ	time constant	$[\tau] =$ s
τ_{d}	ambipolar diffusion time constant	$[\tau_{\mathrm{d}}] =$ s
τ_{e}	electron plasma time scale	$[\tau_{\mathrm{e}}] =$ s
T_{e}	electron temperature	$[T_{\mathrm{e}}] =$ K
T_{ion}	ion temperature	$[T_{\mathrm{ion}}] =$ K
T_-	negative ion temperature	$[T_-] =$ K
T_{n}	neutral gas temperature	$[T_{\mathrm{n}}] =$ K
T_+	positive ion temperature	$[T_+] =$ K
T_{room}	room temperature	$[T_{\mathrm{room}}] =$ K
V_{bias}	self-bias voltage	$[V_{\mathrm{bias}}] =$ V
v_{phase}	phase velocity	$[v_{\mathrm{phase}}] =$ m/ s
w	Gaussian beam radius of the electrical field, $\lvert\vec{E}_0\rvert/\mathrm{e}$	$[w] =$ m
$\tilde{w}$	measured effective beam radius $1/\sqrt{2}\cdot\lvert\vec{E}_0\rvert/\mathrm{e}$	$[\tilde{w}] =$ m
w_0	beam waist	$w_0 = 5\,\mathrm{mm}$
$w_{0,\mathrm{h}}$	beam waist of the horn antenna	$w_{0,\mathrm{h}} = 4.5\,\mathrm{mm}$
z	microwave propagation direction	$[z] =$ m

Abbreviations

CCRF	Capacitively coupled radio frequency
DC	Direct current
EEDF	Electron energy distribution function
FMC	Fluid model calculations
ICCD	Intensified Charge Coupled Device
ICRF	Inductively coupled radio frequency
MWI	Microwave interferometry / Microwave interferometer
Nd:YAG	Neodymium-doped yttrium-aluminum garnet
PIC-MCC	Particle In Cell - Monte Carlo Collision
PTE	Partial thermodynamic equilibrium
PLL	Phase lock loop
RF	Radio frequency
PROES	Phase resolved optical emission spectroscopy
TROES	Temporal resolved optical emission spectroscopy

1. Introduction

Nonthermal low-pressure plasmas generated by radio frequency (RF) discharges have been widely studied in fundamental plasma research and applied in low temperature plasma technologies [1–3]. Their frequency ranges between the ion and electron plasma frequencies, consequently the electrons can follow the high-frequency electric field instantaneously. In contrast to electrons, the movement of heavy ions is determined by their mass and radio frequency, where the ions more or less follow the time-averaged electric field.

RF discharges can be distinguished in terms of the RF power coupling and electron heating. In principle two RF discharge configurations can be identified, the capacitively coupled RF (CCRF) and the inductively coupled RF (ICRF) discharge [2]. The latter is characterized by high plasma densities and an inductor electrode, which does not have to be placed in the vacuum chamber. The electron heating mechanism of the ICRF discharge is based on an induced toroidal electrical field parallel to the coil. Consequently, there are no electrical fields perpendicular to the electrode surface. The situation is different for CCRF discharges, where an electrical field occurs perpendicular to the electrode surface. Hence, it develops an RF sheath, which separates the neutral plasma bulk from the surrounding walls. Through the sheath the plasma is heated and causes a particle and energy flux to the plasma and the electrodes, respectively. In geometrically asymmetric CCRF discharges a DC self bias occurs, which influences the particle flux as well as the mean ion energy.

Dual frequency discharge have received increased interest in recent research, for a number of reasons. Firstly, they can control the self bias voltage electrically. Secondly, the phase between both frequencies controls the mean ion energy at the electrode separately from the ion flux [4–6].

Low-pressure RF discharges can be also combined with an external magnetic field. In the case of RF magnetron discharges an asymmetric CCRF discharge configuration with magnetic field lines parallel to the powered electrode surface and perpendicular to the electric field in the RF sheath provides an electron confinement due to the $\vec{E} \times \vec{B}$ drift. The locally increased plasma density in the drift region in front of the electrode enlarges the positive ion flux to the target material on RF electrode and the sputter yield of target atoms, respectively. Another discharge configuration is known as the helicon discharge. At low-pressure, the radio frequency is coupled by antennas of a specific geometry, and together with an external magnetic field helicon modes are excited. The resonant electron heating by helicon waves results in high density plasma.

Especially electronegative plasmas such as oxygen and fluorocarbons are widely used in plasma technologies, e. g., plasma treatment of material surfaces (chemical modification,

cleaning, etching, patterning) [7], thin film deposition [8, 9], ozone production [10–12], exhaust gas cleaning and as electron capture in gas circuit-breaker [13]. The difficulty with these plasmas is however that they represent an extraordinary many-particle system, which shows drastic changes in its physical and chemical properties compared to the usual plasmas generated with electropositive gases [14]. Nevertheless, the electronegative plasmas are not completely understood. Therefore, the fundamental research of low temperature plasmas uses the CCRF discharges as a model system to investigate nonthermal, weakly ionized plasmas. A major reason for this is that the CCRF discharge can be easily realized by two parallel electrodes, where one is driven with the RF voltage. The generated alternating RF sheaths in front of the electrodes realize the main energy input, due to the electrical fields perpendicular to the electrode surface. For the most asymmetric CCRF discharges, the RF sheath in front of the powered electrode is strongly positively charged, while the electrode surface is negatively charged. However, the sign of the charging of the surface depends on the surface ratio of the powered to the grounded electrode, and alternates with the RF frequency of 13.56 MHz. This strongly influences the electron heating mechanisms, as well as the plasma parameters.

A main field in experimental plasma physics is therefore the investigation of such complex multi-component plasmas, which contain electrons, multiple negative and positive ions, as well as neutral transient and stable molecules. The electrons play a significant role because of their low mass, which means they can instantaneously follow the electrical RF field. Therefore, they strongly influence the dynamics of and in particular the heating mechanism within the RF sheath [15–18]. Hence, the most important tasks include the measurement of the electron energy distribution function EEDF, the mean electron energy and the electron density. The standard method for the electron density measurement is the Langmuir probe diagnostics, which was introduced in 1924 by Langmuir and Mott-Smith [19]. However, although it has a good spatial resolution, the electrical probe analysis is a strongly invasive diagnostics and can drastically affect the plasma properties [20–22], e. g., due to electron depletion [23]. Moreover, complex model assumptions are necessary to interpret the probe characteristics and to determine the plasma parameters such as the electron density [24, 25]. Probe measurements in reactive plasmas such as oxygen particularly cause difficulties, where for instance high resistance layers can be formed on the probe surface [7, 26–29], or negative ions can occur [26, 30, 31].

Especially the negative ions are an important species in electronegative processing plasmas [32] and they distinguish the electronegative plasmas from the more common electropositive plasmas. In particular, negative ions significantly determine the charged species balance and the electron energy distribution function, by electron attachment and by detachment processes and ion-ion recombination. The formation of negative ions by attachment of electrons to radicals can furthermore contribute to the growth of particles [33], or even reduce the charge of dust grains in plasmas [34]. The negative (hydrogen) ions are also important for the neutral beam heating of fusion plasmas after acceleration and collision detachment of the negative ions [35–37]. Moreover, the negative ions can even cause instabilities, which significantly change the plasma parameters, e. g., floating and plasma potential, excitation processes in the form of optical emission and charge carrier

densities [38–45]. Another effect of the negative ions is that they can strongly influence the plasma dynamics, e. g., the electron heating [18,46], as well as the change of the properties of the plasma boundary sheath [47], or the formation of double layers [48–51]. Moreover, the negative ions are produced at the electrode or in the RF plasma sheath region, e. g., during the sheath collapse phase [52]. They may contribute to additional "secondary electrons" due to detachment reactions inside the sheath [18] and consequently can affect the quasineutral plasma bulk. Another example of the effect of negative ions is given by plasmas with electronegative organic molecules. Here, the ion-molecule reactions are extended by charge transfer reactions with negative ions and result in the formation of larger molecules and small clusters [53].

Consequently, it is crucial to have information on the negative ions as well as the electronegativity, which is the fraction of the negative ion and the electron densities in electronegative plasmas. The analysis of the electrons and negative ions is therefore in the focus of interest in this thesis, because of their influence on heating mechanisms, the discharge development and the generation of modes. The standard method to determine the localized negative ion density is the measurement of the electron current increase within the volume of the pulsed laser beam, by means of a Langmuir probe and laser photodetachment technique [49,50,54–78]. Apart from the problems using probe diagnostics mentioned above, other effects have to be taken into account, e. g., the evaluation of the probe signal [71] and the interaction of the laser pulse with the probe material [79,80]. In addition the interaction of the probe with different laser beam volumes influences the shape and height of the detachment signal [56, 59, 81]. Other less common and more difficult ways to measure the negative ions include the usage of absorption spectroscopy [64, 82], and crossed-beam photodetachment technique [83]. Furthermore, it is possible to use the photodetachment technique in combination with opto-galvanic effects [60], with resonance microwave cavity method [60, 84], using the whole vacuum chamber and involving the more spatially localized hair-pin probe technique [85].

This contribution will extensively discuss the results of investigation on an oxygen plasma produced in an asymmetric CCRF discharge, and compare it to an electropositive argon plasma. Oxygen was chosen in this study because it is a reactive and electronegative plasma, which contains many species such as charged particles such as electrons, positive (O_2^+, O^+) and negative ions (O^-, O_2^-, O_3^-), as well as neutral particles such as radicals ($O\left(^3P\right)$) and metastable excited species such as molecular metastable oxygen $O_2\left(a^1\Delta_g\right)$. Hence, it is a multi-species system, but it does not contain too many species, so that it is suitable as a molecular model system. Therefore, it is still possible to distinguish between different reaction channels and the relevance of collisional partner.

This thesis present a novel non-invasive method to measure the electron and negative ion density by means of microwave interferometry (MWI) and simultaneously laser photodetachment. This combination was realized for the first time in CCRF oxygen discharge. These diagnostics provide an excellent approach to study the steady state as well as the dynamical behavior of the electron and negative ion densities. The microwave interferometry directly allows for measuring the line integrated electron density by measuring the phase shift of the microwave due to the change in electron density without any model as-

sumption. One major advantage of this diagnostics is its application in electronegative and reactive low-pressure plasmas [86]. The microwave interferometry in the high gigahertz range is a standard method in fusion research, with its high amount of electrons [87–92]. However, under the requirements of low-temperature, low-density plasmas such as the CCRF discharges, the usage of the microwave interferometry in the high gigahertz range is not standard. This is due to its low electron density of about $10^{16}\,\mathrm{m}^{-3}$ and its consequent rather low phase shift of 0.01° to 1°. These conditions therefore require a high quality microwave interferometer and careful experimental design. The microwave interferometry (90 GHz) in combination with simulations are used to determine the electron density in the plume of Hall thruster [93, 94]. Furthermore, microwave interferometry has been applied for electron density analysis in RF plasmas with a wavelength of 1 mm [95–97], leading to a spatial resolution of about 10 mm. This was an improvement compared to previous experiments [98–100]. The temporal resolution of Niemöller *et al.* [95] is about 1 ms using the advantages of a heterodyne interferometer, e. g., higher sensitivity and increased stability [89, 101, 102]. A better temporal resolution was achieved by Krämer *et al.* [97] but with a pure homodyne interferometer, which influences the phase measurement. A much better temporal resolution in combination with a suitable axial spatial resolution is crucial to measure and study fast dynamics in the RF discharge, e. g., the effect due to instabilities, and the resolution of fast changes in the early plasma afterglow or even to measure the electron density increase due to laser photodetachment. For the latter it is important to resolve the detachment signal in the microsecond range [59, 62, 72]. Because of these high requirements the combination microwave interferometry and laser photodetachment diagnostics has not often been realized. The few examples known from the literature as in include fluorocarbon plasmas [103] and sulfur hexafluoride [104] using a photodetachment and microwave cavity technique, or chlorine plasma (ICRF) [105, 106] and SF_6/Ar RF plasma (ICRF) [107] by 80 GHz microwave interferometry and in a C_4F_8 plasma (ICRF) using a microwave resonance probe [108]. Greenberg *et al.* [55] have shown very briefly and exemplarily that it is possible to measure negative ions in a hollow cathode discharge in nitrogen trifluoride by microwave interferometry and laser photodetachment.

Nevertheless, there are no detailed investigations and published results on the combination of microwave interferometry in the millimeter range and laser photodetachment in low-pressure oxygen RF plasmas, with a suitable spatial and temporal resolution. This contribution will therefore intensively discuss the analysis of the CCRF oxygen plasmas regarding the density of electrons and negative ions, their dynamics and consequently their influence on the reactions and processes in the discharge. The used 160 GHz microwave interferometer, the design of the microwave guiding components and the description of the free space propagation are a very important issues (Article I). The optimization of the setup is achieved with best spatial and temporal resolutions in first parameter studies (Article I) and further comprehensive electron density analysis regarding the pressure dependence on the RF sheath (Article II). The non-invasive measurement of the negative ions by laser photodetachment and microwave interferometry is an important part of this work. This measurement is done both in the steady state phase (Article III) and temporally resolved for the electron and negative ion densities in the pulsed discharge, to

investigate the dynamical behavior (Article IV). Beside the dynamics, the stability of the oxygen discharge regarding the appearance of instabilities is investigated as well (Article V, VI). Finally, the experiment is also compared with first simulations (Article VI). [1]

[1] For thesis articles I to VI please see Chapter 6

2. Capacitively coupled RF discharge and applied diagnostics

The experimental setup was based on a capacitively coupled radio frequency (CCRF) discharge, which is one of the most frequently used types of low-pressure discharges. The produced plasma is a typical low-temperature, non-thermal and weakly ionized plasma with an ionization degree κ (2.1), which ranges from 10^{-6} to 10^{-4}.

$$\kappa = \frac{n_\mathrm{e}}{n_\mathrm{e} + n_\mathrm{n}} \tag{2.1}$$

Where n_n is the neutral particle and n_e the electron density in an electropositive plasma. An important time scale (τ_e) is defined by the electron plasma frequency (2.2).

$$\frac{1}{\tau_\mathrm{e}} = \omega_\mathrm{e} = \sqrt{\frac{n_\mathrm{e}\, e^2}{m_\mathrm{e}\, \epsilon_0}} \tag{2.2}$$

The electron plasma frequency is in the order of 6 GHz if one assumes a typical electron density of $10^{16}\,\mathrm{m}^{-3}$ in CCRF plasmas. Consequently, the electrons are able to follow the RF field at 13.56 MHz due to their low mass ($\omega_\mathrm{e} \gg \omega_\mathrm{rf}$) and they are mainly influencing the dynamics of the CCRF discharge. It is therefore of great interest in fundamental plasma physics research to analyze the electrons and especially to determine their density (n_e) and energy distribution in CCRF discharges.

The simplest CCRF discharge configuration consists of two plane parallel electrodes. One of these electrodes is powered with the radio frequency voltage, which is usually at 13.56 MHz (ISM band)[1], and the other electrode is on ground potential. One can distinguish between symmetric and asymmetric CCRF discharges, depending on the area ratio of the powered to the grounded electrode. In contrast to symmetric CCRF discharges, where both areas are equal, for asymmetric CCRF discharges one electrode area is greater than the other. Despite of equal electrode areas the unconfined RF discharges are mostly asymmetric. Here, the effective grounded electrode area is larger than the powered electrode, which is due to the grounded RF electrode shielding and chamber wall. This fact and the capacitively coupling, which does not allow loss of charge within a RF cycle, causes a DC self-bias voltage V_bias. Because of the higher mobility of the electrons in comparison to the positive ions, all surfaces are negatively charged against the plasma potential. As the fluxes of negative and positive charge carriers have to compensate over one RF period, a negative DC self-bias voltage shifts the RF voltage at the powered electrode and increases

[1] ISM band is the Industrial, Scientific and Medical band of frequencies, the usage of which is regulated by the Vollzugsordnung für Funkdienste (VO-Funk) in Germany.

the mean sheath voltage. In particular, the enlarged positive ion current at the powered electrode compensates the electron current at the grounded electrode over one RF cycle. The sheath voltage at the powered electrode is RF modulated. The dynamics of the RF sheath is mainly determined by the electron dynamics in the sheath. Consequently, the electron front oscillates in dependence on the variation of the electrode and the plasma potential. This results in the strong modulation of the space charges, the self-consistent electric field, the sheath potential, as well as the sheath thickness [1]. Hence, the electrons are heated during the sheath expansion phase and they are able to excite, dissociate and ionize neutrals. Consequently, the electron energy distribution function (EEDF) in the CCRF plasma mainly determines the elementary processes and kinetics in the plasma [3]. In specific cases the approximation of a local Partial Thermodynamic Equilibrium (PTE) can be applied for nonequilibrium plasmas which implies the definition of different kinetic temperatures for the electrons, ions and neutrals (2.3).

$$T_e \gg T_{ion} \approx T_n \approx T_{room} \tag{2.3}$$

Usually, the low pressure plasma of a CCRF discharge does not show a Maxwellian EEDF. In some cases of a CCRF discharge a Bi-Maxwellian electron energy distribution has been found and consequently two electron temperatures have been defined [24, 109, 110]. A rough estimation for the mean electron energy provides the application of an effective electron temperature.

Molecular CCRF plasmas represent multi-species plasmas which contain electrons, positively and negatively charged ions, and neutrals such as molecules, atoms and radicals. Furthermore, the heavy plasma particles may contain different internal energy due to excitation and energy transfer processes. Plasmas containing only electrons and positive ions besides the neutral species are known as electropositive plasmas. If the plasma in addition contains negative ions, it is called an electronegative plasma. Electronegative plasmas are an extraordinary many particle system, which can drastically change its physical and chemical properties in comparison to electropositive plasmas [14]. Hence, the investigation of the negative ions, and especially the knowledge of their density, production and loss channels (attachment, detachment, recombination, charge transfer), gives a comprehensive insight into the mechanisms of electronegative CCRF discharges.

2.1. Vacuum apparatus and discharge configuration – Article I

This experiment uses a 13.56 MHz capacitively coupled RF (CCRF) discharge, which is schematically shown in Fig. 2.1. The setup mainly consist of a cylindrical stainless steel vacuum vessel with a height and diameter of 400 mm each. The chamber is pumped by a 200 l/ s turbo pump to a base pressure of 5×10^{-5} Pa. The process pressure is maintained by a 16 m^3/ h stage rotary pump and is varied in the range from 5 to 100 Pa. All experiments in this work are performed with argon (Ar) or oxygen (O_2) as process gases, which are admitted into the reactor via a mass flow controller with a constant gas flow rate of

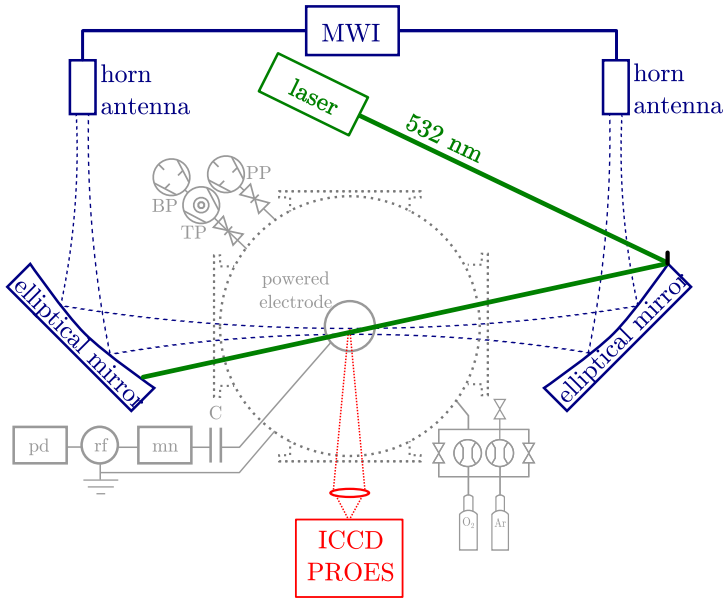

Fig. 2.1.: Sketch of the experimental setup in top view, consisting of the vacuum chamber with the vacuum equipment for low-pressure plasma processing, the RF power supply (rf) and the matching network (mn). Additional pulsing of the discharge is realized by a pulse delay generator (pd). The applied diagnostics consist of the 160.28 GHz Gaussian beam microwave interferometer (MWI) for electron density measurement, the Nd:YAG laser for photodetachment and the ICCD camera for phase resolved optical emission spectroscopy (PROES).

5 sccm. The discharge configuration consists of a stainless steel electrode with a diameter of 100 mm. The electrode is water-cooled and powered by a RF generator at 13.56 MHz and a fully tunable π-type matching network. The shielding of the RF electrode and the chamber walls are on ground potential. Because of the capacitively coupling and the large area ratio between the grounded and the powered electrode, a strong asymmetric RF plasma is generated. This results in a negative self-bias voltage at the powered electrode. The results presented in this work were achieved using RF power values between 5 and 150 W and corresponding self-bias voltages between -100 and -600 V.

The CCRF discharge was investigated by different diagnostics, see Fig. 2.1. The optical emission of excited atomic oxygen at 844 nm was measured by RF phase resolved optical emissions spectroscopy (PROES). This diagnostic technique has been discussed in detail in [16–18]. To measure the electron density in the bulk plasma the Gaussian beam microwave interferometry was applied at 160 GHz, which is discussed section 2.2 below. The laser photodetachment of the electrons from the negative ions and the measurement of their density was realized by the simultaneous usage of a Nd:YAG laser[2] (sec. 2.3) and the microwave interferometer.

[2]neodymium-doped yttrium-aluminum garnet laser

2.2. Gaussian beam microwave interferometry (MWI) – Article I

Microwave interferometry (MWI) was used to determine the density of the electrons in the plasma bulk of the CCRF discharge. One advantage of this method is that it is non-invasive and allows direct measurement of the line-integrated electron density by the phase shift of the microwave due to the change in the electron density without any model assumptions. The electron density is directly coupled with the plasma frequency (2.2) and, therefore, with the refractive index N_{pl} of the plasma. Hence, there is a phase difference $\Delta\Phi$ between the microwave beam passing the plasma and the microwave beam not passing the plasma, which differ in phase velocity. In the following, the phase shift difference is derived using the dispersion relation for electromagnetic wave propagation in non-magnetized and collision free plasma [111]

$$k_{\mathrm{w}}(\omega) = \frac{1}{c}\sqrt{\omega_{\mathrm{mwi}}^2 - \omega_{\mathrm{e}}^2} \tag{2.4}$$

which directly couples the phase shift over the refractive index (2.5) of the plasma with the electron plasma frequency (2.2) and therefore with the electron density.

$$N_{\mathrm{pl}} = \frac{c}{v_{\mathrm{phase}}} = c \cdot \frac{k_{\mathrm{w}}}{\omega_{\mathrm{mwi}}} = \sqrt{1 - \frac{\omega_{\mathrm{e}}^2}{\omega_{\mathrm{mwi}}^2}} \tag{2.5}$$

Where ω_{mwi} (2.6) is the angular frequency of the microwave interferometer, which defines a critical density n_{c}, until the microwave can pass the plasma and is not reflected.

$$\omega_{\mathrm{mwi}} = \sqrt{\frac{n_{\mathrm{c}}\, e^2}{m_{\mathrm{e}}\, \epsilon_0}} \tag{2.6}$$

Consequently (2.2) and (2.6) change (2.5) to:

$$N_{\mathrm{pl}} = \sqrt{1 - \frac{n_{\mathrm{e}}}{n_{\mathrm{c}}}} \tag{2.7}$$

The different refractive indexes of air and plasma lead to differences in the optical path length ΔL_{opt}, which is connected to the phase difference via

$$\frac{\Delta\Phi}{2\pi} = \frac{\Delta L_{\mathrm{opt}}}{\lambda_{\mathrm{mwi}}} \tag{2.8}$$

The difference of the optical path length ΔL_{opt} is defined by:

$$\Delta L_{\mathrm{opt}} = \int_{z_1}^{z_2} (N_{\mathrm{air}} - N_{\mathrm{pl}})\, \mathrm{d}z \tag{2.9}$$

Finally, the phase shift $\Delta\Phi$ can be estimated by means of (2.8), (2.7), (2.9), and $N_{\mathrm{air}} = 1$.

$$\Delta\Phi = \frac{2\pi}{\lambda_{\mathrm{mwi}}} \int_{z_1}^{z_2} \left(1 - \sqrt{1 - \frac{n_{\mathrm{e}}}{n_{\mathrm{c}}}}\right) \mathrm{d}z \tag{2.10}$$

Assuming that weakly ionized plasmas have a much lower electron density than critical electron density ($n_e \ll n_c$) it follows (2.11):

$$\Delta\Phi = \frac{\pi}{n_c \lambda_{mwi}} \underbrace{\int n_e(z)\,dz}_{\tilde{n}_e} \tag{2.11}$$

Where λ_{mwi} is the microwave wavelength, and n_c the critical density, which is given for a specific chosen microwave frequency f_{mwi}. Hence, the phase shift is directly proportional to the line integrated electron density $\tilde{n}_e$ without any model assumption. The choice of the diagnostic frequency (f_{mwi}) is strongly coupled to the following points:

- The microwave frequency has to be much higher than the electron plasma frequency, which is due to $n_c \gg n_e$.
- The phase shift resolution has to be high enough, to resolve the expected low electron densities down to $10^{14}\,m^{-3}$.
- The free space propagation can be described under the requirements of the Gaussian beam propagation theory.

Establishing microwave interferometry in low-pressure CCRF plasmas needs to fulfill the requirement of measuring electron densities ranging between 10^{15} and $10^{16}\,m^{-3}$ [60, 112, 113], which corresponds to phase shifts between 0.03° and 0.3°. The detection of such small phase shifts is one of the great challenges of this diagnostics. The electron densities are connected to plasma frequencies in the range of 2 to 20 GHz. In this frequency range, microwave interferometers are commercially available [113–115]. In this low frequency range it is not possible to describe the microwave free space propagation by Gaussian beam theory. Full wave physics, including the boundary conditions, e. g., walls, need to be involved here. A special microwave interferometer was applied, with a frequency of $f_{mwi} = 160.28\,GHz$ and a wavelength of about $\lambda_{mwi} = 1.87\,mm$. The critical density of $n_c = 3.2 \times 10^{20}\,m^{-3}$ satisfies ($n_c \gg n_e$). Moreover, at this frequency the axial spatial resolution is sufficient and amounts to 10 mm in the middle of the powered electrode in the optical axis of $a_{mwi} = 20\,mm$, which is discussed below.

At a microwave frequency of $f_{mwi} = 160.28\,GHz$ the quasi-optical theory has to be applied to describe the free space microwave propagation by a Gaussian beam, which describes the spatial distribution of the electric field of the microwave [116]. The normalized electrical field distribution at any distance along the axis of propagation is given by:

$$\left|\vec{E}(z,r)\right| = \sqrt{\frac{2}{\pi w^2}} \times \exp\left(-\frac{r^2}{w^2} - ikz - \frac{i\pi r^2}{\lambda_{mwi} R} + i\varphi_0\right) \tag{2.12}$$

The electrical field is normalized to its value at $z = 0$ and in addition normalized to set the integral $\int |E(z,r)|^2\, 2\pi r\, dr \equiv 1$ to unity with the boundary values of $r = 0 \to \infty$ [116]. The latter is important to satisfy the requirement that the total power (square of electrical field) is one integrated over the area of the beam. The distribution of the real part of the

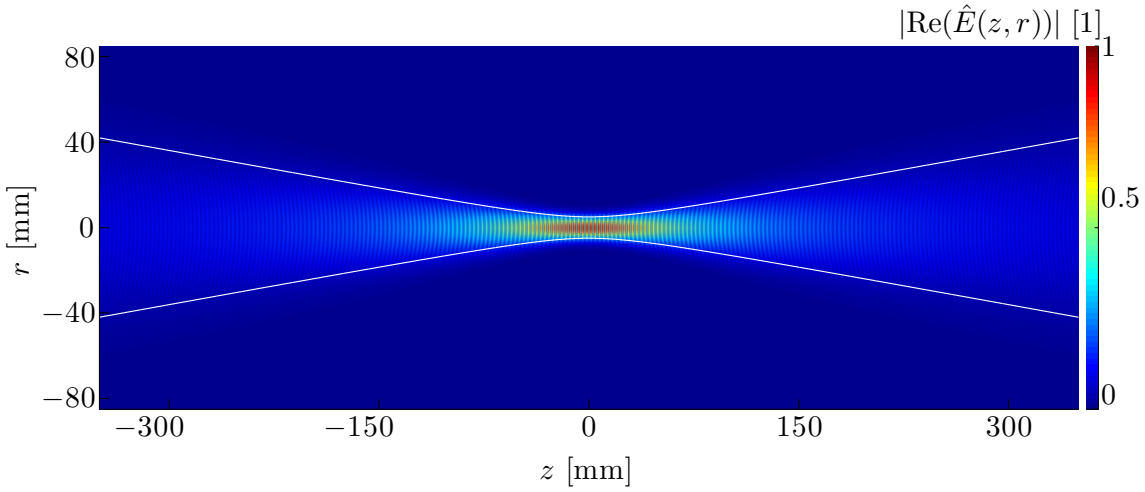

Fig. 2.2.: Total amount of the real part of the electrical field in dependence of the beam radius w, the radius of curvature R and the phase of the electrical field φ_0. The initial parameters are the beam waist $w_0 = 5\,\mathrm{mm}$ and the microwave frequency of $f_{\mathrm{mwi}} = 160.28\,\mathrm{GHz}$. The solid line represents the Gaussian beam radius w with the aforementioned beam waist.

electrical field is shown in Fig. 2.2 and is mainly defined by the three parameters w, R and φ_0.

$$w = w_0 \cdot \sqrt{1 + \left(\frac{z\,\lambda_{\mathrm{mwi}}}{\pi w_0^2}\right)^2} \tag{2.13}$$

$$R = z + \frac{1}{z}\left(\frac{\pi w_0^2}{\lambda_{\mathrm{mwi}}}\right)^2 \tag{2.14}$$

$$\varphi_0 = \arctan\left(\frac{z\,\lambda_{\mathrm{mwi}}}{\pi w_0^2}\right) \tag{2.15}$$

The beam radius w describes the 1/e decrease of the electric field amplitude at the position z in propagation direction along the optical axis. w_0 is the minimal beam radius in the focus at $z = 0$, which is the so-called beam waist and which defines the best axial spatial resolution perpendicular to the beam propagation. R is the curvature radius of the wave front and φ_0 is the phase of the electrical field. Consequently, an important property of the Gaussian beam theory is that the microwave beam diverges with increasing propagation direction z, see Fig. 2.2.

Under the requirements of the Gaussian beam theory, the free space propagation of the microwave beam can be calculated. Firstly, the optical axis was defined to 20 mm above the powered electrode. Under the requirements of the lossless propagation of the microwave beam through the vacuum chamber, the beam waist was set to $w_0 = 5\,\mathrm{mm}$ in the middle of the powered electrode. Based on these facts, special microwave guiding components are required. These are on the one hand the specifically calculated and manufactured cylindrical horn antennas, which are important for the sufficient transformation of the rectangular waveguide into free space and vice versa. These horn antennas have a beam waist of $w_{0,\mathrm{h}} = 4.5\,\mathrm{mm}$ and produce a well-defined Gaussian microwave beam. On the

other hand, two elliptical aluminum mirrors were calculated under the requirements of the Gaussian beam theory and subsequently manufactured. These mirrors are important for changing and refocusing the microwave beam direction, which is schematically shown in Fig. 2.1. With these two peripheral components, the alignment of the microwave beam propagation in free space was theoretically calculated, and was used to determine the position of the horn antennas and the elliptical mirrors.

To provide the frequency of 160.28 GHz a frequency stabilized, phase lock loop (PLL) heterodyne microwave interferometer was used, with an output power of about 1.3 mW. The temporal resolution of the microwave interferometer was up to 200 ns. The heterodyne system ensures an undisturbed and high quality measurement of the phase shift, by using a temporal modulation of the microwave phase at a difference frequency ω_0. The phase shift measurement is thus independent of the amplitude and the sign of the phase.

The microwave interferometer is separated into three functional units. Firstly, there is the *PLL unit* which supplies the difference frequency $\omega_0 = 30$ MHz on the bases of two Gunn oscillators, which are coupled to each other in a rigid manner. One Gunn oscillator provides the signal frequency for the reference path (80.17 GHz), and the other Gunn oscillator provides the signal frequency for the measurement path (80.14 GHz). The doubled difference of both signals provides an intermediate frequency of 60 MHz, which is needed as a reference in the analysis unit. The second part is the *measurement unit*, where the doubled signal frequency (160.28 GHz) of the measurement path is guided through the plasma and receives its additional phase shift in dependence of the electron density. Subsequently, the obtained signal is mixed with the doubled signal frequency of the reference path. Thus, a signal is generated at the intermediate frequency including the phase information. This signal is compared to the intermediate frequency coming from the reference path in the third part, the *analysis unit*. The *analysis unit* finally provides the sine of the phase shift in units of volts, which is evaluated by an oscilloscope.

To sum up, these theoretical considerations regarding the choice of frequency, the calculation of the free space propagation of the microwave, and the manufacturing of the optical components have ensured an optimized Gaussian beam microwave interferometry. Controlling the alignment of the free space microwave propagation was of great importance in the experimental setup. The accuracy of the alignment was verified by means of a specifically developed measurement method, for visualizing the Gaussian microwave beam. Two factors are of critical importance here and have to be proved. Firstly, the Gaussian microwave beam needs to be completely aligned in the optical axis. This is the case if the maximum of Gaussian microwave beam distribution is in the middle of the receiving horn antenna, which is axially aligned in the optical axis. Secondly, the beam radius $w(z)$ has to be measured for different positions z and compared to the previous theoretically calculated ones (2.13). Therefore, the microwave beam profile was measured by means of a cylindrical ceramic rod of 150 mm length and 1 mm diameter. A stepper motor moved this rod through the microwave beam perpendicular to the propagation direction z. This causes a disturbance of the microwave beam, which is measured by an oscilloscope. To determine the optical axis, an additional He-Ne laser beam was used along the optical axis of the receiving horn antennas. This way, the position of the maximum intensity of

the Gaussian beam distribution could be compared with the optical axis. The maximum intensity of the Gaussian beam distribution was shown to be at the same position as the aligned He-Ne laser, or the middle of the receiving horn antenna, respectively. Moreover, the Gaussian beam radius w could be determined by fitting the measured disturbance by means of a Gaussian distribution. Subsequently, the measured beam radius was compared to the theoretically calculated beam radius, which were in good accordance.

To benchmark the entire microwave interferometer diagnostic setup, line integrated electron density measurements were performed in a CCRF argon plasma. The resolution of the line integrated electron density was optimized to $5.3 \times 10^{13}\,\mathrm{m}^{-2}$, relating to a phase resolution of about 0.016°. Comparing the experimentally determined electron densities with the values from the literature revealed good accordance. Microwave interferometry was thus found to be a powerful diagnostic tool for non-invasive electron density measurements, it has a high sensitivity, a temporal resolution of 200 ns and an adequate spatial resolution of 10 mm.

2.3. Microwave interferometry and laser photodetachment – Article III

Laser photodetachment is based on the detachment of electrons from negative ions by means of a laser with an appropriate wavelength or frequency. This is shown for the detachment of negative atomic oxygen in (2.16).

$$\mathrm{O}^- + h\nu_1 \longrightarrow \mathrm{O} + \mathrm{e}^- \tag{2.16}$$

The detached electrons have to be measured by suitable diagnostics. In this work a combination of laser photodetachment and microwave interferometry was chosen, instead of the standard electric probe technique. This is because Langmuir probes have certain disadvantages compared to microwave interferometry. The probe measurement is based on measuring the ion current increase during the laser shot, which provides localized data. However, the usage of probes may drastically affect the plasma properties [20–22]. The interaction of the laser pulse with the probe material may also have some effects. Finally, various model assumptions are necessary to determine the negative ion densities from the probe characteristics [24, 25, 68]. Using a microwave interferometer instead of probes avoids these disadvantages. Simultaneously combining microwave interferometry and laser photodetachment to determine the line integrated negative oxygen ion density had never been done before in CCRF oxygen plasmas. The diagnostics is based on the measurement of the phase shift, which is produced by the additional electrons after the detachment laser pulse (2.16). This phase shift can be directly converted into a line integrated electron density. An example of a typical detachment signal, which is achieved by microwave interferometry, is shown in Fig. 2.3. The solid red line represents to an exponential fit function, which is justified by (3.3), to be discussed in section 3.3. The line integrated electron density immediately increases after the laser pulse at $t = 0$. Assuming that the laser pulse detaches all negative ions within the laser volume, the detachment

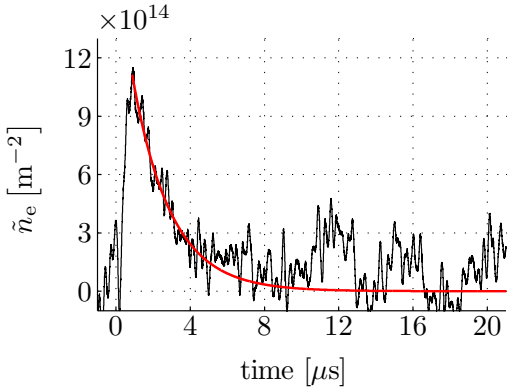

Fig. 2.3.: Detachment signal of the line integrated electron density and the exponential fit function (3.3) for 10 Pa, 12 W, −180 V self-bias voltage.

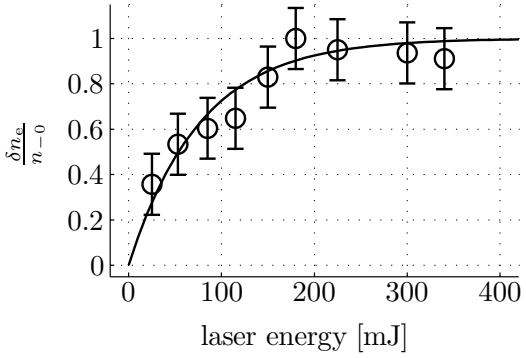

Fig. 2.4.: Ratio of the detached electrons δn_e and the steady state negative ion density n_{-0} over laser energy (2.18).

peak corresponds to the total amount of negative ion density. Furthermore, the decay of the detachment signal provides information about the relaxation of the additionally produced electrons to steady state, which provides a deeper insight into physical plasma processes, see section 3.3.

As mentioned above, for the detachment in oxygen a frequency doubled Nd:YAG laser at a wavelength of 532 nm has to be used, which is associated with a photon energy of about 2.3 eV. For the detachment of the atomic negative oxygen ions O^- (2.16) a photon energy of 1.46 eV is required [84]. Generally, in addition to atomic negative oxygen ions O^-, oxygen plasma can also contain the molecular ions O_2^- and O_3^-. The detachment of these molecular ions requires laser photodetachment energies of 0.44 eV and 2.1 eV, respectively [60].

In low-pressure RF plasmas, Katsch *et al.* has shown that the O_2^- density is less than 2 % [68], which is in good accordance with PIC-MCC simulations of CCRF plasmas [117] and optogalvanic study [118]. Further investiations have shown that the density of O_2^- and O_3^- is only of about 10 % of the total negative ion density [60, 84]. Moreover, comparable fluid model calculations also show the dominance of the negative atomic oxygen ions (Article VI). Negative atomic oxygen ions can therefore be assumed to be the main negative ion species in the investigated RF plasma.

For the laser photodetachment technique it is important to ensure that all negative ions are detached during the laser shot. The ratio of the detached electrons to the total number of negative ions depends on the laser power [55, 72, 83] and can be calculated.

$$\frac{\mathrm{d}\delta n_e}{\mathrm{d}t} = \frac{\sigma I_l}{h\nu_l}\left(n_{-0} - \delta n_e\right) \tag{2.17}$$

I is the laser intensity, $h\nu_l$ the photon energy of the laser and $\sigma = 6.4 \times 10^{-22}\,\mathrm{m}^2$ the photodetachment cross section [119, 120]. It should be noted that the photodetachment cross section can differ in the percent range [121] and that the chosen value is an intermediate value. Moreover, the steady state negative ion density is the sum of detached electrons

δn_e and the remaining negative oxygen ions n_-: $n_{-0} = \delta n_e + n_-$. Equation (2.17) can be estimated for a short-pulsed laser system by using $\int I_l \, dt \equiv E_l/A_l$, where E_l is the laser energy and $A_l = \pi R_l^2$ the laser beam cross section, which is discussed in detail in appendix A.1.

$$\frac{\delta n_e}{n_{-0}} = \left[1 - \exp\left(-\frac{\sigma}{h\nu_l}\frac{E_l}{A_l}\right)\right] \tag{2.18}$$

The theoretical curve (2.18) is shown in Fig. 2.4. The dots are experimental data for the detachment ratios for different laser energies. A laser energy of 350 mJ is sufficient to detach 99 % of the negative ions within the volume of the laser beam with a radius of $R_l = 6.5$ mm. Consequently, the laser was driven at a laser energy greater than 350 mJ.

3. Analysis of the steady state electron and negative ion densities

3.1. Line integrated electron densities in an argon and oxygen CCRF plasma – Article I, II, VI

A detailed analysis was performed of the line integrated electron density in an argon and oxygen plasma in dependence of the processing parameter RF power from 10 to 100 W, a self-bias voltage from −50 to −600 V, and a total gas pressure from 10 to 100 Pa. In the CCRF argon plasma, the electron density continuously increased with increasing RF power from 10^{15} to $3 \times 10^{16}\,\mathrm{m}^{-2}$, an example is shown in Fig. 3.1. The RF power increase is equivalent to an increasing energy transfer into the plasma. The corresponding heating of electrons results in more ionizing collisions [3], which leads to an enhanced ionization rate and a further increase in electron density. In comparing the line integrated electron density with the values found in the literature an estimated absolute electron density of between 10^{16} and $3 \times 10^{17}\,\mathrm{m}^{-3}$ was used, while using the confocal length as an effective path length as a first approximation. The line integrated electron density values obtained in this work were in good agreement with the values in Overzet *et al.* [115].

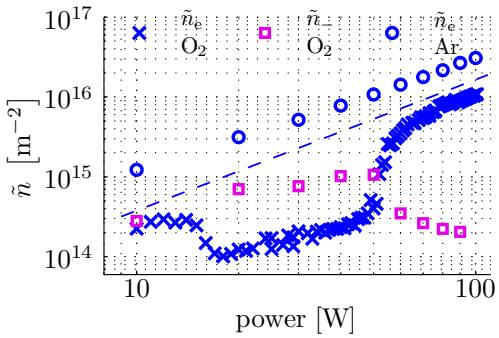

Fig. 3.1.: Comparison of the line integrated electron density (MWI) in argon (○) and oxygen (×) plasma as well as the line integrated negative ion density (□) in oxygen at 30 Pa total gas pressure and RF power variation.

The electron density measurements by microwave interferometry were furthermore compared with Langmuir probe diagnostics (Article VI). Therefore, preliminary investigations are done regarding the measurement of the radial plasma density distributions by means of suitable compensated and RF filtered Langmuir probe [122] in an argon CCRF plasma. The absolute electron density is determined by the Druyvesteyn method [123]. The discharge considered here operates in a transition regime with $\lambda_e > \lambda_+ \gtrsim \lambda_D$, for the mean

free path for the considered species. The line integrated electron density is numerically calculated from the radial electron density profiles, having a value of about $3.5 \times 10^{14}\,\mathrm{m}^{-2}$ for 10 Pa and 10 W. Compared to the directly measured line integrated electron density of about $9.5 \times 10^{14}\,\mathrm{m}^{-2}$ from MWI, the probe measurement yields a value of a factor 2.7 lower. This discrepancy is well-known in the literature [115, 124–129] and may be connected to the working regime of the probe. Another reason might be that for highly non-Maxwellian EEDFs the cylindrical probe geometry has to be taken into account because of the deviations in electron density calculations using the Druyvesteyn method [130].

Further investigations were performed regarding the sheath edge position in relation to the fixed position of the microwave beam axis at $a_{\mathrm{mwi}} = 20\,\mathrm{mm}$ above the powered electrode. This is of great interest, because the mean RF sheath edge varies with the pressure in the case of collision-dominated sheath. The mean RF sheath thickness d_{coll} can be estimated with a simple analytic calculation, assuming a collision-dominated RF sheath and an ion current density $j_{+\mathrm{rf}}$ proportional to the Bohm current $j_{+\mathrm{Bohm}} \propto \sqrt{\frac{k_{\mathrm{B}} T_{\mathrm{e}}}{m_+}}$.

$$d_{\mathrm{coll}} \propto \left(\frac{\epsilon_0 \cdot b_{+0}}{e \cdot n_{+0}} \cdot \left(\frac{m_+}{k_{\mathrm{B}} \cdot T_{\mathrm{e}}} \right)^{1/2} \right)^{1/3} \cdot (\bar{\phi}_{\mathrm{rf}})^{2/3} \cdot p^{-1/3} \tag{3.1}$$

In particular, the mean sheath thickness depends on the mean RF sheath voltage $\bar{\phi}_{\mathrm{rf}}$ and the total pressure p. At a constant mean sheath voltage, the distance between the microwave beam axis and the sheath edge ($20\,\mathrm{mm} - d_{\mathrm{coll}}$) increases with pressure and is scaled approximately with $p^{-1/3}$. A characteristic plasma density maximum is observed nearby the RF sheath edge [131]. Experimental investigations by means of optical emission spectroscopy provide the proportionality of the mean sheath thickness with the pressure variation by $p^{-1/n}$, with n in between 2 and 4 for argon and oxygen RF plasma [15, 17, 132]. A value of 3 is therefore a good approximation in correcting the distance between the sheath edge and the fixed microwave optical axis. Plotting the line integrated electron densities as a function of $P \cdot p^{-1/3}$ for total gas pressure higher than 30 Pa in argon, the values shift in one graph. Hence, the approximation for a collision-dominated RF sheath fits very well for higher total gas pressures.

The same dependence was seen for an oxygen CCRF discharge. The influence of the total gas pressure on the RF sheath thickness was similar to that observed in the argon plasma. When plotting the line integrated electron density over $P \cdot p^{-1/3}$ the values match approximately in one graph for different total gas pressure values.

However, in comparison to the argon plasma, the oxygen plasma provides lower electron densities, which is shown in Fig. 3.1 for 30 Pa. The lower density is due to the electronegative character of the oxygen plasma, which includes for instance the formation of negative ions by attachment processes, resulting in a reduction of electrons. The line integrated electron density is significantly reduced by half an order of magnitude and amounts to 10^{14} and $10^{16}\,\mathrm{m}^{-2}$ in the investigated RF power range. Moreover, the oxygen plasma is distinguished from the argon plasma by the fact that the line integrated electron density does not increase continuously with rising RF power. A dip occurs in the line integrated electron density within 20 and 50 W, which can be seen in for instance Fig. 3.1 for 30 Pa.

The onset RF power of this characteristic electron density dip shifts with increasing total gas pressure. In this region the line integrated electron density only slightly increases and is significantly lowered with values between 8×10^{13} and $5 \times 10^{14}\,\mathrm{m}^{-2}$. But for further RF power increase, greater than 50 W, the line integrated electron density rises over one order of magnitude up to $10^{16}\,\mathrm{m}^{-2}$. This may be combined with a mode transition of the discharge, which is discussed in more detail in the following section 3.2.

3.2. Mode transition in oxygen – Article III, VI

For fixed RF power of 40 W the line integrated negative ion density was estimated for 10, 20, 30 and 60 Pa by means of laser photodetachment and microwave interferometry. The line integrated negative ion density values amount to $2 \times 10^{14}\,\mathrm{m}^{-2}$ for 10 Pa, $5 \times 10^{14}\,\mathrm{m}^{-2}$ for 20 Pa, $7 \times 10^{14}\,\mathrm{m}^{-2}$ for 30 Pa, and $10^{15}\,\mathrm{m}^{-2}$ for 60 Pa. The decay time constant can be evaluated by the use of a single exponential fit function of the detachment relaxation signal, which is exemplified in Fig. 2.3 for a detachment signal and is satisfied by (3.3). The corresponding values are 75 µs for 10 Pa, 37 µs for 20 Pa, 3.2 µs for 30 Pa, and 1.6 µs for 60 Pa. The relaxation time constant changes significantly from high to low over one order of magnitude, due to the total gas pressure change from 20 to 30 Pa. This reveals a transition between two different discharge modes. Within one discharge mode the relaxation time constant decreases with increasing total gas pressure as expected, because of the direct proportionality of the collision frequency to the total gas pressure. Also for RF power variation at fixed total gas pressure a mode transition can be seen, as mentioned in the previous section. There the oxygen RF discharge can be divided into two different discharge modes. Beside the line integrated electron $\tilde{n}_\mathrm{e}$, the negative ion density $\tilde{n}_-$ and the resulting electronegativity $\tilde{n}_-/\tilde{n}_\mathrm{e}$, the decay time constant of the detachment signal also shows non-monoton behavior, see Fig. 3.2. They all show step-like behavior between 50 and 60 W. The line integrated electron density displays a rather small increase in the first mode, in the range of a few $10^{14}\,\mathrm{m}^{-2}$ in the low RF power range below 50 W. With increasing RF power a significant jump in the densities occurs, reaching values up to $10^{16}\,\mathrm{m}^{-2}$ at 100 W, which corresponds to the second mode.

The behavior of the line integrated negative ion density is the other way around. For low RF power the density is high with values of about $10^{15}\,\mathrm{m}^{-2}$. It decreases with increasing RF power to values of about $10^{14}\,\mathrm{m}^{-2}$. This dramatic change in the oxygen RF plasma is also reflected in the ratio between the negative ion and electron densities ($\tilde{n}_-/\tilde{n}_\mathrm{e}$). The value for $\tilde{n}_-/\tilde{n}_\mathrm{e}$ switches from high ($\tilde{n}_-/\tilde{n}_\mathrm{e} > 2$) to low ($\tilde{n}_-/\tilde{n}_\mathrm{e} < 1$) electronegativity [Fig. 3.2(c)]. This defines two modes, which are sharply separated by RF power values between 50 and 60 W. This mode transition can also be seen in the decay time constant of the detachment signal, see Fig. 3.2(d). For the high electronegative mode, the relaxation of the detached electrons needs a few microseconds only. For the low electronegative mode, the relaxation time is much longer and can be up to about 100 µs.

Comparing these results with the phase resolved optical emission spectroscopy (PROES) of excited atomic oxygen at 844 nm [15, 17], the significant change between the high and low electronegative mode correlates with the transition of CCRF discharge from the α-

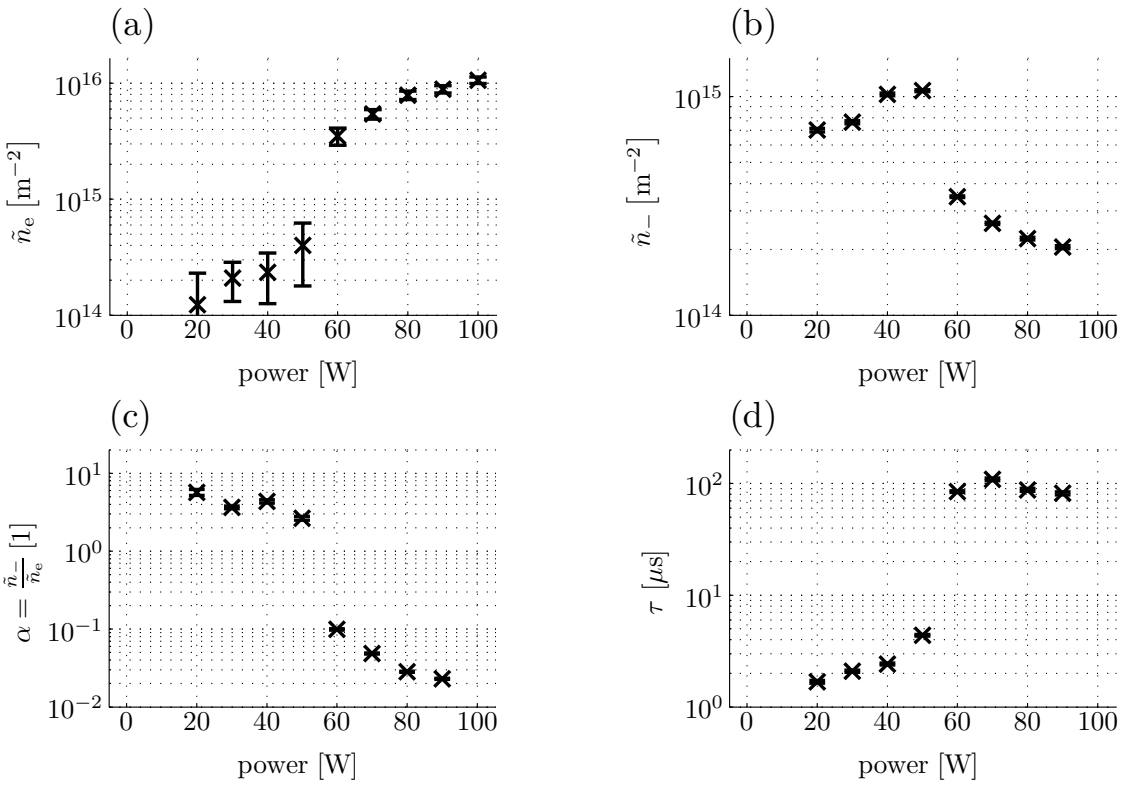

Fig. 3.2.: Mode transition in dependence of RF power for total gas pressure of 30 Pa in oxygen. Comparison of the line integrated steady state electron density (a), the line integrated steady state negative ion density (b), the electronegativity $\alpha = \tilde{n}_-/\tilde{n}_e$ (c), and the decay time constant of the detachment signal (d), evaluated by an exponential fit function, see Fig. 2.3.

mode to the γ-mode [133]. The α-mode is characterized by the excitation pattern I which is due to electron heating during the sheath expansion phase, see Fig. 3.3. The excitation pattern III is due to the electric field reversal during the RF sheath collapse. This electron heating is common for electronegative plasmas to ensure the current balance within one RF cycle, if the negative ion density is high. Moreover, fluid model calculations (FMC) were performed in comparison to the experiment in cooperation with Loffhagen *et al.* [134], see Article VI. Preliminary results of FMC also showed this pattern I and III at conditions comparable to the experimental conditions and likewise reveal the high electronegative mode. Moreover, the α-mode is characterized by a higher electron temperature T_e and lower electron density [133,135,136]. This higher electron temperature furthermore reveals higher values for the attachment coefficients (k_{aX}, $k_{a\Delta}$) and thus a higher efficiency of the dissociative attachment of negative atomic oxygen with the molecular ground state and molecular excited metastable state [137, 138]. This explains the effective production and the hight number of the negative ions in this discharge mode.

When the plasma transfers to the γ-mode [133, 139], the electron density significantly increases due to the simultaneous decrease of the negative ion density, as mentioned above. One reason for this strong increase is the production of secondary electrons by the detachment of negative ions within the RF sheath ("pseudo-secondary electron"), and by the

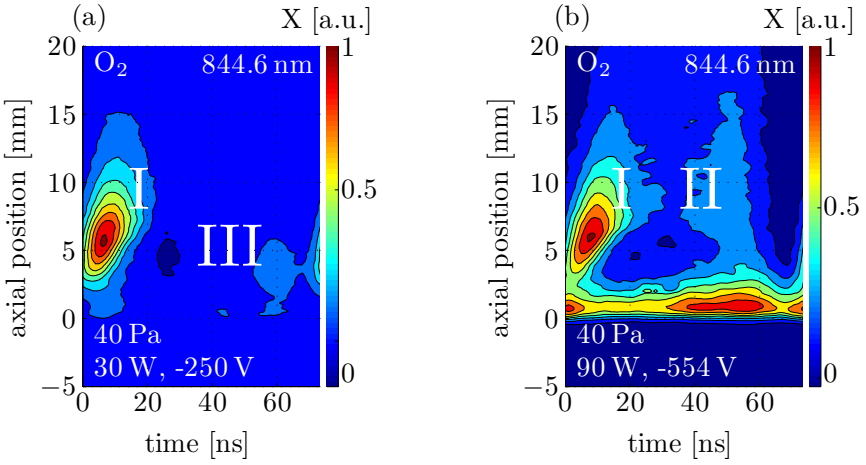

Fig. 3.3.: Spatial and RF phase resolved emission spectroscopy (PROES) for the corresponding atomic oxygen line by 844 nm [15,17,18,46] at a total gas pressure of 40 Pa. The ordinate represents the axial distance a to the powered electrode. (a) Excitation due to electron heating during the sheath expansion phase (I), the α-mode and (III) the electric field reversal during the RF sheath collapse of the RF discharge (30 W). (b) The excitation pattern (II) due to secondary electrons in the γ-mode of the RF discharge (90 W). The excitation of atomic oxygen due to heavy particle impact can be seen immediately in front of the powered electrode ($a = 0$ mm).

energetic heavy particle bombardment at the RF electrode (γ-process). The production of secondary electrons can be also seen by the additional appearance of a second excitation pattern (II), which is due to secondary electrons and was measured by means of PROES, see Fig. 3.3(b). This pattern were also observed in the Particle In Cell-Monte Carlo Collision (PIC-MCC) simulation [18,140,141], which revealed comparable results to those found in this work, see Article VI. The γ-mode is distinguished from the α-mode by a lower electron temperature at a much higher electron density [133, 135, 136], which is comparable to the conditions in the negative glow of a DC discharge. Moreover, this reduced electron temperature lowers the dissociative electron attachment rate coefficients and may explain the lower negative ion density and the lower electronegativity.

In different mixtures of argon and oxygen the mode transition is also observed [Fig. 3.4]. For all argon-oxygen admixtures at RF power higher than 50 W, the transition from high to low electronegative mode takes place. At this threshold, the transition into the γ-mode by a strong electron density increase and negative ion density decrease can directly be seen. At a relatively low oxygen admixture of 10 % in argon the electron density is already reduced, which can be seen in comparison to 100 % argon in Fig. 3.1. Hence, already for this small amount of oxygen, the discharge changes its character from electropositive to electronegative with an electronegativity of about $\tilde{n}_-/\tilde{n}_e = 1$. With increasing oxygen admixture the two modes of electronegativity, observed in pure oxygen plasmas, are more and more pronounced, see Fig. 3.4. In the case of 90 % oxygen admixture, the negative ion density in the high electronegative mode (RF power smaller than 50 W) exceeds the electron density by a factor of about 4 and shows similarities with a 100 % oxygen plasma.

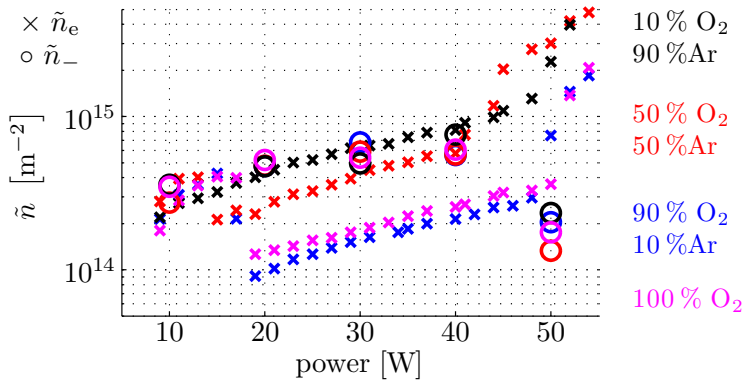

Fig. 3.4.: Line integrated electron (×) and negative oxygen ion (○) densities for different admixtures of argon and oxygen at 40 Pa total gas pressure and RF power variation.

3.3. High electronegative mode – Article III

For the high electronegative mode, which is due to a high amount of negative ions as well as a short relaxation time constant of the detachment signal [Fig. 3.2(d)] a simple 0d attachment-detachment model is applied. This model describes the detachment signal analytically and can estimate the effective rate coefficients for dissociative electron attachment $\tilde{K}_a$ and negative ion detachment $\tilde{K}_d$. It involves, two electron attachment reactions (with ground state and metastable with excited molecular oxygen), and three negative ion detachment reactions (with the corresponding molecular oxygens and the atomic oxygen) (3.2). The densities of the heavy species $O_2\left(X^3\Sigma_g^-\right)$, $O_2\left(a^1\Delta_g\right)$ and $O\left(^3P\right)$ are assumed to not change significantly during the short relaxation time in the microsecond range. The positive ion density is also taken to be unaffected by the electron impact ionization and the recombination reaction of positive ions. The characteristic reaction time constant for the recombination of the molecular positive ions with electrons and with negative atomic oxygen ions, using the rate coefficient k_{re} and $k_{r\text{-}}$ [137] and the corresponding positive ion density, is estimated to $1/(k_{re} \cdot n_{+0}) \sim 5\,\text{ms}$ and $1/(k_{r\text{-}} \cdot n_{+0}) \sim 10\,\text{ms}$. By contrast, the loss of negative atomic oxygen ions is much faster by detachment reactions with ground state and metastable excited molecular oxygen. These reactions are characterized by reaction time constants in the order of $1/(k_{dX} \cdot n_X) \sim 0.1\,\text{ms}$ and $1/(k_{d\Delta} \cdot n_\Delta) \sim 0.01\,\text{ms}$. Consequently, two attachment reactions and three detachment reactions are assumed for the simple 0d attachment-detachment model, resulting in the following rate equation.

$$\begin{aligned} \frac{dn_e}{dt} &= -\left(k_{aX}\left(T_e\right) n_X + k_{a\Delta}\left(T_e\right) n_\Delta\right) n_e + \left(k_{dX} n_X + k_{d\Delta} n_\Delta + k_{dO} n_O\right) n_- \\ &= -\tilde{K}_a n_e + \tilde{K}_d n_- \end{aligned} \tag{3.2}$$

To simplify the following discussion, effective rate coefficients are introduced for the attachment and the detachment processes $\tilde{K}_a$ and $\tilde{K}_d$, respectively. Using the steady state solution with $n_e + n_- = n_{+0} = \text{const}$ and the initial conditions $n_e(t=0) = n_{e0} + n_{-0} = n_{+0}$, the decay of the detachment signal is described by a single exponential decay function.

$$\Delta n_e(t) = \left(n_e(t) - n_{e0}\right) = n_{-0} \cdot \exp\left[-\left(\tilde{K}_a + \tilde{K}_d\right) \cdot t\right] \tag{3.3}$$

The effective attachment ($\tilde{K}_\mathrm{a}$) and detachment ($\tilde{K}_\mathrm{d}$) coefficients were evaluated from the measured decay time constant of the detachment signal τ and the line integrated electron and negative ion densities expressed by the electronegativity $\alpha = n_-/n_\mathrm{e}$.

$$\tilde{K}_\mathrm{a} = \frac{1}{\tau} \cdot \frac{1}{1+\frac{1}{\alpha}} \qquad (3.4) \qquad\qquad \tilde{K}_\mathrm{d} = \frac{1}{\tau} \cdot \frac{1}{1+\alpha} \qquad (3.5)$$

One main result of this model is that the main loss channel of the negative ions in oxygen CCRF plasma is the detachment by molecular metastable oxygen $\mathrm{O_2}\left(\mathrm{a}^1\Delta_\mathrm{g}\right)$. The detachment of the negative ions by atomic oxygen can be neglected because of its low density in the range of only $10^{19}\,\mathrm{m}^{-3}$, which was measured by two photon laser-induced fluorescence spectroscopy [142–144], and which was also in agreement with the fluid model calculation (FMC), see Article VI. For the given experimental conditions, the negative ion detachment by ground state molecular oxygen can also be neglected due to the low rate coefficient [137]. Hence, the effective detachment coefficient $\tilde{K}_\mathrm{d}$ can be used to estimate the metastable density n_Δ for different RF power values by using $\tilde{K}_\mathrm{d} = k_{\mathrm{d}\Delta} n_\Delta$.

The ground state molecular oxygen density n_X can be estimated from the difference between the metastable density, and the total particle density at 30 Pa total gas pressure and a temperature of 300 K by means of ideal gas law. The relative density of the molecular metastable $\mathrm{O_2}\left(\mathrm{a}^1\Delta_\mathrm{g}\right)$ is estimated to be in the order of 10 % of the molecular ground state density, which is in good accordance with the values in the literature [145–147]. With the effective attachment rate coefficient $\tilde{K}_\mathrm{a}$ the attachment rate coefficients for the molecular ground state $k_{\mathrm{a}\mathrm{X}}$ and the molecular metastable state $k_{\mathrm{a}\Delta}$ were calculated, using the estimated molecular ground state n_X and molecular metastable density n_Δ. The estimated attachment rate coefficients slightly decrease with increasing RF power from $4.4 \times 10^{-17}\,\mathrm{m}^3/\mathrm{s}$ to $1.6 \times 10^{-17}\,\mathrm{m}^3/\mathrm{s}$ for the attachment with molecular ground state oxygen $\mathrm{O_2}\left(\mathrm{X}^3\Sigma_\mathrm{g}^-\right)$, and from $1.6 \times 10^{-16}\,\mathrm{m}^3/\mathrm{s}$ to $9.5 \times 10^{-17}\,\mathrm{m}^3/\mathrm{s}$ for the attachment with metastable molecular oxygen $\mathrm{O_2}\left(\mathrm{a}^1\Delta_\mathrm{g}\right)$. The decrease of both attachment rate coefficients is due to the decrease in electron temperature from 6 to 2 eV, which is in good agreement with values in the literature [137, 138] for the α-mode. Moreover, the reduction in electron temperature indicates the transition to the γ-mode.

Summarizing, the simple 0d attachment-detachment model shows that the metastable molecular singlet state $\mathrm{O_2}\left(\mathrm{a}^1\Delta_\mathrm{g}\right)$ is the most important species in interpreting both the effective attachment and detachment rate coefficients.

4. Temporal behavior of electron and negative ion densities

4.1. Detachment-induced electron production in the early afterglow – Article IV

This sections discusses the results from investigations on the temporal behavior of the electron and negative ion densities. In the experiment, the RF power was pulsed with 10 Hz and a duty cycle of 50 %. The CCRF oxygen discharge was studied in the low and high electronegative mode. The temporal behavior of the line integrated electron density

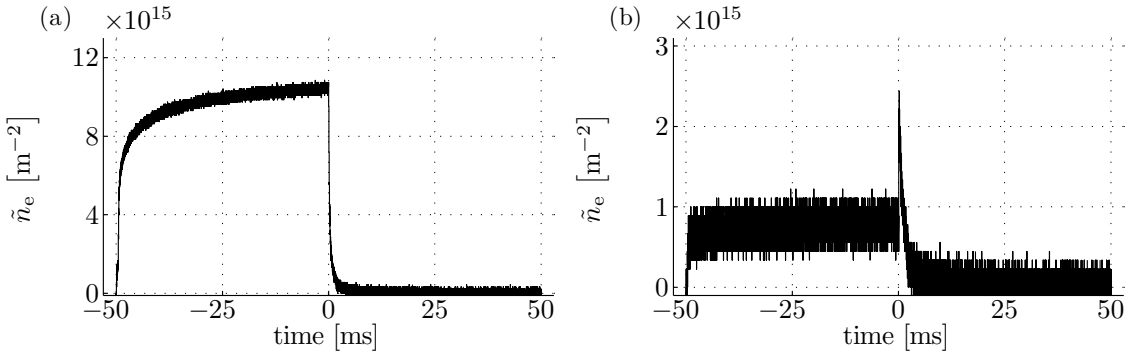

Fig. 4.1.: Temporally resolved line integrated electron density in a 10 Hz (50 % duty cycle) pulsed oxygen RF plasma (40 Pa, 5 sccm) at RF power of (a) 91 W (low electronegative mode) and (b) 48 W (high electronegative mode). The RF power is enabled at −50 ms and disabled at 0 ms.

is shown in Fig. 4.1(a) for the low electronegative mode (high RF power, 91 W) and in 4.1(b) for the high electronegative mode (low RF power, 48 W). For both modes the electron density rises after enabling the RF power at $t = -50$ ms and achieves a steady state value of 10^{16} m^{-2} for the low and 0.8×10^{14} m^{-2} for the high electronegative mode. As explained in section 3.2 the electron density of both modes is distinguished by one order of magnitude. Additionally, a different early afterglow behavior of the electron density was found. For the low electronegative mode, the electron density increases after enabling the RF power and reaches its steady state value after a few milliseconds. After disabling the RF power at $t = 0$, the electron density decreases immediately. Here the electron density afterglow behavior is the same as for an electropositive gas such as argon.

However, some differences were observed when comparing the oxygen plasma with the electropositive argon plasma at the same discharge parameters. Firstly, the time constant of the electron density reduction in the afterglow in oxygen is about 1.5 ms, which is much

shorter than in argon. Secondly, the electron kinetics in oxygen appears to be a second order kinetics. Consequently, the dissociative recombination of electrons with molecular oxygen ions seems to be the dominant loss process. The kinetics of the argon plasma on the other hand appears to be a first order reaction kinetics. This indicates that the main loss processes are diffusion and surface recombination.

In contrast to the afterglow behavior of the argon plasma and the oxygen plasma in the low electronegative mode, an electron density peak occurs in the early afterglow of the high electronegative mode in oxygen, see Fig. 4.1(b). The line integrated electron peak density $\tilde{n}_{\mathrm{eP}}$ exceeds the mean steady state line integrated electron density $\tilde{n}_{\mathrm{e}}$. The difference of peak and mean line integrated electron densities, divided by the mean line integrated electron density $((\tilde{n}_{\mathrm{eP}} - \tilde{n}_{\mathrm{e}})/\tilde{n}_{\mathrm{e}})$, is a measure for the electronegativity. This fraction decreases from about 5.5 to 2.5 with increasing RF power for a total gas pressure of 40 Pa. This is similar to the electronegativity $(\tilde{n}_{-}/\tilde{n}_{\mathrm{e}})$ determined from the measured negative ion and electron densities, which shows a high number of negative ions [Fig. 3.4]. Assuming a simple exponential function, the temporal increase of the electron density to the peak value can be approximated. This is satisfied, if one assumes that the electron production is connected to the detachment of negative atomic oxygen O^-, e. g., by collisions with atomic oxygen O $\left(^3\mathrm{P}\right)$, molecular ground state O_2 $\left(\mathrm{X}^3\Sigma_{\mathrm{g}}^-\right)$, or metastable molecular oxygen O_2 $\left(\mathrm{a}^1\Delta_{\mathrm{g}}\right)$. Taking these processes into account for the electron production in the early afterglow, it is also aligned with the consumption of negative ions, as shown in the following equation.

$$\frac{\mathrm{d}n_{\mathrm{e}}}{\mathrm{d}t} = -\frac{\mathrm{d}n_{-}}{\mathrm{d}t} = \left(k_{\mathrm{dO}} n_{\mathrm{O}} + k_{\mathrm{d}\Delta} n_{\Delta} + k_{\mathrm{dX}} n_{\mathrm{X}}\right) n_{-} = \frac{1}{\tau} n_{-} \tag{4.1}$$

Assuming constant densities of the involved neutral species within the early afterglow phase, the rate equation (4.1) can be solved for the negative ion (4.2) and electron (4.3) densities taking into account the corresponding initial conditions for negative ions $n_{-}(0) = n_{\mathrm{eP}} - n_{\mathrm{e}}(0)$ and electrons $n_{\mathrm{e}}(0)$, respectively.

$$\begin{aligned} n_{-}(t) &= n_{-}(0) \times \exp\left(-t/\tau\right) \\ &\propto \left[n_{\mathrm{eP}} - n_{\mathrm{e}}(0)\right] \times \left(\exp\left(-t/\tau\right)\right) \qquad (4.2) \\ n_{\mathrm{e}}(t) &= n_{\mathrm{e}}(0) + \left[n_{\mathrm{eP}} - n_{\mathrm{e}}(0)\right] \times \left(1 - \exp\left(-t/\tau\right)\right) \qquad (4.3) \end{aligned}$$

The equations confirm that the electron density increases, whereas the negative ion density decreases, in the early afterglow. To verify this hypothesis the temporal behavior of the negative ion density in the early afterglow was additionally measured. The electron and the negative ion density are plotted in Fig. 4.2 for the early afterglow phase, for 40 Pa in the high electronegative mode. In order to be able to compare the two densities, the rising electron density is rewritten as $(\tilde{n}_{\mathrm{eP}} - \tilde{n}_{\mathrm{e}}(t))/[\tilde{n}_{\mathrm{eP}} - \tilde{n}_{\mathrm{e}}(0)] = \exp\left(-t/\tau\right)$, and the negative ion density as $\tilde{n}_{-}(t)/\tilde{n}_{-}(0) = \exp\left(-t/\tau\right)$. As expected, both exponential functions have about the same time constant of 53 µs. This supports the hypothesis that the electrons are produced by negative ion detachment in the early afterglow.

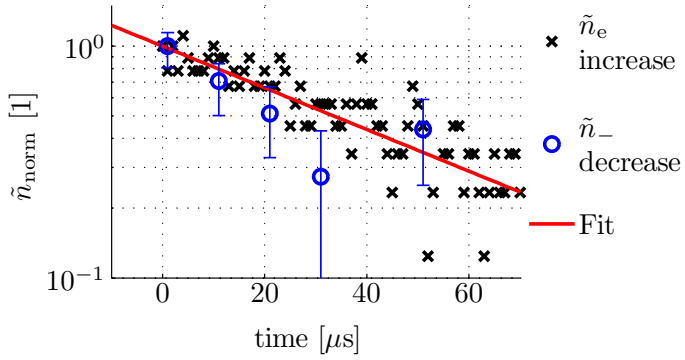

Fig. 4.2.: Fit of the re-arranged analytical functions for electrons (4.3) $(\tilde{n}_{\mathrm{eP}} - \tilde{n}_{\mathrm{e}}(t))/[\tilde{n}_{\mathrm{eP}} - \tilde{n}_{\mathrm{e}}(0)] = \exp(-t/\tau)$ (×) and negative ions (4.2) $\tilde{n}_-(t)/\tilde{n}_-(0) = \exp(-t/\tau)$ (○) to the experimental data.

To validate the experimentally achieved afterglow time constant the corresponding time constant for detachment of negative atomic ions O^- by molecular ground state can be estimated to $1/(k_{\mathrm{dX}} \cdot n_{\mathrm{X}}) \propto 100\,\mu\mathrm{s}$. For this estimation a detachment rate coefficient of $k_{\mathrm{dX}} = 10^{-18}\,\mathrm{m^3\,s^{-1}}$ [137] is taken, which is adequate for the discharge conditions in this work. The molecular ground state density is calculated by ideal gas law at 40 Pa and 300 K and amounts to $n_{\mathrm{X}} = 10^{22}\,\mathrm{m^{-3}}$. The detachment time constant with metastables can be estimated in the same way. Its density is approximately 10 % of the ground state density [145–147], see section 3.3. This reaction channel is important and has to be considered for various reasons. Firstly, the rate coefficient is about $k_{\mathrm{d}\Delta} = 10^{-16}\,\mathrm{m^3\,s^{-1}}$ [137,145,148–150], which is significantly higher compared to the ground state. Secondly, the lifetime of the metastable molecular oxygen is up to 10^3 s [137,151], and for the used discharge conditions in the millisecond range. Consequently, the time constant amounts to $1/(k_{\mathrm{d}\Delta} \cdot n_{\Delta}) \propto 10\,\mu\mathrm{s}$. The estimated time constants are in the order of the measured values of between 60 and 20 µs, for increasing RF power values from 20 to 50 W. These estimations emphasize the important role of the metastable molecular oxygen in the CCRF oxygen discharge and particularly for the detachment of negative ions in the early afterglow.

4.2. Modeling the afterglow behavior – Article IV

Advanced knowledge of the early afterglow behavior in the CCRF oxygen discharge was obtained using a 0d rate equation model. In short, a set of nine elementary reactions was applied, involving recombination, detachment, and charge transfer reactions (4.4a-4.4i). The included neutral particles are molecular ground state oxygen ($O_2\,(X^3\Sigma_g^-)$), molecular metastable oxygen ($O_2\,(a^1\Delta_g)$) and atomic oxygen (O). The involved charged particles are

electrons (e^-), negative oxygen ions (O^-, O_2^-) and positive molecular oxygen ions (O_2^+).

$$O_2^+ + e^- \xrightarrow{k_{re}} O\left(^3P\right) + O\left(^3P\right) \tag{4.4a}$$

$$O_2^+ + O^- \xrightarrow{k_{r-}} O_2\left(X^3\Sigma_g^-\right) + O\left(^3P\right) \tag{4.4b}$$

$$O_2^+ + O_2^- \xrightarrow{k_{r-,2}} O_2\left(X^3\Sigma_g^-\right) + O_2\left(X^3\Sigma_g^-\right) \tag{4.4c}$$

$$O^- + O\left(^3P\right) \xrightarrow{k_{dO}} O_2\left(X^3\Sigma_g^-\right) + e^- \tag{4.4d}$$

$$O_2^- + O\left(^3P\right) \xrightarrow{k_{dO,2}} O_2\left(X^3\Sigma_g^-\right) + O\left(^3P\right) + e^- \tag{4.4e}$$

$$O^- + O_2\left(X^3\Sigma_g^-\right) \xrightarrow{k_{dX}} O_3 + e^- \tag{4.4f}$$

$$O^- + O_2\left(a^1\Delta_g\right) \xrightarrow{k_{d\Delta}} O_3 + e^- \tag{4.4g}$$

$$O_2^- + O_2\left(a^1\Delta_g\right) \xrightarrow{k_{d\Delta,2}} O_2\left(X^3\Sigma_g^-\right) + O_2\left(X^3\Sigma_g^-\right) + e^- \tag{4.4h}$$

$$O^- + O_2\left(a^1\Delta_g\right) \xrightarrow{k_{c\Delta}} O_2^- + O\left(^3P\right) \tag{4.4i}$$

It is not necessary to consider the attachment reactions of free electrons with molecular ground state or metastable state, because of their rather low reaction rate coefficients (k_{aX}, $k_{a\Delta}$) at rather low electron temperature T_e [137, 138]. As is known from the literature, [99, 112] the electron temperature decreases in the nanosecond timescale after disabling the RF power. Consequently, the attachment reaction coefficients rapidly decrease.

The set of elementary processes results in six rate equations for the considered species. It has to be mentioned that for the positive ions and electrons a loss term is included, which takes into account the effective diffusion time step $\tau_d = L_d^2/D_a$. Where D_a is the ambipolar diffusion coefficient and L_d the diffusion length. The latter, is set to 20 mm which is the distance from the microwave beam axis to the powered electrode. The entire rate equation system is numerically solved, with a fixed time constant $\Delta t = 1\,\mu s$. The numerical fit routine is treated as a least square fit to achieve the best agreement between the modeled and the measured electron densities. This requires some initial parameters at $t = 0$. The initial values for O_2^-, O_2^+, O, $O_2\left(a^1\Delta_g\right)$ and D_a can only vary within the appropriate physical range. For the initial electron ($\tilde{n}_e$) and negative ion ($\tilde{n}_-$) densities, the steady state values are taken from the measurements at $t = 0$. These are converted into absolute values by assuming an average density above the diameter of the powered electrode (0.1 m) as an effective line of sight of the microwave interferometry. The transition from the line integrated density to absolute values was achieved by $n/\,m^{-3} = \tilde{n}/\,m^{-2}/0.1\,m$.

The 0d model describes the electron density afterglow behavior very well for both electronegative modes. The temporal behavior of the measured [Fig. 4.3, gray] and of the model calculated electron density [Fig. 4.3, line marked with ×] are in good agreement. Furthermore, the model predicts that the negative ion density immediately decreases after disabling the RF power at $t = 0$, which is likewise in good accordance with the laser photodetachment measurements, see Fig. 4.2. And finally, for both modes the model predicts that the initial density of O_2^- is significantly lower compared to the negative atomic oxygen

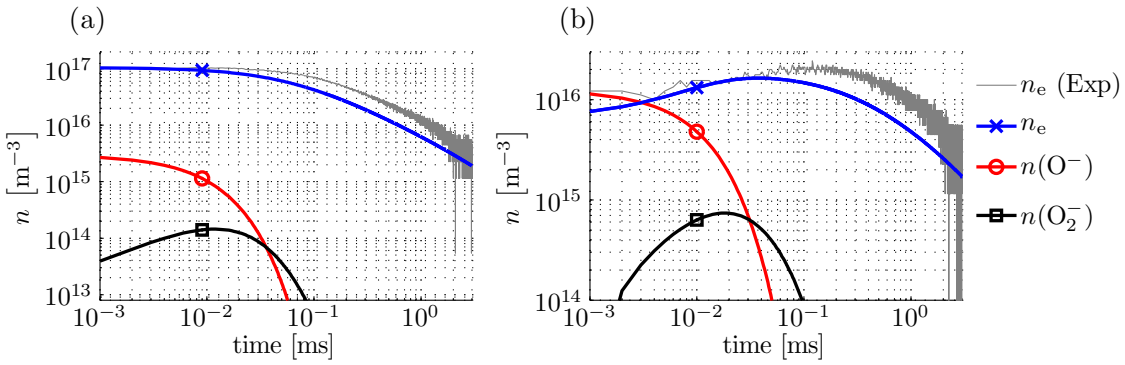

Fig. 4.3.: Comparison of the experimental (gray) and model based (×) electron density afterglow behaviors for (a) 91 W low electronegative mode and (b) 48 W high electronegative mode, both at gas pressure of 40 Pa. The calculated negative ion densities of O^- (○) and of O_2^- (□) are also shown.

O^- density, which is in good accordance with the values in the literature [60, 68].

For the low electronegative mode [Fig. 4.3(a)], the modeled electron density directly decreases after $t = 0$, as it does in the experiment. Parameter studies of the model have shown that the decreasing electron density is dominated by the recombination and diffusion processes. For the high electronegative mode [Fig. 4.3(b)] the calculated and the measured electron densities are also parallel: booth increase in the early afterglow. In this mode parameter studies of the model have shown that the detachment of the negative atomic oxygen atoms is the dominant production channel of electrons in the early afterglow. The detachment with molecular metastable $O_2\left(a^1\Delta_g\right)$ plays an essential role.

In summary, it can be concluded that the presence of negative ions has a strong influence on the temporal afterglow behavior of the discharge. A further interesting temporal behavior is the appearance of instabilities in the electronegative oxygen CCRF discharge, which will be discussed in the following section.

4.3. Instabilities in the oxygen discharge – Article V, VI

Investigations in the electronegative CCRF oxygen plasma have shown that it is dominated by instabilities. These can strongly influence several plasma parameters, such as floating potential, ion saturation current, electron density and optical emission intensity.

Fluctuations are discussed in several publications in the framework of attachment-induced ionizations instabilities [38, 39, 42]. The appearance of this kind of instability is analyzed by Nighan and Wiegand [40]. The instabilities are not only seen in oxygen [39, 41, 43] but also in other electronegative plasmas [41, 42, 152] as well as in dusty plasmas [153–156]. What all these investigations have in common is the existence of negative ions or negatively charged dust particles, which act as electron sinks.

Two examples of the fluctuation of the line integrated electron density are shown in dependence of RF power in Fig. 4.4 for 50 Pa and 70 Pa. The steady state background line integrated electron density is subtracted. One remarkable fact is that for 50 Pa there

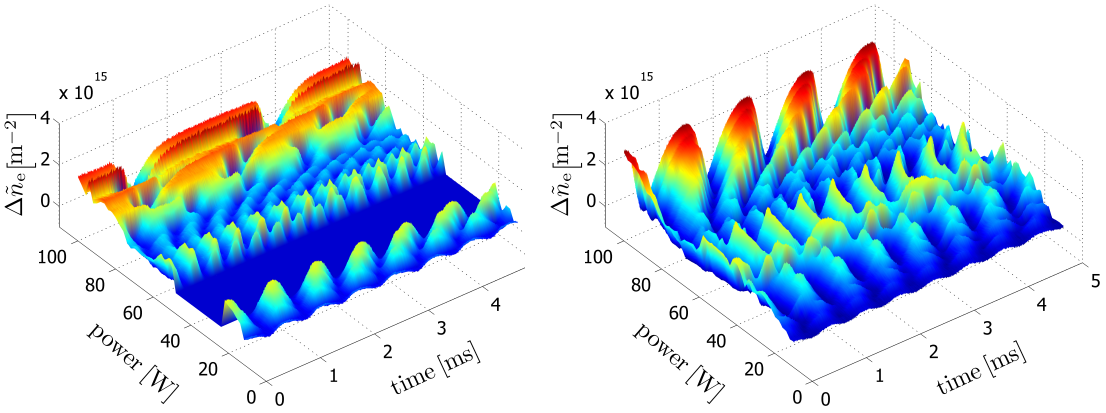

Fig. 4.4.: Line integrated electron density fluctuations in dependence of RF power and time, for a process pressure of 50 Pa (left) and 70 Pa (right). The mean line integrated electron density is subtracted.

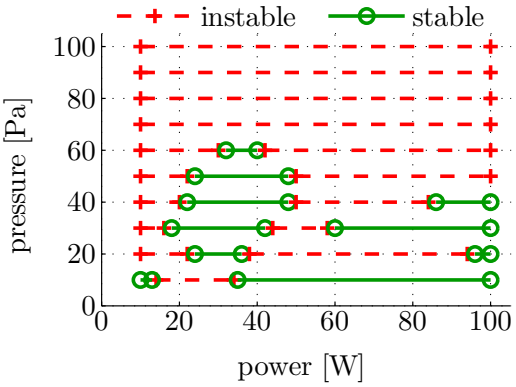

Fig. 4.5.: Pressure and RF power dependence on the stable and instable regions of the oxygen RF plasma in the investigated ranges of 10 to 100 Pa and 10 to 100 W.

is a region of no fluctuations between 20 and 50 W RF power, whereas at pressures higher than 70 Pa the plasma is dominated by instabilities. Hence, it is possible to draw areas where instabilities in dependence of pressure and RF power exist, see Fig. 4.5. Stable regions can only be found below 70 Pa total gas pressure.

For the entire investigated parameter set the frequency of the instabilities are ranging between 0.3 and 3 kHz and have peak-to-peak line integrated electron densities from 0.5×10^{15} to $3.5 \times 10^{15}\,\mathrm{m}^{-2}$. A system of two electric probes was installed for further detailed analysis. One probe is the so-called trigger probe and the other probe is the measuring probe. The trigger probe is characterized by a stationary mounting in the vacuum chamber. The measuring probe is radially (r) and axially (a) movable, in almost the entire discharge volume. Hence, the temporal ion saturation current and the floating potential fluctuation were measured radially $r(t)$ and axially $a(t)$ resolved. This set of data have to be recalculated to a 2d spatially and temporally resolved pattern of the instability. Consequently, one can directly measure the fluctuation in the entire discharge center. It

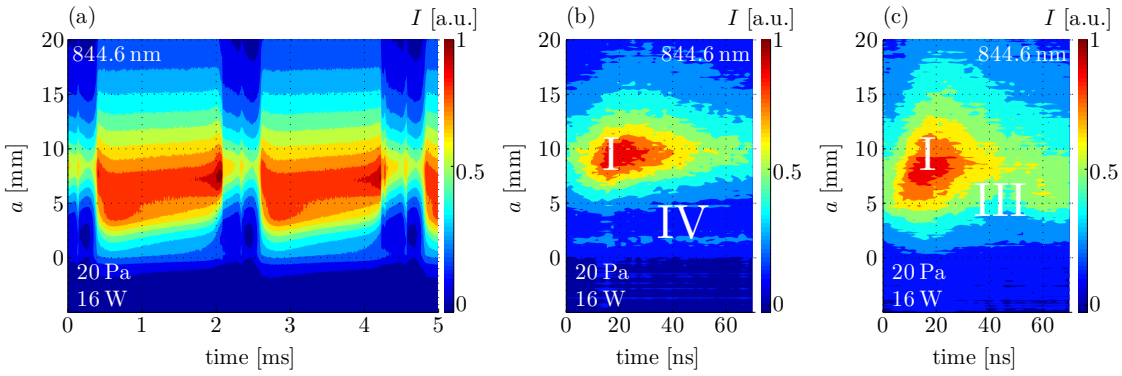

Fig. 4.6.: TROES and PROES of atomic oxygen at 844.6 nm for an oxygen CCRF discharge at 20 Pa and 16 W. (a) Temporally and axially resolved optical emission intensity over about two periods of the instability. RF phase and axially resolved optical emission intensity at the phase position of 1.2 ms (b) and 2.5 ms (c) within the instability.

was shown that these fluctuations are not waves. Moreover, the fluctuations are strongly influencing the RF sheath region.

To investigate the influence of the RF sheath on the instability and vice versa in more detail, the temporally resolved optical emission spectroscopy (TROES) was applied in the millisecond-scale [Fig. 4.6(a)]. The optical emission was measured to be changing during the instability in the RF sheath. This is related to a change in the heating mechanisms. For detailed analysis of the heating mechanisms, the phase resolved optical emission spectroscopy (PROES) was performed in the nanosecond-scale at different phase positions of the instability, namely at 1.2 ms and 2.5 ms [Fig. 4.6(b,c)]. For both points in time the excitation pattern I occurs, which is due to heating during the sheath expansion. The maximum for both points is at the same axial position. For the second time value this excitation pattern is more spread out.

The characteristic heavy particle emission pattern IV of the atomic oxygen in front of the RF powered electrode appears [Fig. 4.6(b)], when the electron density is high, and disappears when the electron density drops. Furthermore, at a low electron density the emission pattern III appears, which is connected to the electric field reversal, and which suggests a high negative ion density, see Fig. 4.6(c). These effects are associated with fluctuations of the mean sheath potential and therefore with the change in heating mechanisms and particle fluxes towards the powered electrode, which have considerable influence on the surface processes. The investigation into and the understanding of these kind of instabilities is one of the future tasks.

5. Summary

The electron and negative ion densities in an asymmetric capacitively coupled low-pressure RF plasma in oxygen were systematically studied and compared to the electropositive argon RF plasma during continuous and pulsed power input. One of the challenges in this work was to measure the electron density without disturbing the plasma itself, in addition to obtaining appropriate diagnostics for electropositive argon and electronegative oxygen plasma. Oxygen was chosen here, because of its reactive and electronegative character, as well as its suitable usage as a model system for a multi-component plasma.

This work presents the careful design and realization of a non-invasive 160.28 GHz Gaussian beam microwave interferometry (MWI) as an innovative diagnostic tool. MWI directly provides the line integrated electron density without any model assumption by the phase shift of the microwave propagation through the plasma, which is due to the change of the plasma refractive index depending on the electron density. The high microwave frequency enables one to accurately describe the microwave free space propagation by means of Gaussian beam theory. The used setup differs from commercially available interferometers due to a sufficient spatial (axial) resolution of 10 mm in combination with a high phase stability and a high temporal resolution of 200 ns. A major challenge of this diagnostics was the measurement of the expected small phase shifts between 0.03° and 0.3°. The microwave interferometry setup was optimized to measure the line integrated electron density with a resolution of $5.3 \times 10^{13}\,\mathrm{m}^{-2}$.

The optimized setup was the basis for the novel approach of simultaneous laser photodetachment and microwave interferometry, in order to experimentally determine the negative ion density in the CCRF oxygen discharge. This is the first time that both diagnostics were combined in low-pressure capacitively coupled RF oxygen plasmas. It is based on the phase shift measurement, which is due to additional electrons produced during the laser pulse by detachment of negative ions, and hence directly provides the line integrated electron density increase. The peak value corresponds to the line integrated negative oxygen ion density, provided that all negative ions are detached within the laser volume during the laser pulse. This was ensured by comparing the theoretically and experimentally measured ratios of the amount of detached electrons to the total amount of steady state negative ions in dependence on the laser energy.

This thesis first presented comprehensive measurements of the steady state line integrated electron density in dependence on RF power and pressure for an argon and oxygen plasma. It was observed that the electron density can be reduced to one graph in dependence on the RF power for different total gas pressure, by considering the pressure dependence of the mean sheath thickness of the collision dominated RF sheath at pressures higher than 30 Pa. This balances the fixed microwave optical axis and the pressure

depending sheath edge. For both gases the electron density increases with RF power. However, the line integrated electron density in oxygen is about a factor 3 to 10 smaller than in argon and amounts to between 10^{14} and $10^{16}\,\mathrm{m}^{-2}$. A further significant observation was the characteristic electron density dip over a specific RF power range in the oxygen discharge. This reduced electron density is accompanied by a high number of negative ions, which exceeded the electron density and resulted in a high electronegativity $\tilde{n}_-/\tilde{n}_\mathrm{e} > 2$. With increasing RF power, the plasma switches into a low electronegative mode with $\tilde{n}_-/\tilde{n}_\mathrm{e} < 1$. Consequently, the discharge operates in two different modes, which are distinguished by their degree of electronegativity. These are the high and the low electronegative mode. It is remarkable that the electropositive argon plasma, which clearly does not show such two modes, can be transferred to a high electronegative mode for low RF power, by adding only a small amount of oxygen. With further oxygen admixture the discharge increasingly strongly shows the separation of the electronegative modes and behaves like a 100 % oxygen discharge. The transition between the high and low electronegative modes is step-like and it was concluded that one can here directly see the discharge switches from the α-mode to the γ-mode.

The γ-mode (low electronegative mode, high RF power) is characterized by a strong increase of the electron density and a simultaneous decrease of the negative ion density. The increase may be connected to the production of secondary electrons by collision detachment of negative ions within the RF sheath ("pseudo-secondary electron"), in addition to the classical γ process due to positive ion bombardment of the powered electrode. This effect was observed by an additional excitation pattern of atomic oxygen due to secondary electrons, being temporal at the maximum of the RF voltage, by means of phase resolved optical emission spectroscopy. Furthermore, these experimental results are confirmed by Particle In Cell-Monte Carlo Collision simulations. In the low electronegative mode, the oxygen plasma behaves like the electropositive argon plasma. Moreover, the γ-mode is characterized by a lower electron temperature of the electrons in the bulk plasma, which reduces the dissociative electron attachment rate coefficient. This explains the lower number of negative ions in the low electronegative mode.

In comparison to the γ-mode the α-mode (high electronegative mode, low RF power) reveals more negative ions than electrons. For the α-mode it was observed the dominance of the excitation patterns from electron heating during sheath expansion phase and during the sheath collapse due to electric field reversal, respectively, by phase resolved optical emission spectroscopy. In the α-mode the experimental results are comparable with fluid model calculations, which show the same excitation patterns due to the sheath expansion and collapse at high electronegativity. The α-mode involves a higher electron temperature in the bulk plasma and consequently a higher efficiency of negative ion production by dissociative attachment, which accounts for the high number of negative ions.

Furthermore, a simple 0d attachment-detachment model was applied to calculate the effective rate coefficients for dissociative electron attachment and collisional detachment from the experimentally determined values of steady state electron and negative ion density, as well as the detachment decay time constant. Hence, the attachment rate coefficient of the molecular ground state k_aX $\left(\mathrm{O}_2\left(\mathrm{X}^3\Sigma_\mathrm{g}^-\right)\right)$ and the excited metastable state

$k_{a\Delta}$ ($O_2\left(a^1\Delta_g\right)$) in dependence on RF power were determined, which were in good agreement with the values from the literature. Moreover, the density of metastable molecular oxygen $O_2\left(a^1\Delta_g\right)$ was estimated to 10 % of the molecular ground state oxygen, which is also comparable to the values found in the literature. The metastable oxygen $O_2\left(a^1\Delta_g\right)$ is therefore of crucial importance in correctly interpreting the experimental data and this work demonstrated its important role within the oxygen discharge.

The influence of each electronegative mode to the entire temporal behavior of the oxygen discharge was intensively investigated by pulsing the discharge. This influence was particularly clear in the afterglow behavior. Here it was shown that for the low electronegative mode the afterglow behavior is similar to that of an electropositive argon plasma. The only difference is the faster electron density decay in oxygen in comparison to argon. This was explained by the additional dissociative recombination in oxygen. In the argon discharge the main loss processes are diffusion and surface recombination.

In the high electronegative mode an electron density peak in the early afterglow was observed. It was concluded that the electron production originates from the collisional detachment of negative ions. The temporal decreasing negative ion density in the early afterglow was measured by laser photodetachment. The negative ion loss and the electron production in the early afterglow were modeled numerically with a 0d rate equation system, while taking into account the particle balance of six species (e^-, O_2^+, O^-, O_2^-, $O_2\left(a^1\Delta_g\right)$, $O\left(^3P\right)$), nine elementary reactions involving recombination, detachment and charge transfer, as well as a loss term due to ambipolar diffusion. The model accurately describes the afterglow behavior of both electronegative modes, as well as the direct electron density decrease for the low electronegative mode, and the additional electron density peak in the early afterglow with the subsequent electron density decay of the high electronegative mode. The parameter studies for the high electronegative mode have shown that the metastable molecular oxygen $O_2\left(a^1\Delta_g\right)$ in particular plays an important role as a detachment partner for the production of electrons in the early afterglow. In summary both the electronegativity and the number of negative ions appear to have a significant influence on the discharge dynamics.

Furthermore, the presence of the negative ions causes fluctuations of plasma parameters, e. g., floating and plasma potential, ion saturation current, electron density and optical emission intensity. The dominance of these instabilities increases with rising pressure. Spatially (axial and radial) and temporally resolved ion saturation current measurements have shown that these fluctuations involve the entire reactor volume. Moreover, the results clearly indicate that these instabilities are not waves. The temporal and phase resolved optical emission spectroscopies (TROES and PROES) provide a deeper insight into the RF sheath dynamics during the instability and at characteristic phases within the instability for one RF cycle. The TROES measurements already show a strong change in emission pattern during the instability, which becomes more obvious for one RF cycle at characteristic instability phases. Here, the emission patterns reveal significant changes in the electron heating mechanisms, which are accompanied by a change in electronegativity during the instability.

A detailed investigation of the instabilities is one of the future tasks, in particular the measurement of the negative ion density to confirm the assumption that the negative ion density is also fluctuating. Thereby, the laser photodetachment experiment has to be phase triggered with the instability, which is a challenging task because of the various frequencies of the 10 Hz pulsed laser and of the instability, which are in the kilohertz range. Apart from the fluctuations the small RF power range characterizing the transition between the high and low electronegative mode also needs to be investigated in more detail. Here in particular, the measurement of the electron and negative ion density has to be intensively performed.

Furthermore, the established innovative diagnostics can also be applied for inductively coupled RF discharge (ICRF) in the same model systems of argon and oxygen. Here the E- to H-mode transition has to be investigated in more detail regarding the influence of different electronegativities. ICRF oxygen discharges in particular are rarely investigated in detail. Finally, some open questions remain regarding the existence of a hysteresis, which have not yet been answered satisfactorily.

This work has provided an in-depth discussion of the transition, as well as the similarities and differences, between an electropositive plasma such as argon and an electronegative plasma such as oxygen. In future research a stronger electronegative CCRF plasma, such as tetrafluoromethane CF_4, should be investigated. CF_4 is also a suitable model system and opens up a wide field of exciting research questions and goals for future studies. One task concerns for example the recently discovered electron heating in drift and ambipolar electric fields (Ω-mode) [157, 158]. Beside the PIC-MCC simulations in symmetric CCRF plasmas in CF_4 and the experimental verification by RF phase resolved optical emission spectroscopy no experimental data are available concerning the measurement of electron and negative ion densities in the CF_4 discharge during the Ω-mode.

In conclusion the well established non-invasive microwave interferometry presented here, with its high sensitivity and high temporal resolution opens up a wide field of new experimental investigations into electron density measurements. As there are currently no detailed investigations into the measurement of negative ions in CF_4 discharges in the literature [159, 160]. The microwave interferometry with simultaneous laser photodetachment presented in this study can be applied for the measurement of electrons and negative ions F^- in CF_4 discharge.

6. Thesis Articles

Author Contribution

This chapter presents the publications achieved during the PhD thesis. The papers are arranged according to their scientific content.

Article I:
"160 GHz Gaussian beam microwave interferometry in low-density rf plasmas"
K Dittmann, **C Küllig** and J Meichsner, *Plasma Sources Sci. Technol.* **21** (2012) 024001 (7pp)
KD has basically prepared the setup of the CCRF discharge and has prepared the diagnostics (microwave interferometer). CK developed a setup for the measurement of the Gaussian beam waist and performed the regarding measurements. CK prepared finally the setup for the electron density measurement and programmed the measurement software. All measurements are performed by CK. The entire manuscript is written by CK. It was edited by all co-authors.
Link: http://Article I

Article II:
"Electron and Negative Ion Analysis in Oxygen Capacitively Coupled Radio Frequency Plasma"
J Meichsner, K Dittmann, **C Küllig**, *Contrib. Plasma Phys.* **52** (2012) 561-570
The measurements are done by CK except the PROES measurements, which are done by KD. The entire manuscript is written by JM and CK. It was edited by all co-authors.
Link: http://Article II

Article III:
"A novel approach for negative ion analysis using 160 GHz microwave interferometry and laser photodetachment in oxygen cc-rf plasmas"
C Küllig, K Dittmann and J Meichsner, *Plasma Sources Sci. Technol.* **19** (2010) 065011 (10pp)
The laser is included into the setup by CK (together with KD). The presented results are achieved by CK. The analytical model for the high electronegative mode was developed by JM and CK. PROES results are from KD. The entire manuscript is written by CK. It was edited by all co-authors.
Link: http://Article III

Article IV:
"Detachment-induced electron production in the early afterglow of pulsed cc-rf oxygen plasmas"
C Küllig, K Dittmann and J Meichsner, *Phys. Plasmas* **19** (2012) 073517
The measurement of the time depending electron and negative ion density are done by CK. The first order rate equation, which describes the negative ion loss and production of electrons are created by CK. The 0d rate equation system was initialized by JM and CK. The implementation, numerical modeling and calculation of the model, was done by CK. The entire manuscript is written by CK and was edited by all co-authors.
Link: http://Article IV

Article V:
"Electron Density Oscillations in CC-RF Oxygen Plasma Investigated by Gaussian Beam Microwave Interferometry"
C Küllig, K Dittmann and J Meichsner, *IEEE Transactions on Plasma Science,* **39** (2011) 2564-2565
The investigation of the instabilities were done by CK. The manuscript is written by CK. It was edited by all co-authors.
Link: http://Article V

Article VI:
"Dynamics and Electronegativity of Oxygen RF Plasmas"
C Küllig, K Dittmann, T Wegner, I Sheykin, K Matyash, D Loffhagen, R Scheider and J Meichsner, *Contrib. Plasma Phys.* **52** (2012) 836–846
The experimental measurements are achieved by CK. The results regarding PROES measurements are achieved by KD. The main part of the manuscript is written by CK. The introduction is written by JM. The introductory part of the fluid model calculation coming from IS and DL. The comparing part between fluid model calculation and the experiment is written by CK. The introductory part for the PIC-MCC is written by KD. It was mainly edited by CK, KD and JM.
Link: http://Article VI

Confirmed:

(Prof. Dr. Jürgen Meichsner) Greifswald, 25. April 2013

Article I

IOP Publishing Plasma Sources Science and Technology
Plasma Sources Sci. Technol. **21** (2012) 024001 (7pp) doi:10.1088/0963-0252/21/2/024001

160 GHz Gaussian beam microwave interferometry in low-density rf plasmas

K Dittmann, C Küllig and J Meichsner

Institute of Physics, University of Greifswald, Felix-Hausdorff-Str. 6, Germany

E-mail: dittmann@physik.uni-greifswald.de, kuellig@physik.uni-greifswald.de and meichsner@physik.uni-greifswald.de

Received 25 July 2011, in final form 13 October 2011
Published 4 April 2012
Online at stacks.iop.org/PSST/21/024001

Abstract
160 GHz Gaussian beam microwave interferometry is realized for electron density analysis in low pressure rf plasmas. Measurement of electron densities lower than 10^{16} m^{-3} with corresponding phase shift less than 0.3° demands high stability of the interferometer frequency and minimum disturbance due to external interfering voltages and mechanical vibrations of the optical components. The interferometer consists of a frequency stabilized (phase lock loop) heterodyne system operating at a frequency of $f_{MWI} = 160.28$ GHz and wavelength of $\lambda_{MWI} = 1.87$ mm, respectively. A quasi-optical setup is used, considering specially designed horn antennas and elliptical mirrors as well as components which have to comply with the aperture limit in relation to the Gaussian microwave beam and its optimal coupling and focusing into the plasma center. A spatial and temporal resolution of about 10 mm (beam waist 5 mm) and 0.2 µs is achieved, respectively. In cc-rf plasma the lowest measurable phase shift is in the order of 0.01°, which corresponds to a line-integrated electron density of about 5×10^{13} m^{-2} or an electron density of 5×10^{14} m^{-3} averaged over the electrode diameter. Results are presented and discussed concerning line-integrated electron density in an asymmetric argon cc-rf plasma in dependence on rf power and total pressure.

(Some figures may appear in colour only in the online journal)

1. Introduction

Radio frequency discharges are frequently used for surface treatment, for the chemical modification and structuring of solid state surfaces, or for vapour deposition of thin films. Despite the widespread application of such plasmas, these are not fully understood. Thus, a fundamental issue of experimental plasma diagnostics is the analysis of the charge carriers in such plasmas to provide information about the reaction kinetics of the plasma itself. Particularly, electrons with their low mass can follow the applied rf voltage and, therefore, are one of the most important quantities characterizing the plasma. Hence, the measurement of electron density is very important. But even the reactive character of the complex plasmas used makes this difficult.

The most prevalent standard method for electron density measurements is Langmuir probe diagnostics. But electrical probe analysis is a strongly invasive diagnostics and can affect the plasma properties drastically [1–3]. Furthermore, complex model assumptions are necessary to interpret the probe characteristics and to determine the plasma parameter of interest, such as the electron density [4, 5]. Even in reactive plasmas there are many disadvantages in using Langmuir probes, such as the formation of high resistance layers on the probe surface [6–10] or the presence of negative ions [6, 11, 12].

Microwave interferometry, as compared with probe diagnostics, is a minimal-invasive method which affords a direct measurement of the line-integrated electron density by the phase shift of the microwave due to the change in electron density without any model assumptions. The electron density is directly coupled with the plasma frequency and, therefore, with the refractive index of the plasma.

Moreover, reactive plasmas have no influence on the microwave diagnostics. Hence, it is even possible to analyse e.g. chlorofluorocarbons using microwave interferometry. Plasma diagnostics with microwaves is a standard method in fusion research and other plasmas with much higher electron densities and dimensions but a challenge in low-temperature, low-density plasmas such as the cc-rf discharges presented

here. Due to the low dimensions of these plasmas in the centimeter range and low electron densities in the order of $10^{16}\,\mathrm{m}^{-3}$ the resulting phase shifts of the probing microwave beam are rather low. These conditions require high quality of the used microwave interferometer; for instance, high frequency stability as well as minimized mechanical vibrations of optical components guiding the microwave beam just enough to achieve a small noise signal to resolve the slight phase shifts from the plasma. At a wavelength of about 1 mm, microwave interferometry has already been applied for electron density analysis in rf plasmas [13–15], leading to a spatial resolution of about 10 mm in the discharge center. This was much better than previous experiments [16–18]. A temporal resolution of about 1 ms could be achieved with a heterodyne interferometer by Niemöller *et al* [13], whereas 1 s temporal resolution was realized by Krämer *et al* [15] but with a pure homodyne interferometer which influences the phase measurement. A much better temporal resolution in combination with a suitable spatial resolution has not yet really been achieved. But this is essential for temporal analysis of the electron density to study the electron density fluctuations due to instabilities, the electrons in the afterglow of pulsed plasmas, and during photodetachment experiments to investigate negative ions [19]. This work describes the design and realization of a high-quality microwave interferometer setup. Furthermore, the line-integrated electron density measured in an argon cc-rf plasma is shown and discussed in dependence on the plasma processing parameters rf power and pressure.

2. Basic concepts

The principle of interferometry is based on the fact that a microwave beam with characteristic amplitude and phase Φ is split into two parts: a measurement and the reference path. Both split microwave beams are finally compared at a detector. On the measuring path the wave is going through the plasma and becomes phase shifted due to the different phase velocity, respectively refractive index, in the plasma. This phase shift is coupled with the electron plasma frequency and allows a direct determination of the line-integrated electron density. In the case that the plasma electron density is much lower than the critical electron density corresponding to the microwave frequency (1), $n_\mathrm{e} \ll n_\mathrm{C}(\omega_\mathrm{MWI})$, the relation between the relative phase shift and the line-integrated electron density in the z-direction can be approximated by (2):

$$\omega_\mathrm{MWI} = \sqrt{\frac{n_\mathrm{C}\,\mathrm{e}^2}{\epsilon_0\, m_\mathrm{e}}}, \tag{1}$$

$$\Delta\Phi = \frac{\pi}{n_\mathrm{C}\,\lambda_\mathrm{MWI}} \underbrace{\int_{z_1}^{z_2} n_\mathrm{e}(z)\,\mathrm{d}z}_{\tilde{n}_\mathrm{e}}. \tag{2}$$

Furthermore, microwave interferometry has to be carefully realized to minimize the influence of

- the beam refraction due to density gradients,
- the mechanical vibrations in the ray trace,
- the components guiding/transmitting the microwave beam,
- the arrangement of discharge electrodes.

Typical laboratory low pressure rf plasmas are characterized by electron densities of about $n_\mathrm{e} \approx 10^{16}\,\mathrm{m}^{-3}$, length scales in the order of 10 cm for the windows, the discharge electrodes and the active plasma zone, as well as some millimetres for the rf plasma sheath thickness in front of the powered electrode. The consideration of all these facts results in the application of a microwave with a frequency of 160 GHz and a wavelength of 1.87 mm. At this frequency, quasi-optical theory has to be applied to describe the free space microwave propagation by a Gaussian beam. The Gaussian beam is characterized by two parameters; the first is the beam radius w given by

$$w = w_0 \cdot \sqrt{1 + \left(\frac{z\,\lambda_\mathrm{MWI}}{\pi\, w_0^2}\right)^2}. \tag{3}$$

The beam radius w describes the $1/e$ decrease in the electric field amplitude at the position z of the beam propagation (optical axis) [20]. λ_MWI is the wavelength of the microwave and w_0 is the minimal beam radius in the focus at $z = 0$, which is the so-called beam waist. It defines the best spatial resolution perpendicular to the beam propagation.

The second important parameter is the curvature radius of the wave front, in the following denoted by R and described by

$$R = z + \frac{1}{z}\left(\frac{\pi\, w_0^2}{\lambda_\mathrm{MWI}}\right)^2. \tag{4}$$

The parameters in this equation are the same as mentioned above in (3).

The beam radius diverges with increasing propagation in the z direction. Hence, the aperture dimensions (mirrors, windows, etc) are the limiting factors of the microwave propagation. The aperture dimension L at a position z of microwave propagation has to be four times greater than the beam radius

$$L(z) \geqslant 4 \cdot w(z) \tag{5}$$

at this position [21]. This ensures a negligible power loss of the microwave beam and obviates the excitation of higher Gaussian modes as well as the disturbance of the beam propagation.

The microwave is passed in microwave rectangular waveguides (D-band) between the microwave interferometer and the horn antennas. The horn antennas realize the transition of the microwave from the waveguide into free space and reversed, respectively, and were specially calculated and manufactured. They are round and non-corrugated. This ensures a high-quality Gaussian beam shape with a beam waist of 4.5 mm. Elliptic mirrors are used to change the propagation direction, refocus the beam and transform the beam waist. The necessary modeling and calculation of the elliptic mirrors for Gaussian beam optics are performed taking into account the Gaussian beam collimation at 160 GHz microwave frequency for optimal spatial resolution under consideration of the beam limitations by the low pressure plasma device as shown in (5). This results in a calculated Gaussian microwave beam which

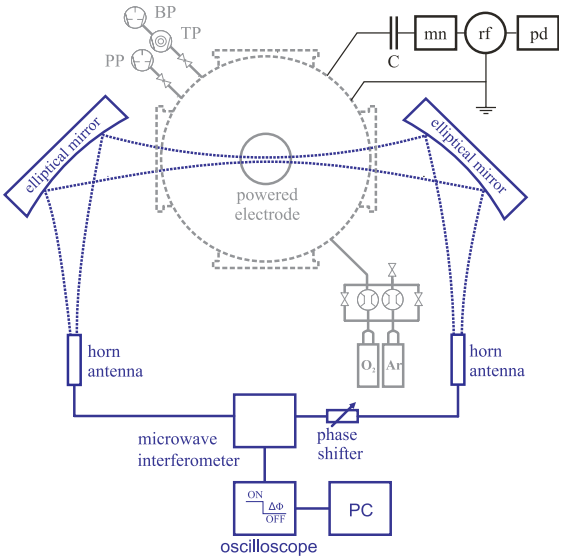

Figure 1. Schematic diagram of the experimental device and the diagnostics, where mn is the matching network, rf is the power supply, pd is the pulse delay generator, PP is the process pump, TP is the turbopump and BP is the booster pump and the microwave interferometer (160.28 GHz).

propagates through the plasma with an optical axis 20 mm above the powered electrode. Here, the beam waist is 5 mm at the center of the electrode, which leads to a spatial resolution of 10 mm. Consequently, two large elliptical aluminium mirrors (Dural®) of size 340 mm width, 240 mm height and 70 mm depth at the thickest part were manufactured on a CNC milling machine according to the calculated data.

3. Experimental setup

3.1. Vacuum chamber and rf discharge

The asymmetric capacitively coupled rf discharge operates at a frequency of 13.56 MHz. The cylindrical vacuum chamber built of stainless steel has a diameter of 400 mm and a height of 400 mm. Four large windows (fused silica) are mounted on the discharge chamber as shown in figure 1. Each window is angled 5° in the horizontal axis to avoid the disturbance of the phase front of the microwave due to interference effects with multiple reflections inside the window material. Furthermore, fused silica has a low absorption coefficient for microwave propagation. The vacuum chamber is pumped by a 660 l s^{-1} turbopump to a base pressure of 5×10^{-5} Pa. The process pressure can be adjusted from 5 to 100 Pa and is obtained by a 16 m^3 h^{-1} stage rotary pump. The gas flow rate is fixed for all experiments at 5 sccm by a mass flow controller (mks 647 C). The effective rotary pump speed is set by a throttle valve to allow the discharge pressure to be controlled independently of the process gas flow.

The planar stainless steel rf electrode with a diameter of 100 mm is arranged 20 mm below the Gaussian beam optical axis. The electrode is powered by the rf generator at 13.56 MHz (ENI ACG-3B) via a fully tunable π-type matching network (ENI MW-10D). The chamber wall and the electrode shielding serve as the grounded electrode. Due to the capacitive coupling and the large surface ratio between the effective grounded and the powered electrode, an asymmetric rf plasma is generated characterized by a negative dc self-bias voltage at the powered electrode. The rf discharge is running at forward rf power of between 5 and 150 W, and a self-bias voltage between −100 and −600 V depending on rf power and discharge pressure.

The low pressure cc-rf plasma is characterized by an electron density between 10^{15} and 10^{16} m^{-3} which approximately results in a line-integrated electron density over the active plasma zone in the range from 10^{14} to 10^{15} m^{-2}. The corresponding relative change in the phase shift for the interferometer is expected to be between 0.03° and 0.3°, only. The detection of such a small phase shift is one of the challenges of this kind of diagnostics. For example, a phase shift of 0.03° corresponds to a 0.16 µm change in the optical path length. To achieve the required mechanical stability the complete experimental setup, i.e. the interferometer components together with the plasma reactor, is mounted on an optical table and massive holders for the wave guiding components, the horn antennas and elliptic mirrors are used. Furthermore, a very stable interferometer frequency is required for maximum signal-to-noise ratio in phase shift measurements.

3.2. Microwave interferometer

The applied microwave interferometer is a frequency stabilized (phase lock loop–PLL) heterodyne system operating at a frequency of 160.28 GHz and a corresponding wavelength of $\lambda = 1.87$ mm (AMTRON, Mikrowellentechnik). The output power of the interferometer is 1.3 mW. Hence, this microwave interferometry is a minimal-invasive diagnostics. Generally, the circuit diagram of the interferometer can be divided into three parts. The first part is the *PLL unit*, where the coupling between the phase of the measurement and reference signal frequency takes place. In detail, the heterodyne system uses a temporal modulation of the microwave phase at the difference frequency ω_0. Therewith, the phase measurement is independent of amplitude and sign of the phase. To achieve this phase modulation the interferometer operates at two different frequencies: one is the measurement signal frequency $\omega_{sig} = 80.14$ GHz and the other is the reference signal frequency $\omega_{ref} = 80.17$ GHz, which are generated by two Gunn oscillators. Thus, the difference frequency ω_0 is 30 MHz. Subsequently, this difference frequency is doubled in the *duplexer 3*, see figure 2, to provide the reference signal with an intermediate frequency of 60 MHz, which is guided to the analyse unit. It is important to couple the two Gunn oscillators in a rigid manner to each other. Briefly explained, this part is an electronic circuit, which couples the phasing of the two Gunn oscillators. They are connected to one special and very stable 60 MHz quartz oscillator. A highly stabilized frequency of the measurement and reference signal is achieved, due to the permanent readjustment of the

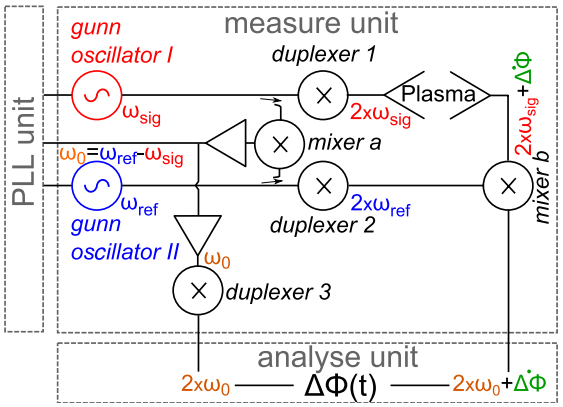

Figure 2. Schematic diagram of the circuit diagram of the microwave interferometer.

generated frequencies by the Gunn oscillators in a closed loop. The second part is the *measurement unit* which includes two pathways. In the measurement path the signal frequency of 80.14 GHz is doubled and the microwave is guided via the D-band waveguide, horn antenna and elliptic mirror to the plasma. After passing the plasma the microwave is received via an elliptical mirror by a second horn antenna and guided via the D-band waveguide forward to the *mixer b*. In the reference path the signal frequency of 80.17 GHz is doubled and directly transferred to the *mixer b*. Here, the frequency doubled reference signal is mixed with the measurement signal to generate a signal at the intermediate frequency of 60 MHz, which additionally contains the relative phase shift from the plasma.

To determine this phase shift, the phasing of the measurement and reference signal, both at the intermediate frequency of 60 MHz, is compared in the *analyse unit*, which is the third part of the circuit diagram (figure 2). The phase measurement is ensured by a phase mixer. Additionally, the analyse unit contains various types of noise filtering components and amplifiers to edit the signals. Here, the temporal resolution of the phase measurement is limited to about 0.2 µs by the electronics (filters, video-amplifier). Finally, the sine of the phase shift ($\sin\Delta\phi$) in units of voltage ($V_{\sin(\Delta\phi)}$) is available at an output of the analyse unit. This sinusoidal shape of the phase shift is important for the measurement and shown in figure 3(*a*):

$$V_{\sin(\Delta\phi)} = \frac{V_{\max} - V_{\min}}{2} \cdot \sin\Delta\phi + \underbrace{\frac{V_{\max} + V_{\min}}{2}}_{V_{\text{off}}}. \qquad (6)$$

The maximum voltage $V_{\max}$ and minimum voltage $V_{\min}$ in (6) have to be measured frequently to ensure a correct determination of the phase shift. An example of the voltage shift in dependence on the phasing of the sine is shown in figure 3(*b*) for a phase shift of 1°. The best phase resolution is achieved in the range of π, where the sine passes zero. The phase shift of 1° causes a voltage shift of about 260 mV, which is suitable for the measurement. Hence, to obtain the best phase resolution the phase signal is adjusted to π by the phase shifter shown in the experimental setup, see figure 1.

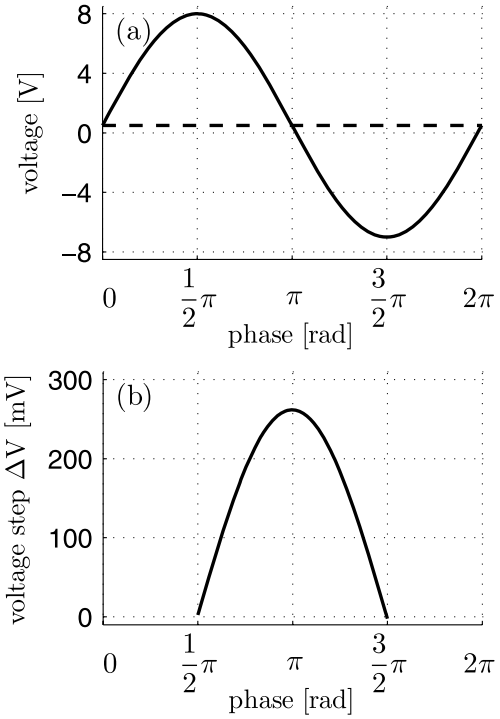

Figure 3. (*a*) The sine of the phase shift $\sin(\Delta\phi)$ (——) in units of voltage ($V_{\sin(\Delta\phi)}$) and the offset (V_{off}) of this signal (- - - -). (*b*) The change in voltage ΔV by a phase change in $\Delta\phi = 1°$ in dependence of the phasing of the microwave signal.

3.3. Measurement of the Gaussian beam radius

The Gaussian beam profile was checked to control the adjusted setup and the properness of the microwave beam propagation. The measurement was carried out in the area between the second elliptical mirror and the receiving horn antenna. Two points have to be examined. Firstly, we have to check the correct position of the maximum microwave power concerning the calculated optical axis, where also the axis of the horn antenna is adjusted. Secondly, we have to measure the Gaussian beam radius and compare with the theoretically calculated one, which is an indication of undisturbed microwave propagation and accurate alignment.

For the beam profile measurement we used a cylindrical ceramic rod of 150 mm length and 1 mm diameter. This rod was mounted on a stepper motor which moves it with its axis perpendicular to the optical axis through the Gaussian microwave beam at different positions z of the microwave propagation. The disturbance of the microwave propagation was detected by means of an oscilloscope. Additionally, a He–Ne laser beam was applied for the indication of the optical axis of the horn antennas. Therewith, the position of the maximum intensity of the Gaussian beam distribution could be determined.

An example for driving the ceramic rod through the microwave beam is shown in figure 4 (black solid line) for a distance of $z = 122$ mm from the receiving horn antenna. By

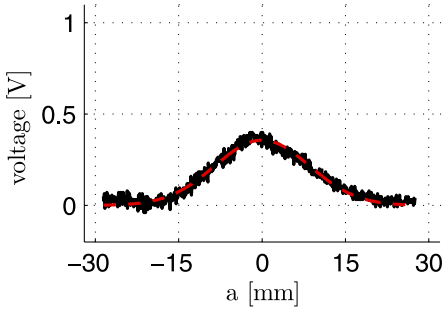

Figure 4. Result of the measured Gaussian beam distribution (——) at $z = 122$ mm. The fitted Gaussian profile (- - - -) is based on the equation $A/(\sigma_{\text{Gauß}} \cdot (2\pi)^{1/2}) \times \exp(-(a - a_0)^2/(2 \cdot \sigma^2_{\text{Gauß}}))$, whereby $A = 7.62$ V mm, $a_0 = 7.17 \times 10^{-5}$ mm and $\sigma^{1/e}_{\text{Gauß}} = 11.95$ mm, providing the $1/e$ decay, which corresponds to the beam radius $\tilde{w}$ at this position.

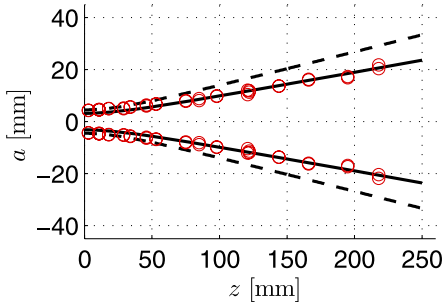

Figure 5. Gaussian microwave beam propagation, where w (- - - -) is the calculated Gaussian beam radius with a beam waist of 4.5 mm, $\hat{w}$ (——) is the Gaussian beam radius divided by $\sqrt{2}$, which corresponds with the intensity distribution of the microwave beam and is in accordance with the experimentally determined beam radius $\tilde{w}$ (○).

fitting a Gaussian distribution onto the measured distribution (dashed line) the radial position was determined for the maximum intensity at $a = 0$ and the $1/e$ intensity decrease at $a \approx 12$ mm, which is the value for the beam radius $\tilde{w}$. The vertical position of $a = 0$ indicates the optical axis of the Gaussian beam, which is perfectly aligned to the optical axis of the horn antennas. Furthermore, we are able to compare the measured beam radius $\tilde{w}$ with the calculated Gaussian beam radius w.

Several such measurements are performed at different positions z in front of the receiving horn antenna which leads to figure 5. There, the measured beam radius $\tilde{w}$ in dependence on the position z does not immediately correspond to the calculated Gaussian beam radius w because of the fact that the measured beam distribution represents the intensity distribution [20] and not the distribution of the electric field amplitude (3). It can be shown that the $1/e$ intensity decrease can be calculated by $\hat{w} = w/\sqrt{2}$. The measured values for the beam radius $\tilde{w}$ fit very well the theoretically calculated Gaussian beam radius $\hat{w}$. In summary, it can be concluded that the calculated Gaussian beam propagation was excellently realized in the experiment.

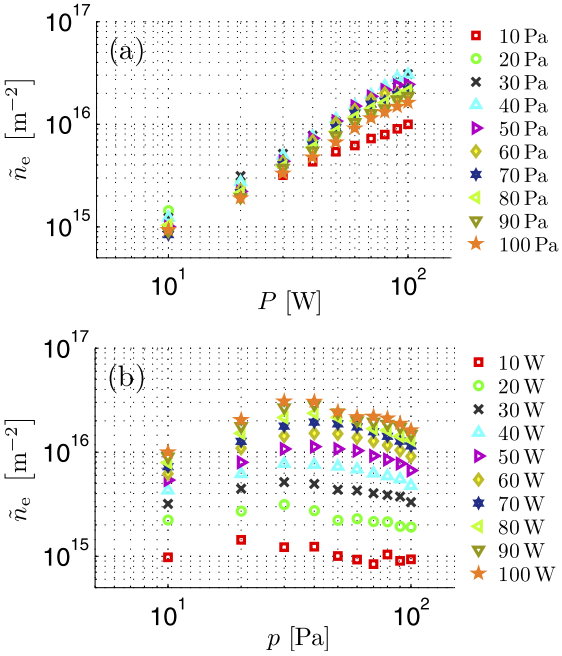

Figure 6. Line-integrated electron density (a) over rf power for different pressure values, (b) over pressure for different power values in an argon plasma for a gas flow rate of 5 sccm.

4. Non-invasive electron density measurements

The measured line-integrated electron densities are shown in figure 6(a), obtained in argon plasma at a fixed gas flow rate of 5 sccm and for different pressure values of 10 to 100 Pa and rf power variation from 10 to 100 W with corresponding self-bias voltages −50 V to −600 V, respectively. Moreover, the electron density in dependence on the argon pressure between 10 and 100 Pa with rf power as parameter is shown in figure 6(b). For each measured point in figure 6 the phase shift in the plasma-on and plasma-off state was determined. The difference between them is the phase shift due to the plasma electrons.

The determined line-integrated electron density ($\tilde{n}_e$) is in the range 10^{15} to 3×10^{16} m^{-2} which was reproducible with high accuracy. The errors are not plotted in figure 6 for reasons of clarity. However, the absolute errors are in the order of 2×10^{15} to 4×10^{15} m^{-2}, which is due to the noise band of the phase signal. It is obvious that with increasing rf power the line-integrated electron density is continuously increasing. The increasing rf power is equivalent to an increasing energy transfer into the plasma. The corresponding heating of electrons results in more ionizing collisions [23], which means the ionization rate (7) is enhanced and the electron density is further increased:

$$\frac{\mathrm{d}n_e}{\mathrm{d}t} = k_{\text{ion}}(T_e) n_e n_{\text{Ar}}. \tag{7}$$

The dependence of the electron density on the pressure at constant rf power (figure 6(b)) is influenced by many factors,

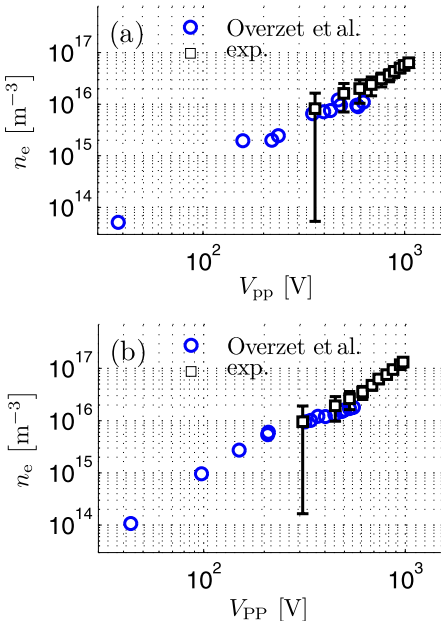

Figure 7. Comparison of the electron density resulting from microwave interferometry (□) and probe measurement (○) by Overzet *et al* [22] in an argon rf plasma over the rf peak-to-peak voltage for (*a*) 13 Pa and (*b*) 33 Pa.

such as the ionization rate depending on the rate coefficient and the neutral argon density, as well as the change in the relative position of the optical axis to the sheath edge of the collisional rf sheath, the ambipolar diffusion out of the active plasma volume and recombination.

To classify the quality of the determined electron densities, a comparison with the literature was made [22]. A comparison of our results with those from probe measurements by Overzet *et al* [22] was made using the averaged electron density (n_e) over the electrode diameter (0.1 m) as an effective path length (see figure 7)

$$\tilde{n}_e = 0.1\,\mathrm{m} \cdot n_e. \tag{8}$$

The electron density is plotted over the peak-to-peak value of the rf voltage for 13 and 33 Pa argon pressure. A good compliance is observed between our results (squares) and the experimental data of Overzet (circles). Moreover, our determined electron densities directly extend the data points measured by Overzet for both pressure values.

The temporal resolution of the microwave interferometry is demonstrated by the electron density decay in the afterglow phase of a 10 Hz pulsed argon plasma (50 Pa, 65 W), figure 8. The typical decay time constant is in the order of about 500 µs. The mentioned high temporal resolution lower than 1 µs was already shown in the electron density relaxation after the laser photodetachment of negative ions in oxygen plasma [19].

5. Conclusions

In this paper, we have carefully designed and realized microwave interferometry at 160.28 GHz to measure rather low line-integrated electron densities in low-density cc-rf plasmas. The setup is optimized to measure phase shifts of about 0.016°, which leads to measurable line-integrated electron densities smaller than 5.3×10^{13} m^{-2}. Microwave propagation is based on Gaussian beam theory, which needs special microwave guiding components as waveguides, horn antennas and elliptical mirrors. The Gaussian beam propagation in the realized experimental setup was experimentally checked due to a controlled disturbance of the microwave beam by a ceramic stick. As a result, very good agreement between the theoretically calculated curve and the experimental determined values was found.

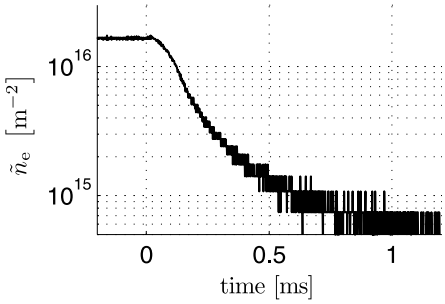

Figure 8. Time dependence of the electron afterglow behavior for 50 Pa, 65 W and 5 sccm argon. The rf power supply is disconnected at $t = 0$.

Subsequently, we successfully applied these diagnostics to an argon cc-rf plasma. Line-integrated electron densities were measured in dependence on pressure and rf power in the range 10^{15} to 3×10^{16} m^{-2}. Moreover, a comparison with the literature shows a comparable electron density. Thus, we have a powerful diagnostic tool for non-invasive electron density measurements with very high sensitivity, a temporal resolution of about 0.2 µs and an adequate spatial resolution of 10 mm. Therewith, we are now able to investigate reactive complex plasmas in further experiments, for example, the fluctuation of the electron density due to instabilities, or the afterglow behavior of a pulsed plasma, as well as to detect electrons being photodetached from negative ions [19].

Acknowledgments

This work was supported by the Deutsche Forschungsgemeinschaft (DFG) in the framework of the Sonderforschungsbereich Transregio 24 'Fundamentals of Complex Plasmas'.

We want to thank Dr M Hirsch and Professor Dr H-J Hartfuss from IPP, Greifswald branch, for helpful discussion and advice in microwave diagnostics. We thank the IPF Stuttgart for the construction of the specific feed-horns.

References

[1] Arndt S, Sigeneger F, Testrich H and Brandt C 2005 Self-consistent analysis of the spatial relaxation of a disturbed neon glow discharge *Plasma Chem. Plasma Process.* **25** 567–94

[2] Brandt C, Testrich H, Kozakov R and Wilke C 2006 Investigation of the disturbance of a Langmuir probe and its influence on measurement results *Rev. Sci. Instrum.* **77** 023504

[3] Demidov V I, Ratynskaia S V and Rypdal K 2002 Electric probes for plasmas: The link between theory and instrument *Rev. Sci. Instrum.* **73** 3409–39

[4] Godyak V A, Piejak R B and Alexandrovich B M 1992 Measurements of electron energy distribution in low-pressure RF discharges *Plasma Sources Sci. Technol.* **1** 36–58

[5] Godyak V A, Piejak R B and Alexandrovich B M 1993 Probe diagnostics of non-Maxwellian plasmas *J. Appl. Phys.* **73** 3657–63

[6] Klagge S 1993 Sondendiagnostik, Weiterbildungskurs Plasmaphysik *Vorlesungsmanuskript Sektion Physik/Elektronik, Universität Greifswald*

[7] Sabadil H, Klagge S and Kammeyer M 1988 Langmuir probe measurements of axial variation of plasma parameters in 27.1 MHz rf oxygen planar discharges *Plasma Chem. Plasma Process.* **8** 425–44

[8] Wehner G and Medicus G 1952 Reliability of probe measurements in hot cathode gas diodes *J. Appl. Phys.* **23** 1035

[9] Thomas T L and Battle E L 1970 Effects of contamination on langmuir probe measurements in glow discharge plasmas *J. Appl. Phys.* **41** 3428

[10] Olson R A and Nordlund D R 1972 Automatic plotting of langmuir probe susceptance and conductance voltage curves *J. Appl. Phys.* **43** 2780

[11] Buddemeier U 1997 Experimentelle Untersuchung einer kapazitiv gekoppelten HF-Entladung in Sauerstoff *PhD Thesis* Ruhr-Universität Bochum

[12] Amemiya H, Yasuda N and Endou M 1994 Negative ion-containing plasma in parallel-plate radio-frequency discharge oxygen *Plasma Chem. Plasma Process* **14** 209–27

[13] Niemöller N, Schulz-von der Gathen V, Stampa A and Döbele H F 1997 A quasi-optical 1 mm microwave heterodyne interferometer for plasma diagnostics using a frequency-tripled Gunn oscillator *Plasma Sources Sci. Technol.* **6** 478–83

[14] Lukas Ch, Müller M, Schulz-von der Gathen V and Döbele H F 1999 Spatially resolved electron density distribution in an RF excited parallel plate plasma reactor by 1 mm microwave interferometry *Plasma Sources Sci. Technol.* **8** 94–9

[15] Krämer M, Clarenbach B and Kaiser W 2006 A 1 mm interferometer for time and space resolved electron density measurements on pulsed plasmas *Plasma Sources Sci. Technol.* **15** 332–7

[16] Hebner G A, Verdeyen J T and Kushner M J 1988 An experimental study of a parallel plate radio frequency discharge: Measurements of the radiation temperature and electron density *J. Appl. Phys.* **63** 2226–36

[17] Greenberg K E and Hebner G A 1993 Electron and metastable densities in parallel-plate radio-frequency discharges *J. Appl. Phys.* **73** 8126–33

[18] Overzet L J 1995 Microwave diagnostic results form the gaseous electronics conference RF reference cell *J. Res. Natl Inst. Stand. Technol.* **100** 401

[19] Küllig C, Dittmann K and Meichsner J 2010 Novel approach for negative ion analysis using 160 GHz microwave interferometry and laser photodetachment in oxygen cc-rf plasmas *Plasma Sources Sci. Technol.* **19** 065011

[20] Goldsmith P F 1998 *Quasioptical Systems* (New York: Wiley-IEEE)

[21] Véron D 1979 Submillimeter interferometry of high-density plasmas *Infrared and Millimeter Waves* vol 2, ed K J Button (New York: Academic) ch 2

[22] Overzet L J and Hopkins M B 1993 Comparison of electron-density measuremets made using a Langmuir probe and microwave interfermoter in the Gaseous Electronics Conference reference reactor *J. Appl. Phys.* **74** 4323–30

[23] Lieberman M A and Lichtenberg A J 1994 *Principles of Plasma Discharges and Materials Processing* (New York: Wiley)

Article II

Contrib. Plasma Phys. **52**, No. 7, 561 – 570 (2012) / **DOI** 10.1002/ctpp.201210052

Electron and Negative Ion Analysis in Oxygen Capacitively Coupled Radio Frequency Plasma

J. Meichsner*, **K. Dittmann,** and **C. Küllig**

Institute of Physics, University of Greifswald, Felix-Hausdorff-Str. 6, 17489 Greifswald, Germany

Received 14 February 2012, accepted 28 February 2012
Published online 16 August 2012

Key words Low pressure rf discharge, oxygen plasma, electron and negative ion density.

Low pressure capacitively coupled radio frequency plasmas (cc-rf plasmas) were investigated by minimal-invasive 160 GHz Gaussian beam microwave interferometry. The interferometer is a frequency stabilized (PLL) heterodyne system which immediately provides the line integrated electron density at spatial (axial) resolution of about 10 mm and temporal resolution of 200 ns. The line integrated electron density was measured in dependence on the processing parameters rf power (10 . . . 100 W) and total pressure (10 . . . 100 Pa) in comparison between argon and oxygen. Thereby, the changed distance between the fixed microwave beam axis as well as the sheath edge is taken into consideration using an analytical collision-dominated sheath model and results from optical emission spectroscopy. Microwave, interferometry and simultaneous laser photodetachment in oxygen plasma additionally permits the measurement of the negative atomic oxygen ion density. Dynamic and transient phenomena in oxygen plasmas are discussed such as mode transitions, afterglow behaviour in pulsed rf plasma, and electron density fluctuations due to attachment-induced ionization instabilities.

.

1 Introduction

The analysis of charged particle densities such as electrons, negative and positive ions is of great interest to understand dynamic and the transient phenomena in cc-rf low pressure plasmas in electronegative gases, e.g. mode transitions, afterglow behaviour in pulsed rf plasmas and instabilities. The electron and ion density analysis of low pressure plasmas is usually performed by electric probe measurements such as single Langmuir or symmetric double probes. But, electrical probe measurements represent an invasive diagnostic technique and can affect the plasma properties drastically [1–3]. Therefore, specific assumptions and tailored models are necessary to get information about the electron density and electron temperature, respectively the electron energy distribution function (EEDF), as well as the ion density from the probe characteristics [4,5]. Furthermore, the chemical surface modification of the probe tip has to be considered in reactive plasmas e.g. by thin film deposition [6–8]. The electron sampling is also strongly influenced by an external magnetic field. Due to their low cyclotron radius the electron transport becomes anomalous and has to be considered separately for parallel and perpendicular direction to the magnetic field lines [1]. In rf plasmas the disturbing rf voltage in the electric probe circuit has to be strongly reduced by suitable compensation methods and electric filter techniques [9].

In this paper, the minimal-invasive microwave interferometry is applied to determine the line integrated electron density immediately. In particular, an overview is given about the application fields of the Gaussian beam microwave interferometry at 160 GHz in low pressure cc-rf plasmas. The successful realization of the microwave interferometry at 160 GHz for analysis of low density plasmas (electron density from 10^{15} to $10^{16}\,\mathrm{m}^{-3}$) was a challenge because of the very low phase shift in the order of between $0.03°$ and $0.3°$. Firstly, the experimental set up including the diagnostic techniques are briefly described. Secondly, the measured line integrated electron density in dependence on rf power and total gas pressure is discussed in comparison between electropositive argon and electronegative oxygen plasmas. The main part of the paper is focused on the cc-rf plasma in oxygen. Here, the electron density measurement by microwave interferometry is combined with simultaneous laser

* Corresponding author. E-mail: meichsner@physik.uni-greifswald.de, Phone: +49 3834 86 4740, Fax: +49 3834 86 4701

photodetachment of negative atomic oxygen ions described in detail by Küllig et al. [10]. Furthermore, dynamic and transient phenomena on different time scales are observed and discussed. This concerns the afterglow behaviour in pulsed oxygen rf plasmas from the µs-range in the early afterglow up to the ms-range. Additionally, the oxygen plasma reveals electron density fluctuations in the frequency range from 0.3 to 3 kHz over wide field of processing parameters.

2 Experimental setup

2.1 Vacuum chamber and rf discharge

The plasma apparatus consists of a cylindrical vacuum chamber built of stainless steel both diameter and height of 400 mm. The chamber is evacuated by a $660\,\mathrm{l s^{-1}}$ turbo pump to a base pressure of 5×10^{-5} Pa. The process pressure of argon respectively oxygen can be adjusted from 5 to 100 Pa and is obtained by a $16\,\mathrm{m^3 h^{-1}}$ stage rotary pump. The gas flow rate is fixed at 5 sccm for all experiments by a massflow controller (MKS 647C). The effective pumping speed is set by a throttle valve to allow the discharge pressure to be controlled independently of the process gas flow. The planar stainless steel rf electrode with diameter of 100 mm is located in the centre of the vacuum chamber and powered by the rf generator at 13.56 MHz (ENI ACG-3B) via a fully tuneable π-type matching network (ENI MW-10D). The chamber wall and the electrode shielding serve as grounded electrode. Due to the capacitive coupling and the large surface ratio between the effective grounded and the powered electrode, an asymmetric rf discharge is generated characterized by a negative DC self-bias voltage at the powered electrode. The rf discharge is running at forward rf power of between 5 to 150 W, and a self-bias voltage from -100 to -600 V depending on rf power and discharge pressure. Four fused silica windows (diameter 150 mm) are mounted on the discharge chamber (fig. 1).

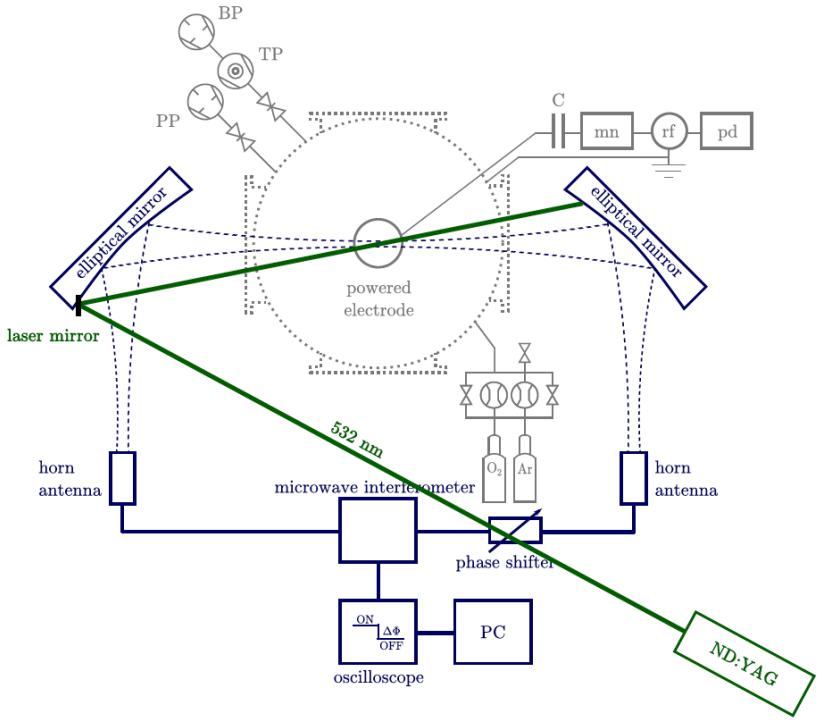

Fig. 1 Schematic sketch of the experimental setup with vacuum equipment for low pressure plasma processing, rf power supply and matching network, as well as the implementation of the 160.28 GHz Gaussian beam microwave interferometer and Nd:YAG laser for photodetachment.

Thereby, each window is angled 5 degree in the horizontal axis to avoid the disturbance of the microwave phase front due to interference effects by multiple reflections inside the window material as well as the direct backscattering of the laser beam into the laser system during the photodetachment experiment. Furthermore, fused silica has a low absorption coefficient for microwave transmission.

2.2 Microwave interferometry and laser photodetachment

The applied microwave interferometer is described in detail by Dittmann et al. [11]. Briefly summarized the microwave interferometer represents a frequency stabilized (PLL) heterodyne system operating at the frequency of $160.28\,\mathrm{GHz}$ with output power of $1.3\,\mathrm{mW}$. Due to its low power, this microwave interferometry provides a minimal-invasive plasma diagnostics. The microwave free space propagation at $160.28\,\mathrm{GHz}$ is realized considering the requirements of the Gaussian beam propagation theory. Therefore, special designed cylindrical horn antennas were applied for careful microwave transformation from the rectangular waveguides into free space and vice versa. Additionally, two matched elliptical mirrors are used to change the propagation direction, refocus the beam, and form the beam waist, which is schematically shown in figure 1. The Gaussian beam waist ($w_0 = 5\,\mathrm{mm}$) determines the axial resolution in the discharges centre which is $10\,\mathrm{mm}$. The confocal length of the microwave beam approximately corresponds to the electrode diameter of $100\,\mathrm{mm}$. The optical axis of the microwave beam is fixed at the distance of $20\,\mathrm{mm}$ above the rf powered electrode. This position is located in the bulk plasma i.e. outside of the rf plasma sheath. The temporal resolution of the microwave interferometer can be adjusted to $200\,\mathrm{ns}$. The low pressure cc-rf plasma is characterized by electron densities between 10^{15} and $10^{16}\,\mathrm{m}^{-3}$. In that case the corresponding relative phase shift is expected of between $0.03\,^\circ$ and $0.3\,^\circ$, only, and means a huge challenge for accurate detection. As an example, the phase shift of $0.03\,^\circ$ corresponds to about $0.16\,\mu\mathrm{m}$ change of the optical path length. Therefore, a mechanically stable construction of the setup is of major importance.

Microwave interferometry and laser photodetachment are simultaneously applied to determine the negative atomic oxygen ion density in a low pressure capacitively coupled rf oxygen plasma [10]. The frequency doubled, $10\,\mathrm{Hz}$ pulsed Nd:YAG laser with expanded beam diameter of $13\,\mathrm{mm}$ was merged with the Gaussian microwave beam under the angle of $12.6\,^\circ$, (fig. 1). By use of appropriate experimental conditions, e.g. laser pulse energy greater than $300\,\mathrm{mJ}$, the detached additional electrons correspond to the negative ions within the overlapping volume of the microwave and laser beam. It has to be noted that the microwave interferometry provides the line of sight integrated electron density. Therefore electric probe measurements are additionally performed to give first information about the radial plasma density distribution along the microwave optical axis. Thereby, the ion saturation current of a passively rf compensated cylindrical Langmuir probe was taken into account. First results show that an effective microwave path length corresponding to the confocal length (electrode diameter) is an appropriate measure for the calculation of mean electron densities in the active plasma zone.

3 Results

3.1 Electron density in argon and oxygen cc-rf plasma

Argon cc-rf plasma Firstly, the electropositive argon plasma was taken into consideration and the line integrated electron density is measured in dependence on the rf power from 10 to $100\,\mathrm{W}$ at different argon pressure of between 10 and $100\,\mathrm{Pa}$. Due to the fixed position of the microwave beam axis with respect to the powered electrode the distance to the rf sheath edge varies with the pressure in the case of collision-dominated rf sheath. Simple analytical calculations can be used to approximate the mean rf sheath thickness d_{coll}. At the condition $\lambda_{\mathrm{ion}} \ll d_{\mathrm{coll}}$ the mobility dominated positive ion current may be applied (1) using the pressure depending ion mobility b_+.

$$j_+ = e \cdot n_+ \cdot v_+ = e \cdot n_+ \cdot \left(-b_+ \cdot \frac{\mathrm{d}\bar{\phi}}{\mathrm{d}z} \right) \qquad \text{with}: \quad b_+ \cdot p = b_{+0} = const \tag{1}$$

The solution of the 1D Poisson equation with time averaged sheath potential $\bar{\phi}$ and the positive space charge density n_+ in the sheath from (1) provides the ion current density $j_{+\mathrm{rf}}$ at the rf electrode (2). With the further

assumption $j_{+\mathrm{rf}} \sim j_{+\mathrm{Bohm}}$ it is achieved an expression for the mean rf sheath thickness d_{coll} in dependence on the total pressure (3).

$$j_{+\mathrm{rf}} \propto \epsilon_0 \cdot b_+ \cdot \frac{\bar{\phi}_{\mathrm{rf}}^2}{d_{\mathrm{coll}}^3} \sim j_{+\mathrm{Bohm}} = e \cdot n_{+0} \cdot \left(\frac{k_{\mathrm{B}} \cdot T_{\mathrm{e}}}{m_+} \right)^{1/2} \tag{2}$$

$$d_{\mathrm{coll}} \propto \left(\frac{\epsilon_0 \cdot b_{+0}}{e \cdot n_{+0}} \cdot \left(\frac{m_+}{k_{\mathrm{B}} \cdot T_{\mathrm{e}}} \right)^{1/2} \right)^{1/3} \cdot (\bar{\phi}_{\mathrm{rf}})^{2/3} \cdot p^{-1/3} \tag{3}$$

Thereby, k_{B}, ϵ_0, e are the Boltzmann constant, the electric field constant and the elementary charge, respectively, as well as m_+ and n_{+0} are the positive ion mass and the density at the sheath edge. In particular, the sheath thickness depends on the mean rf sheath voltage $\bar{\phi}_{\mathrm{rf}}$ and the total pressure p. At constant mean sheath voltage the distance between the microwave beam axis and the sheath edge (20 mm$-d_{\mathrm{coll}}$) increases with the pressure and is scaled approximately with $p^{-1/3}$. Optical emission spectroscopy was applied to estimate the position of the mean rf sheath boundary at the powered electrode in the considered pressure range [12–14]. The experimental results provide the proportionality of the mean sheath thickness with pressure variation by $p^{-1/n}$ where n is between 2 and 4 for argon and oxygen rf plasma. Therefore, the value $n = 3$ is a good estimation to correct the distance between the sheath edge and fixed microwave optical axis. The influence of the total pressure on the ion transport in the rf plasma sheath was also investigated by energy resolved mass spectrometry of extracted positive ions at the discharge electrodes [15,16]. Here, the ion energy distribution function at the powered and grounded electrode in unconfined capacitively coupled rf plasmas revealed a change of the plasma sheath properties with increasing pressure from 5 to 30 Pa due to elastic ion neutral collisions. For example, at the powered electrode and low pressure of about 5 Pa the ion energy distribution function of Ar^+ and O_2^+ is characterized by multiple peak structure due to the overlapping of saddle-shaped pattern from strong modulation of the rf sheath voltage and the charge exchange collisions in the rf sheath [17,18]. At higher pressure from about 30 Pa the low energy part of the ion energy distribution function dominates more and more due to raising elastic ion-neutral collisions. Plotting

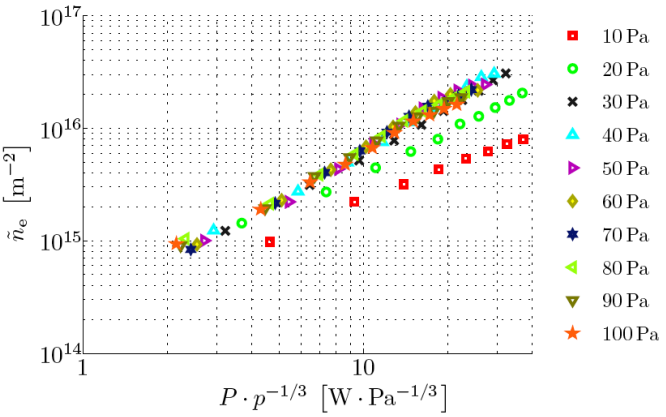

Fig. 2 Line integrated electron density in argon rf plasma at rf power (P) and total pressure (p) variation. The line integrated density is plotted against the rf power times $p^{-1/3}$ which considered the changed distance between sheath edge and microwave axis for collision-dominated rf sheath ($p > 30$ Pa).

the measured line integrated electron density versus the product $P \cdot p^{-1/3}$ the line integrated electron density in dependence on the total pressure shifts in one graph for the case of a collision-dominated rf sheath at pressure higher than about 30 Pa ($d_{\mathrm{coll}}/\lambda_{\mathrm{ion}} > 10$), see figure 2. Due to the characteristic plasma density maximum nearby the rf plasma sheath edge, [19], the scaling by $p^{-1/3}$ balances the changes in the distance between the fixed microwave beam axis and the plasma density maximum as well as the sheath edge, respectively. The line integrated electron density in argon increases with rf power at all pressure values from 10 to 100 Pa and ranges from about 10^{15} to 3×10^{16} m^{-2}, which corresponds to electron density of between 10^{16} and 3×10^{17} m^{-3} using the confocal length as effective path length.

Oxygen cc-rf plasma In figure 3 the influence of the rf power on the line integrated electron density in oxygen is compared with that measured in argon plasma at a total pressure of 30 Pa. Firstly, the line integrated electron

Contrib. Plasma Phys. **52**, No. 7 (2012) / www.cpp-journal.org

density in oxygen is significantly reduced by a half order of magnitude, and secondly, a further electron density dip down to about 2×10^{14} m^{-2} appears between 20 and 50 W in the oxygen plasma. Obviously, this phenomenon is connected with increasing negative ion density in the oxygen plasma. The simultaneous laser photodetachment of negative atomic oxgyen ions confirms this observation. As an example, a characteristic laser photodetachment signal measured by the microwave interferometer is shown in figure 4. Immediately after the laser pulse a sharp increasing electron density in addition to its background value is observed followed by the electron density relaxation with time constant of few µs. The peak electron density corresponds to the detached electrons and is a measure for the line integrated negative ion density in the overlapping volume between microwave and laser beam. Furthermore, the ratio between the line integrated negative ion and background electron density $\tilde{n}_-/\tilde{n}_\mathrm{e}$ characterizes the electronegativity of the oxygen plasma. Therefore, the electron density dip reveals a transition to the strong electronegative mode of the oxygen rf plasma with negative ion to electron density ratio $\tilde{n}_-/\tilde{n}_\mathrm{e} > 2$. For the given example in figure 3 the line integrated negative ion density amounts to about 10^{15} m^{-2}.

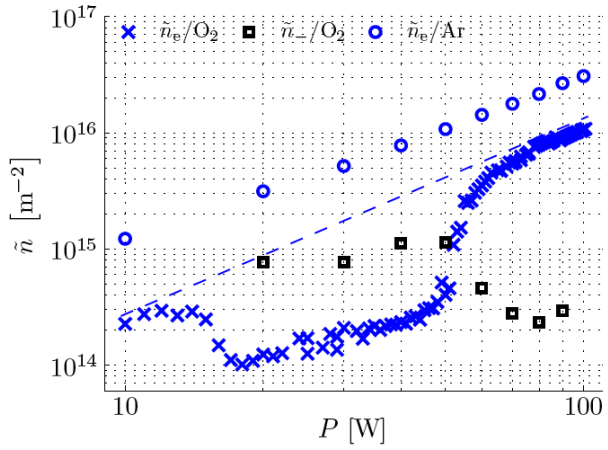

Fig. 3 Comparison of the line integrated electron density $\tilde{n}_\mathrm{e}$ between argon (○) and oxygen (×) rf plasma at 30 Pa and rf power variation from 10 to 100 W. The oxygen plasma provides lower electron density, and additionally a significant electron dip with equivalent increase of the negative ion density $\tilde{n}_-$ (□).

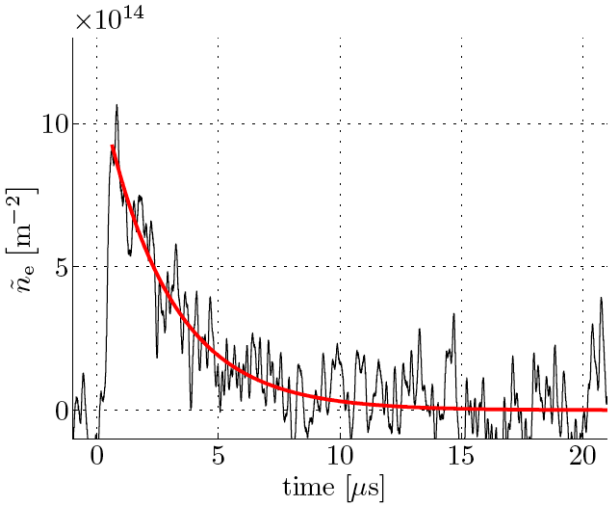

Fig. 4 Example of measured detachment signal in oxygen rf plasma at pressure of 50 Pa, rf power of 40 W and self-bias voltage of -150 V.

At higher rf power the electron density is increasing again, and the oxygen plasma shows rather electropositive behaviour characterized by negative ion to electron density ratio $\tilde{n}_-/\tilde{n}_\mathrm{e} < 1$. The increasing electron density at higher rf power may be combined with a transition from the α- to the γ-heating mode in the capacitively coupled rf discharge [20,21]. Additional phase resolved optical emission spectroscopy supports this assumption, see figure 5. The spatially and rf phase resolved oxygen excitation rate pattern significantly changes for the

considered atomic oxygen line at 844 nm comparing the oxygen plasma at low and high rf power for the total pressure of 100 Pa, [14,22,23]. At higher rf power the detachment of negative ions in the sheath region has to be considered which generates secondary electrons heated in the expanded rf sheath.

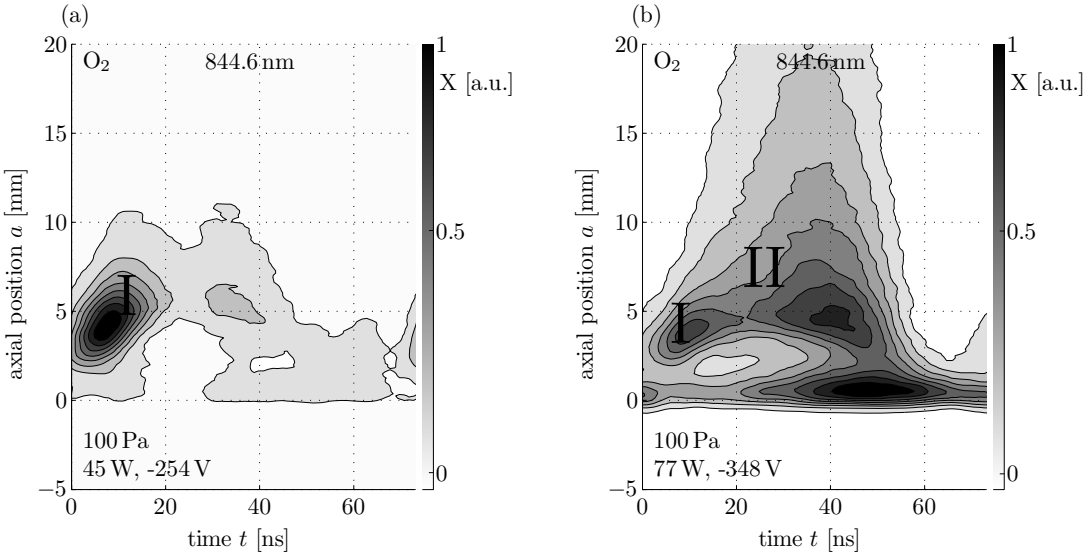

Fig. 5 Axially and rf phase resolved excitation rate X for the corresponding atomic oxygen emission at 844 nm in oxygen rf plasma at 100 Pa [14,22]: a) Excitation pattern (I) reveals the electron heating in the α-mode during the sheath expansion phase, b) additional excitation pattern (II) due to secondary electrons in the γ-mode at higher rf power respectively self-bias voltage.

The influence of the total pressure on the rf sheath thickness is similar to that observed in argon plasmas, that means the graphs of the line integrated electron density versus the product $P \cdot p^{-1/3}$ match approximately in one graph at pressure between 30 and 100 Pa, see figure 6. Thereby, the characteristic electron density dip at increasing rf power in oxygen plasma is well observed, but the onset rf power to the transition in the strongly electronegative mode shifts to higher values with increasing pressure (fig. 6).

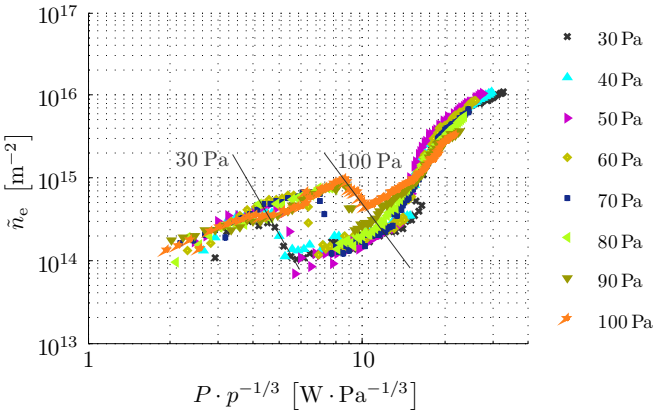

Fig. 6 Line integrated electron density over rf power times sheath thickness $d_{\mathrm{coll}} \propto p^{-1/3}$ for different pressure values in an oxygen plasma for a gas flow rate of 5 sccm.

To achieve first information about the spatial plasma density distribution in oxygen plasma the radial behaviour of the saturation current of positive oxygen ions were measured by rf compensated Langmuir probe at different distances to the powered electrode, see figure 7. From this probe measurement two results are obtained. Firstly, the electrode diameter respectively the confocal length may be used as a measure for the effective line of sight

in microwave interferometry to estimate radial averaged electron density from the line integrated values. In the considered range of processing parameters the line integrated electron density ranges from about 10^{14} to $10^{16}\,\mathrm{m}^{-2}$ which corresponds to averaged electron densities of between 10^{15} and $10^{17}\,\mathrm{m}^{-3}$ using the effective microwave path length. Secondly, the probe measurement at different axial distances to the powered electrode confirms the increasing plasma density towards the rf sheath edge. The variation of the plasma density in axial direction at constant pressure reveals the similar influence on the distance between the rf sheath edge and the fixed microwave optical axis by pressure variation, discussed above.

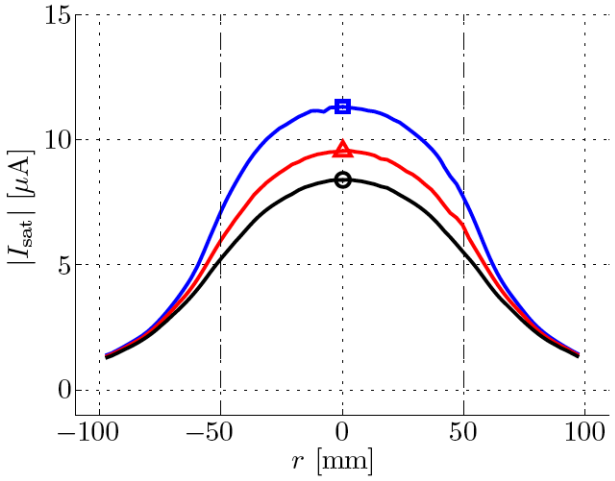

Fig. 7 Radially resolved positive ion saturation current in oxygen rf plasma at 30 Pa and 50 W for three axial distances to the powered electrode: $a = 14$ mm (□), $a = 20$ mm (△) the position of the microwave beam axis, and $a = 26$ mm (○). The chain lines at the radial positions of +/-50 mm assign the rf electrode boundary.

3.2 Electron density in pulsed oxygen cc-rf plasma

The measurements were performed in pulsed rf plasmas at 10 Hz pulse frequency and 50 % duty cycle. Thereby, the minimal measurable phase shift is in the order of $0.016\,^{\circ}$, which corresponds to a measurable line integrated electron density down to $5 \times 10^{-13}\,\mathrm{m}^{-2}$ and an averaged electron densitiy of $5 \times 10^{-14}\,\mathrm{m}^{-3}$, respectively, using the effective microwave path length. The measurements in the on-phase of the pulsed plasma provide the same line integrated electron densities as the measured densities in the corresponding cw mode, but the signal to noise ratio could be increased by the factor 10. The afterglow behaviour of the electron density is shown in figure 8 for the argon plasma at 30 Pa and 32 W.

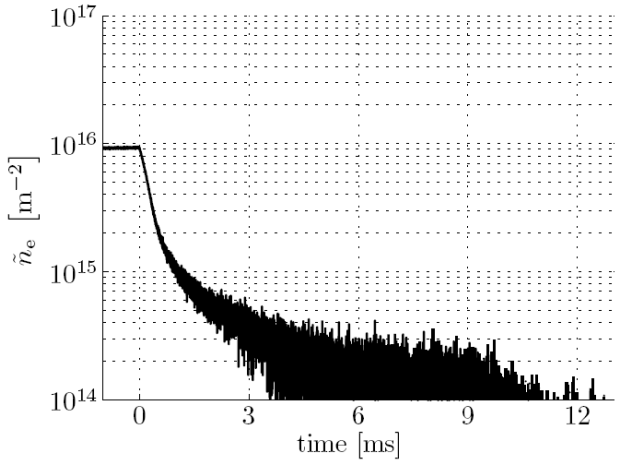

Fig. 8 Temporal behaviour of the line integrated electron density in the plasma-off phase (afterglow) of 10 Hz pulsed oxygen rf plasma at 30 Pa and 91 W.

The electron density decreases as expected with a time constant of between 1 and 2 ms. This behaviour of the line integrated electron density in pulsed rf plasmas exemplarily stands for investigations over wide range of processing parameters. A contrary behaviour was observed in oxygen plasma within specific range of the processing parameters rf power and pressure as exemplarily shown in figure 9. A significant increase of the line integrated electron density was measured in the early afterglow of the oxygen plasma within 200 up to 500 µs after switching off the rf power. Afterwards a decreasing electron density is measured with time constant of few milliseconds like that in the electropositive gas. This increasing electron density was only measured in oxygen plasma, and for rf power lower than 50 W over a pressure range from 20 to 100 Pa. Taking into consideration the strong electronegativity in rf oxygen plasmas at rf power below 50 W (fig.3), the most plausible explanation is the electron production due to detachment of negative ions by metastable oxygen molecules in the early afterglow. The important role of metastable oxygen molecules in elementary processes for production and loss of negative atomic oxygen ions is already discussed in [10]. Furthermore, at special processing parameters the electron density increase was measured being more than one order of magnitude higher than the line integrated electron density in the on phase of the discharge.

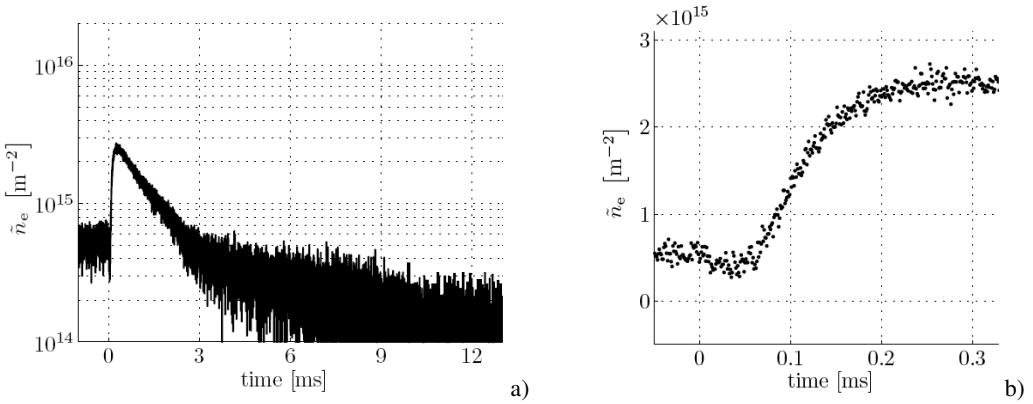

Fig. 9 Temporal behavior of the line integrated electron density in the plasma-off phase (afterglow) of 10 Hz pulsed oxygen rf plasma at 30 Pa and 32 W a). Zoomed electron production in the early afterglow phase b).

Increasing electron densities in the early afterglow plasma were already observed and reported in the literature. Brockhaus et al. [24] has found an electron density increase in the early afterglow in an inductively coupled rf oxygen plasma including the interpretation by fluid modeling. Beside oxygen plasmas, a raising electron density in the early afterglow plasma was also measured in helium plasmas by Greenberg and Hebner [25] as well as Overzet [26], and in hydrogen cc-rf plasma by Gaman et al. [27] using Langmuir probe diagnostics.

3.3 Attachment-induced ionization instability in oxygen plasma

Using the high temporal resolution of 200 ns the electron density fluctuations in oxygen plasma were measured over wide field of processing parameters rf power and pressure. Figure 10 shows exemplarily the non-harmonic electron density fluctuation over the background electron density at 100 Pa and 52 W.
An overview about the electron density fluctuations provides figure 11 for the oxygen plasma at constant total pressure of 50 Pa and rf power variation from 10 to 100 W.

Stable oxygen plasmas are found at rf power between 20 and 50 W, only. In all other cases, the electron density fluctuations are observed at various amplitude and frequency. Generally, stable islands in the investigated oxygen rf plasma are observed at low pressure values within a specific rf power range (fig.11), whereas the oxygen plasma is dominated by instabilities at pressure higher than 60 Pa. The frequency of the electron density fluctuations is reaching from 100 Hz to 3 kHz and the peak to peak value of the line integrated electron density fluctuations varies according to $\Delta\tilde{n}_e = (0.25 \ldots 3.5) \times 10^{15}$ m^{-2}. The origin of the electron density fluctuations is an interaction between the electron density and electron temperature and their influence on the attachment and ionization kinetics, which can be attributed to an attachment-induced ionization instability [28–34]. In more detail

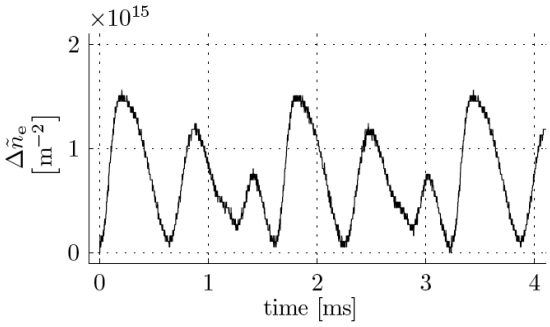

Fig. 10 Electron density fluctuations due to attachment induced ionization instability in oxygen rf plasma at 100 Pa and 52 W.

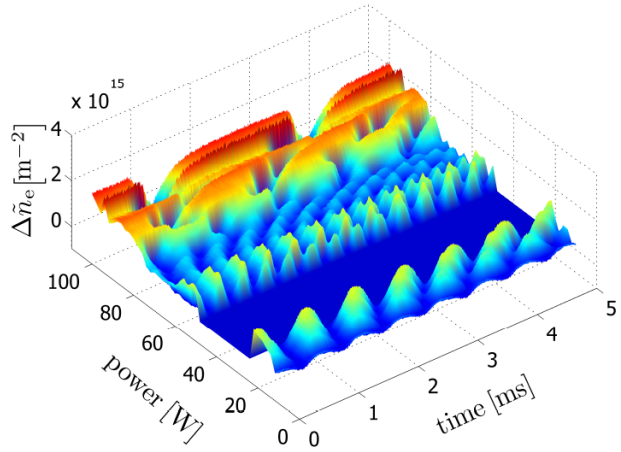

Fig. 11 Overview about the appearance of electron density fluctuations in oxygen rf plasma at 50 Pa and rf power variation from 10 to 100 W. Stable oxygen rf plasma is found between 20 and 50 W, only.

a small initial increase of the electron density is leading to a shift of the equilibrium state between ionization and electron attachment processes. Thereby, an additional and rapid increase of the electron density via a decrease in electron temperature is possible in electronegative gases under special conditions. Consequently, the plasma becomes unstable and the electron density fluctuations take place. Because of the strong coupling of the electron fluctuation with attachment processes it is possible to assume that these fluctuations are equivalent to fluctuations of the negative ion density. Similar fluctuation in optical emission intensity and electron density have been also observed by dust injection or growing dust particles in an rf-plasma. Thereby, the dust grains play a similar role as negative ions, so the electron attach to them and, hence, a reduction of the electron density in the plasma is observed, [35,36].

4 Summary and conclusions

This paper reported about the analysis of line integrated electron density by 160 GHz Gaussian beam microwave interferometry in low pressure cc-rf plasmas. The line integrated electron density was measured in dependence on rf power and pressure for an argon and oxygen plasma. Considering the pressure dependence of the sheath thickness of the collision dominated rf sheath at pressure greater than 30 Pa ($d_{\mathrm{coll}} \propto p^{-1/3}$), the electron density in dependence on the rf power for different total pressure can be reduced to one graph. Thereby, the changed distance between the fixed microwave beam and the sheath boundary is balanced. Comparing oxygen with argon rf plasma, the line integrated electron density in oxygen plasma ranges from 10^{14} to 10^{16} m^{-2} which is by a factor of between 3 and 10 lower than the density in the electropositive argon plasma. Furthermore, a characteristic electron density dip over a specific range in the rf power variation is found. This reduced electron density is connected with a transition into a strong electronegative mode of the oxygen plasma characterized by a negative ion to electron density ratio greater than two. The density of negative atomic oxygen ions was measured by microwave interferometry and simultaneous laser photodetachment. At higher rf power the line

integrated electron density increases again which is connected with a transition to a weak electronegative mode with $\tilde{n}_-/\tilde{n}_e < 1$. This transition may be combined with a transition from the α- to the γ-mode of capacitively coupled rf plasma. In 10 Hz pulsed oxygen rf plasma it was found an effective electron production in the early stage of the plasma-off phase at specific processing parameters, lower than 40 W in the pressure range from 20 to 100 Pa. This electron density increase is mainly related to the detachment of negative atomic oxygen ions in collisions with metastable molecular oxygen. Furthermore, fluctuations of the electron density in oxygen rf plasma were found over wide field of processing parameters rf power and pressure. These fluctuations have their origin in attachment induced ionization instability.

Further investigations are necessary to study the spatial plasma density distribution by probe measurements in order to calculate local electron densities by deconvolution of the line integrated electron density from microwave interferometry. The observed mode transitions have to be studied in more detail.

Acknowledgements This work was supported by the Deutsche Forschungsgemeinschaft (DFG) in the framework of the Sonderforschungsbereich Transregio 24 "Fundamentals of Complex Plasmas", project B5.

References

[1] V.I Demidov, S.V Ratynskaia, and K. Rypdal, Rev. Sci. Instrum **73**, 3409 (2002).
[2] S. Arndt, F. Sigeneger, H. Testrich and C. Brandt, Plasma Chemistry and Plasma Processing **25**, 567-594 (2005).
[3] C. Brandt, H. Testrich, R. Kozakov and C. Wilke, Rev. Sci. Instrum **77**, 023504 (2006).
[4] V.A Godyak, R.B Piejak and B.M Alexandrovich, Plasma Sources Sci. Technol. **1**, 36-58 (1992).
[5] V.A Godyak, R.B Piejak and B.M Alexandrovich, J. Appl. Phys. **73**, 3657-3663 (1993).
[6] U. Buddemeier, Experimentelle Untersuchung einer kapazitiv gekoppelten HF-Entladung in Sauerstoff, PhD thesis, Ruhr-Universitt Bochum, 1997.
[7] H. Sabadil, S. Klagge und M. Kammeyer, Plasma Chemistry and Plasma Processing **8**, 425-444 (1988).
[8] S. Klagge, Vorlesungsmanuskript Sektion Physik/Elektronik p. Universität Greifswald (1993).
[9] U. Flenders, B.H Nguyen Thi, K. Wiesemann, N.A Khromov, and N.B Kolokov, Plasma Sources Sci. Technol. **5**, 61-69 (1996).
[10] C. Küllig, K. Dittmann and J. Meichsner, Plasma Sources Sci. Technol. **19**, 065011 (2010).
[11] K. Dittmann, C. Küllig and J. Meichsner, Plasma Sources Sci. Technol. p. accepted (2012).
[12] N. Mutsukura, K. Kobayashi, and Y. Machi, J. Appl. Phys. **68**, 2657-2660 (1990).
[13] K. Dittmann, Detailed Investigations of the Sheath Dynamics and Elementary Processes in Capacitively Coupled RF Plasmas, PhD thesis, Institute of Physics, Ernst-Moritz-Arndt University of Greifswald , 2009.
[14] K. Dittmann, D. Drozdov, B. Krames and J. Meichsner, J. Phys. D: Appl. Phys. **40**, 6593-6600 (2007).
[15] M. Zeuner and J. Meichsner, Vacuum **46**, 151-157 (1995).
[16] M. Zeuner, H. Neumann and J. Meichsner, Jpn. J. Appl. Phys. **36**, 4711-4716 (1997).
[17] C. Wild and P. Koidl, J. Appl. Phys. **69**, 2909-2922 (1991).
[18] M. Zeuner, H. Neumann, and J. Meichsner, J. Appl. Phys. **81**, 2985-2994 (1997).
[19] J. Meichsner, M. Zeuner, B. Krames, M. Nitschke, R. Rochotzki and K. Barucki, Surface and Coatings Technology **98**, 1565-1571 (1998).
[20] S. Klagge, Plasma Chemistry and Plasma Processing **12**, 103-128 (1992).
[21] Ph. Belenguer and J.P Boeuf, Phys. Rev. A **41**, 4447-4459 (1990).
[22] K. Dittmann, K. Matyash, S. Nemschokmichal, J. Meichsner and R. Schneider, Contributions to Plasma Physics **50**, 942-953 (2010).
[23] S. Nemschokmichal, K. Dittmann, and J. Meichsner, IEEE Transactions on Plasma Science **36**, 1360 (2008).
[24] A. Brockhaus, G.F Leu, V. Selenin, Kh. Tarnev and J. Engemann, Plasma Sources Sci. Technol. **15**, 171-177 (2006).
[25] K.E Greenberg and G.A Hebner, J. Appl. Phys. **73**, 8126-8133 (1993).
[26] L.J Overzet, J. Res. Natl. Inst. Stand. Technol. **100**, 401 (1995).
[27] C. Gaman, S.K Karkari and A.R Ellingboe, Observation of transient electron density rise in an afterglow H2 plasma with confined capacitive radio-frequency source, in: 28th ICPIG, July 15-20, (2007).
[28] H.-M. Katsch, A. Goehlich T. Kawetzki, E. Quandt and H.-F. Döbele, Appl. Phys. Lett. **75**, 2023-2025 (1999).
[29] A. Descoeudres, L. Sansonnens and Ch. Hollenstein, Plasma Sources Sci. Technol. **12**, 152-157 (2003).
[30] W.L Nighan and W.J Wiegand, Physical Review A **10**, 922-945 (1974).
[31] M.A. Lieberman, A.J. Lichtenberg and A.M. Marakhtanov, Appl. Phys. Lett. **75**, 3617-3619 (1999).
[32] P. Chabert, A.J. Lichtenberg, M.A. Lieberman and A.M. Marakhtanov, Plasma Sources Sci. Technol. **10**, 478-489 (2001).
[33] M. Tuszewski and R.R. White, J. Appl. Phys. **94**, 2858-2863 (2003).
[34] C. Küllig, K. Dittmann and J. Meichsner, IEEE Trans. Plasma Science **39**, 2564 (2011).
[35] H. Kersten, U.H. Deutsch, M. Otte, G.H.P.M. Swinkels, G.M.W. Kroesen, Thin Solid Films **377-378**, 530-536 (2000).
[36] M. Mikikian, L. Couedel, M. Cavarroc, Y. Tessier, Y. and L. Boufendi, IEEE Transactions on Plasma Science **36**, 1012-1013 (2008).

Article III

IOP Publishing Plasma Sources Science and Technology
Plasma Sources Sci. Technol. **19** (2010) 065011 (10pp) doi:10.1088/0963-0252/19/6/065011

A novel approach for negative ion analysis using 160 GHz microwave interferometry and laser photodetachment in oxygen cc-rf plasmas

C Küllig, K Dittmann and J Meichsner

University of Greifswald Institute of Physics, Felix-Hausdorff-Str. 6,17489 Greifswald, Germany

E-mail: meichsner@physik.uni-greifswald.de

Received 15 June 2010, in final form 28 August 2010
Published 16 November 2010
Online at stacks.iop.org/PSST/19/065011

Abstract
Microwave interferometry at 160.28 GHz with Gaussian beam propagation (beam waist: 5 mm) and laser photodetachment were combined for the analysis of negative atomic oxygen ions in the bulk plasma of an asymmetric capacitively coupled 13.56 MHz discharge (cc-rf). The line-integrated negative oxygen ion density amounts to between 2.5×10^{14} and 10^{15} m^{-2} depending on the oxygen pressure and rf power. Furthermore, the measured decay of the detachment signal reveals two modes of rf oxygen plasma characterized by different electronegativities. High electronegativity, $\alpha > 2$, is associated with a low decay time constant of only a few microseconds, whereas in oxygen plasmas with low electronegativity, $\alpha < 1$, the relaxation of electron density needs much longer with typical decay time constants of up to about 100 μs. The transition between the two modes shows a step-like characteristic and was observed at a specific rf power depending on the oxygen pressure. In the case of high electronegativity the electron density relaxation can be described by a simple 0D-attachment–detachment model, taking into consideration a constant density for positive ions and neutral oxygen species. Using the appropriate rate coefficients from the literature and the experimentally determined effective rate coefficients of first order kinetics, the evaluation of the attachment and detachment rates indicates the significant role of $O_2(a\,^1\Delta_g)$ in the formation and loss of negative atomic oxygen ions.

(Some figures in this article are in colour only in the electronic version)

1. Introduction

The formation and presence of negative ions have a strong influence on plasma kinetics in low-temperature reactive plasmas. In particular, negative ions significantly determine the charged species balance and the electron energy distribution function. The well-known attachment-induced ionization instability in oxygen plasmas represents a prominent example [1–6]. Under special conditions, such as when using strongly electronegative gases (halogens) or in the case of the decaying plasma in the afterglow, the ion–ion plasma can be observed [7]. The negative ions also play an important role in the formation of dust particles in organic molecular plasmas [8]. In this case they are involved in the generation of species with a higher molecular weight by associative detachment reactions. Furthermore, the negative ions influence the charged species transport and the plasma sheath condition. For a ratio between negative ion and electron density of $\alpha > 2$, a dramatic change in the plasma sheath properties must be expected [9], and further investigations have shown the formation of a double layer [10]. Finally, negative ions produced at the electrode surface or inside the high voltage rf plasma sheath are accelerated towards the bulk plasma [11] or they contribute to additional 'secondary electrons' due to detachment reactions inside the sheath [12].

Negative ion analysis in low pressure electronegative plasmas is usually realized by means of a Langmuir probe within the volume of a pulsed laser beam measuring the electron current increase due to the laser photodetachment [13, 14]. This technique provides localized data on negative

Plasma Sources Sci. Technol. **19** (2010) 065011 C Küllig *et al*

ion density. However, electrical probe measurements represent invasive diagnostics and may affect the plasma properties [15–17]. The interaction of the laser pulse with the probe material may have additional effects. Moreover, various model assumptions are necessary to determine negative ion densities from probe characteristics [18–20]. In the positive column of a dc oxygen discharge the radially averaged negative ion density was measured by means of laser photodetachment over the complete column diameter, using the anode as the electron sampling probe [21].

In this paper 160 GHz microwave interferometry is used to measure the electrons detached from negative ions due to laser photodetachment. There are many advantages to using microwave interferometry instead of standard probe diagnostics. Principally, it represents minimal-invasive diagnostics which can be applied in reactive as well as electronegative plasmas without any restrictions. No model assumption is necessary for measuring the line-integrated electron density and the corresponding negative oxygen ion density from the detached electrons.

Microwave interferometry at a wavelength in the millimeter range has already been applied to electron density analysis in rf plasmas [22–24]. Plasma diagnostics using microwave interferometry (90 GHz) and simulations was recently applied to the determination of electrondensity in the plume of Hall thrusters [25, 26]. Negative ion analysis has been performed in fluorocarbon plasmas [27] using a photodetachment and microwave cavity technique, in SF_6/Ar rf plasma (ICP) [28] by 80 GHz microwave interferometry and in a C_4F_8 plasma (ICP) using a microwave resonance probe [29].

Nevertheless, there are no extensive investigations and published results concerning the combination of microwave interferometry at 160 GHz and laser photodetachment in low pressure oxygen rf plasmas, for the experimental determination of low electron and negative oxygen ion densities with such spatial (beam waist: 5 mm) and temporal (μs) resolutions. The main reason is that the resulting phase shift due to the additionally detached electrons at 160 GHz in low density rf plasmas is only in the order of magnitude of about 0.01°, but contrarily it provides a sufficient spatial resolution by the use of Gaussian beam propagation. Consequently, a careful construction and realization of the setup is absolutely necessary, including the calculation of the Gaussian beam, special horn antennas to enable an optimal transfer of the microwave into the free space, and elliptical mirrors for redirection and refocusing of the microwave.

The laser photodetachment technique concerns the measurement of electrons released due to the interaction of photons with negative atomic oxygen ions, see (1) [30].

$$O^- + h\nu \rightarrow O + e. \quad (1)$$

The detachment of an electron from a negative atomic oxygen ion needs a minimum laser photon energy of 1.46 eV [31]. Therefore, a frequency doubled Nd : YAG laser at a wavelength of 532 nm and a photon energy of 2.3 eV is necessary for laser photodetachment.

Generally, besides the atomic negative ion O^-, the molecular ions O_2^- and O_3^- can be present in oxygen plasmas and require laser photodetachment energies of 0.44 eV and 2.1 eV, respectively [32]. Measurements by Katsch *et al* in low pressure rf plasmas showed O_2^- density to be less than 2% of the atomic negative ion density [20]. They did not consider O_3^- in their investigations. These results are in good agreement with the PIC–MC simulation of cc-rf plasma [30] and an optogalvanic study [33] that also indicates a negligible O_2^- density. Other investigations of rf plasmas show that the density of O_2^- and O_3^- is only about 10% of the total negative ion density [31, 32]. In conclusion, the assumption of only considering negative atomic oxygen ions in the investigated rf plasmas is justified.

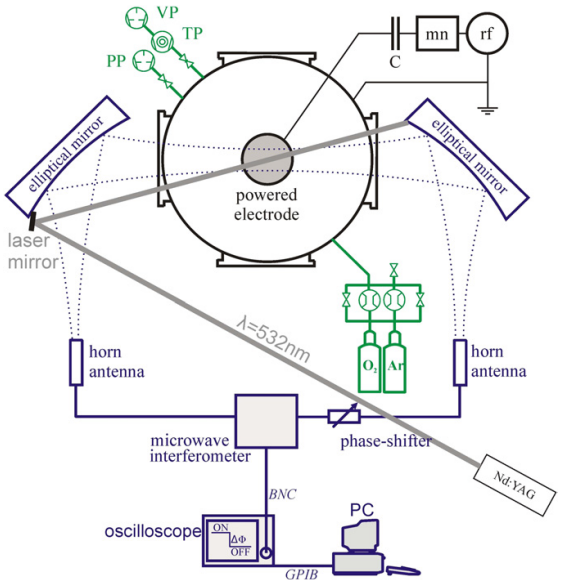

Figure 1. Schematic representation of the experimental setup consisting of vacuum chamber, discharge electrode, process gas and rf power supply as well as diagnostics by means of microwave interferometry and laser photodetachment.

2. Experimental setup

2.1. Vacuum equipment and discharge arrangement

Figure 1 shows the experimental setup. The investigations were performed in an asymmetric capacitively coupled rf discharge (cc-rf). The water-cooled planar rf electrode with a 10 cm diameter consists of stainless steel and was powered by the rf generator at 13.56 MHz (ENI ACG-3B) and a fully tuneable π-type matching network (ENI MW-10D). The shielding of the powered electrode and the chamber wall provide the grounded electrode. The stainless steel vacuum chamber with a diameter of 400 mm and a height of 400 mm was pumped by means of a 210 l s^{-1} turbopump to a base pressure of 5×10^{-5} Pa. The process pressure of between 10 and 100 Pa was obtained by means of a 16 m^{3}h^{-1} stage rotary pump in combination with a throttle valve to control the total pressure independently of the process gas flow. Pure oxygen (O_2) was used as the process gas which was admitted to the

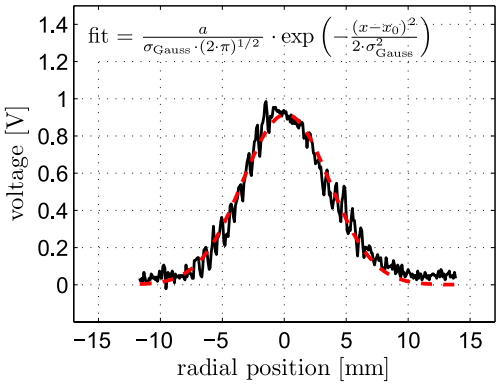

Figure 2. Comparison of the measured (solid line) and fitted (dashed line) radial power profile of the Gaussian beam. The Gaussian beam radius w corresponds to the $1/e$ power decay multiplied by $\sqrt{2}$ as expected.

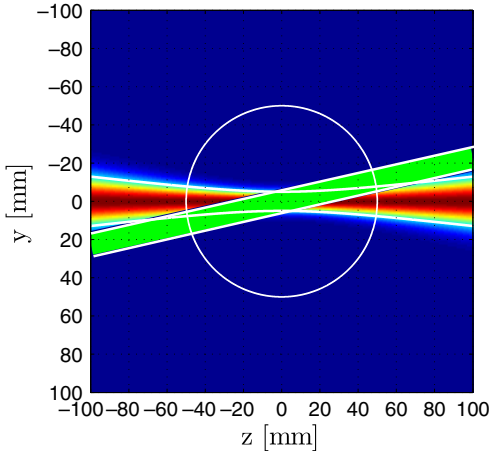

Figure 3. Scaled drawing of the overlapping zone between the microwave and laser beam above the powered rf electrode (white circle). The expanded laser beam is merged with the Gaussian microwave beam in the z-direction under an angle of 12.6°. The Gaussian beam radius is marked by the solid white line representing the $1/e$ electric field decay.

reactor via a mass flow controller (mks 647 C) with a constant gas flow rate of 5 sccm. The plasma processing parameters of pressure and rf power used in the investigations are carefully selected to avoid attachment-induced ionization instabilities.

2.2. Microwave interferometer

The microwave interferometer consists of a frequency stabilized PLL heterodyne system operating at a frequency of 160.28 GHz or the corresponding wavelength of $\lambda_{\mathrm{MWI}} = 1.87$ nm. Gaussian beam propagation theory was used to describe the microwave free space propagation.

In particular, the microwave for the measuring path was guided in D-band waveguides from the interferometer to the specially designed horn antennas. The horn antennas were calculated and manufactured for the specific frequency of 160.28 GHz to ensure an optimal transition to the free space as required by Gaussian beam theory.

The free space microwave beam was guided and refocused via specially designed elliptical mirrors with an optical axis of 20 mm above the powered electrode, see figures 1 and 3. The beam waist is 5 mm at the electrode centre which corresponds to a minimum axial resolution of about 10 mm. The elliptical mirrors were also calculated by the requirements of Gaussian beam theory. The optical axis is far away from the rf sheath edge. Hence, the microwave beam is focused on the rf bulk plasma. This can be seen in the axial distribution of the rf phase resolved relative excitation rate of atomic oxygen in figure 4 [34, 35]. The time averaged rf sheath thickness of approximately 7 mm corresponds to the axial distance at the maximum excitation rate in the sheath expansion phase (pattern I) after about 7 ns.

The free space microwave beam propagation was calculated theoretically using the aforementioned Gaussian beam propagation theory. To check the realized alignment, the disturbance of the microwave power was measured by inserting a thin dielectric rod perpendicular to the beam propagation. In figure 2 it is clearly shown that the measured radial power distribution of the microwave beam is in accordance with the calculated Gaussian beam radius which corresponds to the radial position of the $1/e$ power decay multiplied by $\sqrt{2}$.

The electron density is directly coupled with the electron plasma frequency and therefore with the refractive index of the plasma. This allows a direct measurement of the line-integrated electron density $\tilde{n}_{\mathrm{e}}$ against the background signal and leads to the phase shift $\Delta\Phi$ of the microwave without any model assumptions. For a non-magnetized plasma and an electron density which is radially homogeneous over the Gaussian beam the relation between the phase shift and the line-integrated electron density in the z-direction is given by

$$\Delta\Phi = \frac{\pi}{n_{\mathrm{C}}\,\lambda_{\mathrm{MWI}}} \underbrace{\int_{z_1}^{z_2} n_{\mathrm{e}}(z)\,\mathrm{d}z}_{\tilde{n}_{\mathrm{e}}}, \qquad (2)$$

where n_{C} is the critical electron density, λ_{MWI} is the wavelength of the microwave and $n_{\mathrm{e}}(z)$ is the absolute electron density at the axial position z of the Gaussian beam propagation.

2.3. Nd : YAG laser arrangement

The used Nd : YAG laser system operates at the second harmonic with a corresponding wavelength of 532 nm. The laser has a repetition rate of 10 Hz and a maximum pulse energy of 400 mJ at a pulse length of 7 ns. The laser beam was expanded to a diameter of 13 mm and guided quasi-parallel through the plasma, under an angle of 12.6° to the microwave optical axis, see figures 1 and 3. Therefore, the optical axis of the laser beam has the same axial distance of 20 mm to the powered electrode as the microwave beam. Consequently, this allows

(i) undisturbed microwave guiding within the aperture limit of the Gaussian beam propagation [36, 37], and
(ii) an optimal overlap between the laser and microwave beam

to ensure the best signal-to-noise ratio.

Plasma Sources Sci. Technol. **19** (2010) 065011 C Küllig *et al*

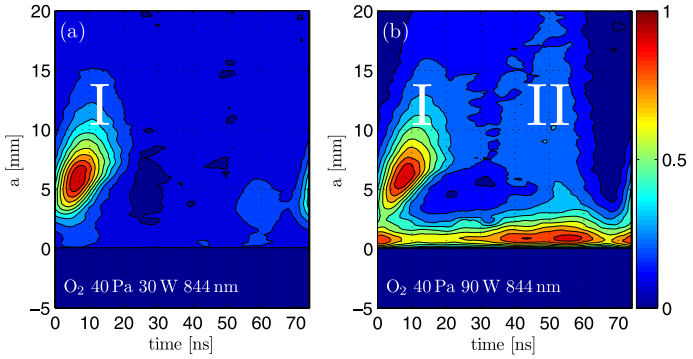

Figure 4. Spatial and rf phase resolved relative excitation rates of an oxygen rf plasma for the corresponding emission of atomic oxygen at 844 nm [34, 35] where the ordinate denotes the axial distance to the powered electrode. (*a*) Excitation due to electron heating during the sheath expansion phase (I), the α-mode of the rf discharge (40 Pa, 30 W). (*b*) An additional excitation pattern (II) due to secondary electrons in the γ-mode of the rf discharge (40 Pa, 90 W). Furthermore, the excitation of atomic oxygen due to heavy particle impact can be seen immediately in front of the powered electrode ($a = 0$ mm).

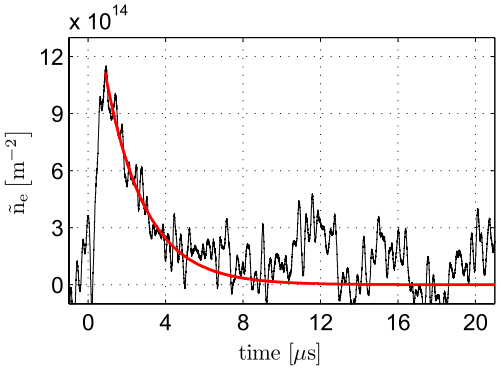

Figure 5. Example of the measured detachment signal in oxygen rf plasma at pressure of 10 Pa, rf power of 12 W, and self-bias voltage of −180 V.

2.4. Detachment signal and dependence on the laser pulse energy

The characteristic detachment signal over time is clearly shown in figure 5, taken simultaneously by microwave interferometry and laser photodetachment. The data acquisition with the microwave interferometer was performed in two steps,

1. the measurement of the background signal, and
2. the measurement of the signal during laser photodetachment.

Both signals were typically measured 5000 times, then averaged and subsequently subtracted. This averaged detachment signal provides the line-integrated density of the detached electrons with a sufficient signal-to-noise ratio and reduced influence of other external disturbances. The detachment peak in figure 5 corresponds to the detached electrons in addition to their steady state value and provides information about the negative oxygen ion density. The subsequent decrease in the detachment signal describes the electron density relaxation.

The decrease of the laser beam diameter by the use of an adjustable circular aperture results in a reduced detachment signal due to the alteration of the volume overlapping with the microwave beam. No change was observed in the electron relaxation time constant.

The ratio of the laser photodetached electrons to the total number density of negative ions depends on the laser power and can be deduced by [39, 40]

$$\Delta n_e + n_- = n_{-0} \tag{3}$$

and

$$\frac{d\Delta n_e}{dt} = \frac{\sigma I}{h\nu}(n_{-0} - \Delta n_e), \tag{4}$$

where I is the laser intensity and σ is the photodetachment cross section. In (3) it is clarified that the sum of densities from laser photodetached electrons Δn_e and the remaining negative oxygen ions n_- is constant and equal to the steady state negative ion density n_{-0}. For the short-pulsed laser system applied here, it is possible to evaluate (4). Using $\int I\,dt \equiv E/A$ where E is the laser energy and $A = \pi R^2_{\text{laser}}$ is the laser beam cross section, the solution of (4) is given by

$$\frac{\Delta n_e}{n_{-0}} = \left[1 - \exp\left(-\frac{\sigma}{h\nu}\frac{E}{A}\right)\right]. \tag{5}$$

Figure 6 shows the theoretical curve shape of the ratio between the photodetached electron density Δn_e and the steady state negative ion density n_{-0} using a laser diameter of 13 mm and a photodetachment cross section of $\sigma = 6.4 \times 10^{-22}\,\text{m}^2$ taken from Burch *et al* [38]. Additionally, this figure contains the measured values of this ratio taken from microwave interferometry and laser photodetachment. The measured values represent the theoretically evaluated detachment ratio very well. Furthermore, the variation of the laser energy from 230 mJ up to 340 mJ shows that the detachment signal does not change significantly. Hence, the increase in electron density is independent of the laser energy in this interval. Consequently, figure 6 reveals that an energy of 400 mJ is necessary to detach all of the negative ions within the overlapping volume of the

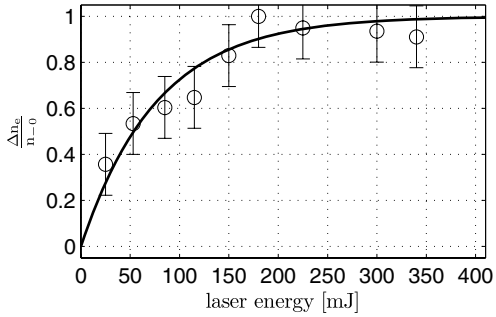

Figure 6. Ratio of detached electron and steady state negative ion density over the laser energy for a laser diameter of 13 mm and cross section of $\sigma = 6.4 \times 10^{-22}\,\mathrm{m}^2$ for photodetachment [38].

laser beam with a diameter of 13 mm and the microwave beam. The laser energy was fixed at 400 mJ for all further experiments. It can be shown that the measured detachment signals are reproducible and independent of the sampling electronics used or other disturbing influences.

3. Results and discussion

3.1. Negative atomic oxygen ion density and electron density relaxation

Figure 7 shows typical laser photodetachment signals from the microwave interferometer for different total pressures in oxygen plasma with a constant rf power of 40 W and a gas flow rate of 5 sccm.

As expected, the line-integrated electron density increases immediately after the laser pulse for all three pressure values. The detachment peak appears after approximately 1 μs. Therefore, this peak of the line-integrated electron density in figure 7 corresponds to the line-integrated negative oxygen ion density $\tilde{n}_-$, in particular $10^{15}\,\mathrm{m}^{-2}$ for 60 Pa, $7 \times 10^{14}\,\mathrm{m}^{-2}$ for 30 Pa, and $2 \times 10^{14}\,\mathrm{m}^{-2}$ for 10 Pa. The main error in the measured detachment signals is produced by the noise band of the signal itself and can be estimated by $\pm 2 \times 10^{14}\,\mathrm{m}^{-2}$.

The overlapping length of the microwave and laser beam amounts to approximately 15 cm. With this overlapping length, and the assumption that negative ions are completely removed due to laser photodetachment in the detection volume, the spatially averaged absolute number density of negative atomic oxygen ions amounts to $6.6 \times 10^{15}\,\mathrm{m}^{-3}$ for 60 Pa, $4.7 \times 10^{15}\,\mathrm{m}^{-3}$ for 30 Pa and $1.7 \times 10^{15}\,\mathrm{m}^{-3}$ for 10 Pa. It should be mentioned that both the time axis and the axis of the line-integrated electron density at 10 Pa in figure 7 differ from those of 30 and 60 Pa. This clearly indicates that the decay time constant of the detachment signal depends on the total pressure. The decay time constants were evaluated by the use of a single exponential fit function, which is shown as a solid bold line for each pressure in figure 7. Additionally, the fit functions are plotted separately in figure 8 with semi-logarithmic scaling. The corresponding time constant amounts to 1.6 μs for 60 Pa, 3.2 μs for 30 Pa, 37 μs for 20 Pa and 75 μs for 10 Pa. The significant change in the time constant

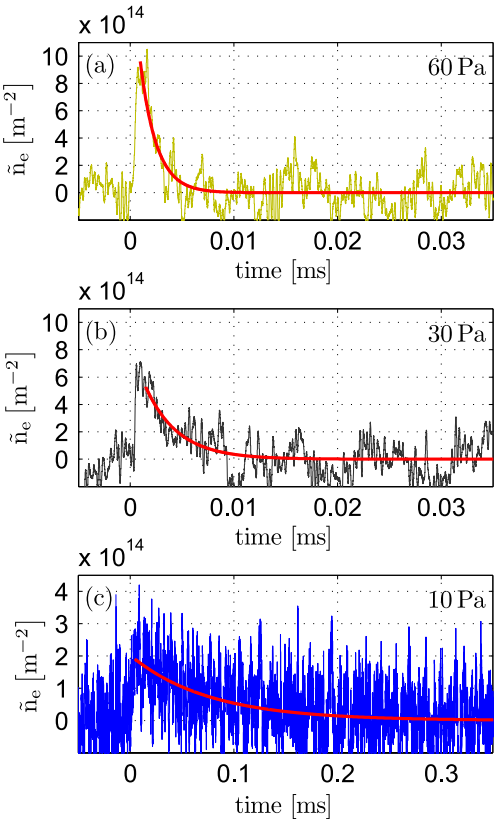

Figure 7. Increase in the electron density after the laser pulse and the subsequent relaxation at the rf power of 40 W for different oxygen pressures, 60, 30 and 10 Pa. The electron peak corresponds to the line-integrated negative oxygen ion density $\tilde{n}_-$. The bold lines represent the fitted exponential decay curves. In comparison with 30 and 60 Pa, the time axis as well as the axis for the line-integrated electron density is changed in the plotted signal for 10 Pa.

by one order of magnitude due to the pressure change from 20 to 30 Pa clearly reveals a transition between two different plasma modes which exist for lower and higher pressure at the constant rf power of 40 W. Within one of the observed plasma modes the time constant decreases with rising total pressure as expected. The observed phenomena may be connected to the ratio between steady state negative ion and electron density, α, which denotes the electronegativity of the plasma, and its influence on the relaxation kinetics of electrons and negative ions after the laser pulse. This can be seen by comparing the 10 and 60 Pa measurements at a rf power of 40 W, see figure 8. For 10 Pa the line-integrated steady state electron density amounts to $4 \times 10^{15}\,\mathrm{m}^{-2}$, which leads to a electronegativity of 0.05 and is linked with a decay time constant of 75 μs. In contrast, for 60 Pa and 40 W the line-integrated steady state electron density amounts to about $2 \times 10^{14}\,\mathrm{m}^{-2}$, providing a electronegativity of 5 with a decay time constant of 1.6 μs. This comparison shows that the oxygen plasma is operating in two different modes.

Most probably the capacitively coupled asymmetric rf discharge changes from the α-mode to the γ-mode [41]. A

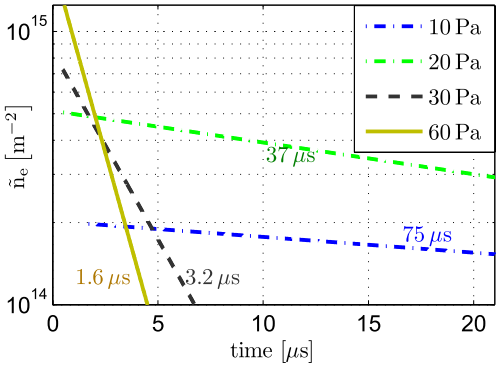

Figure 8. Semi-logarithmic plot of the exponential fit function with decay time constant for different oxygen pressures at rf power of 40 W.

similar transition was observed in previous measurements of the spatial and phase resolved optical emission of atomic oxygen at 844 nm [34, 35]. Here the transition from the α- to the γ-mode is characterized by the appearance of a second excitation pattern (II) due to secondary electrons, see figure 4. In this figure the microwave propagates radially at the axial position $a = 20$ mm. This means that these fast electrons, coming from the rf sheath, have a significant influence on plasma kinetics in the detection volume of the microwave beam, e.g. excitation, ionization, attachment and detachment.

3.2. The influence of rf power variation on the negative atomic oxygen ion and electron densities

Figure 9 compares the measured values for the line-integrated negative ion density, the decay time constant of the detachment signal, the line-integrated electron density and the resulting ratio between steady state negative ion and electron density, α, dependent on the rf power at a constant total pressure of 30 Pa.

All these measured values show a non-monoton behaviour characterized by step-like change between 50 and 60 W of rf power. The line-integrated negative ion density is reduced by a factor of about 3 at 60 W which is combined with an increasing decay time constant by one order of magnitude, see figures 9(*a*) and (*b*). A similar behaviour is observed in the steady state electron density. With increasing rf power the line-integrated electron density remains at a low level in the range of only a few 10^{14} m^{-2}, see figure 9(*c*). Then at rf powers greater than 50 W the electron density increases by one order of magnitude and amounts to about 10^{16} m^{-2} at 100 W. This dramatic change in the oxygen rf plasma is also reflected in the ratio between negative ion and electron density. The value α switches from high ($\alpha > 2$) to low ($\alpha < 1$) electronegativity with increasing rf power between 50 and 60 W, see figure 9(*d*).

This significant change in the electronegativity can be correlated with the transition of the plasma from the α-mode to the γ-mode of the discharge as already mentioned in section 3.1 and represented in figure 4. Generally, the γ-mode is characterized by a lower 'electron temperature' at a much higher electron density, comparable to the conditions in the negative glow of a dc discharge.

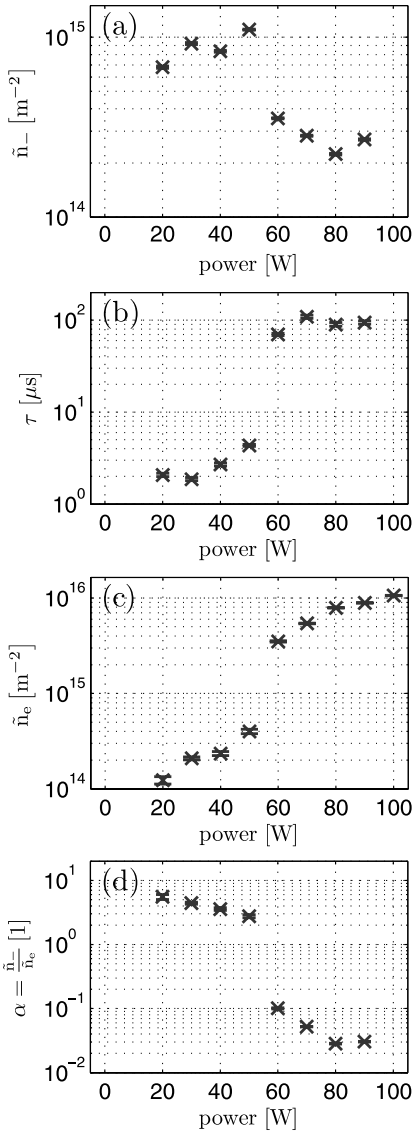

Figure 9. Influence of the rf power on the detachment signal at oxygen pressure of 30 Pa. A comparison between the line integrated steady state negative ion density (*a*), the decay time constant of the detachment signal (*b*), the line-integrated steady state electron density (*c*) and the electronegativity α (*d*).

3.3. Modelling of the detachment signal for low decay time constants at high electronegativity

In this section, a simple 0D-attachment–detachment model is applied to describe the electron density relaxation after the laser pulse at high electronegativity with a corresponding low decay time constant of the detachment signal. It is assumed that the density of all other species does not change significantly during the detachment and electron density relaxation phase, in particular the positive ion density (O_2^+) as well as the neutral heavy species $O_2(X\,^3\Sigma_g^-)$, $O_2(a\,^1\Delta_g)$ and $O(^3P)$.

Table 1. Experimental results for low rf power at 30 Pa.

P [W]	$\tilde{n}_e$ [10^{14} m^{-2}]	$\tilde{n}_-$ [10^{14} m^{-2}]	α [1]	τ [10^{-6} s]	$\tilde{K}_a$ [10^5 s^{-1}]	$\tilde{K}_d$ [10^4 s^{-1}]
20	1.2 ± 0.3	6.8 ± 0.1	5.5 ± 0.5	2.0 ± 1	4.2 ± 0.5	7.5 ± 0.5
30	2.1 ± 0.1	9.2 ± 0.2	4.4 ± 0.2	1.9 ± 1	4.5 ± 0.4	10.1 ± 0.5
40	2.3 ± 0.1	8.4 ± 0.1	3.6 ± 0.1	2.7 ± 1	3.0 ± 0.3	8.3 ± 0.4
50	4.0 ± 0.1	11.0 ± 0.1	2.8 ± 0.2	4.3 ± 1	1.7 ± 0.3	6.2 ± 0.3

During the laser detachment and the short electron relaxation time in the used operation mode at high electronegativity of the rf discharge, the positive ion density should not be significantly influenced by the electron impact ionization and the recombination reactions of positive ions. In particular, the characteristic reaction time constant for the recombination of the molecular positive ions O_2^+ with electrons and negative atomic oxygen ions, calculated by means of the rate coefficients k_{re} and k_{r-} [42] and the corresponding positive ion density, amount to about $1/(k_{re} \cdot n_{+0}) \sim 5$ ms and $1/(k_{r-} \cdot n_{+0}) \sim 10$ ms, respectively. The loss of negative atomic oxygen ions in the detachment reactions with ground state and metastable excited molecular oxygen is much faster, characterized by reaction time constants in the order of $1/(k_{dX} \cdot n_X) \sim 0.1$ ms and $1/(k_{d\Delta} \cdot n_\Delta) \sim 0.01$ ms, respectively.

The dissociative electron attachment to ground state and metastable molecular oxygen (6), (7) and the collisional detachment of negative atomic oxygen ions with ground state and metastable molecular oxygen (8), (9) as well as ground state atomic oxygen (10) are considered and discussed:

$$e + O_2(X\,^3\Sigma_g^-) \xrightarrow{k_{aX}} O^- + O(^3P), \tag{6}$$

$$e + O_2(a\,^1\Delta_g) \xrightarrow{k_{a\Delta}} O^- + O(^3P), \tag{7}$$

$$O^- + O_2(X\,^3\Sigma_g^-) \xrightarrow{k_{dX}} O_2(X\,^3\Sigma_g^-) + O(^3P) + e, \tag{8}$$

$$O^- + O_2(a\,^1\Delta_g) \xrightarrow{k_{d\Delta}} O_3(\text{or products}) + e, \tag{9}$$

$$O^- + O(^3P) \xrightarrow{k_{dO}} O_2(X\,^3\Sigma_g^-) + e. \tag{10}$$

This results in electron balance equation

$$\frac{dn_e}{dt} = -(k_{aX}(T_e)n_X + k_{a\Delta}(T_e)n_\Delta)n_e + (k_{dX}n_X + k_{d\Delta}n_\Delta + k_{dO}n_O)n_-. \tag{11}$$

To make this equation more clear the effective rate coefficients $\tilde{K}_a$ and $\tilde{K}_d$ are introduced:

$$\tilde{K}_a = k_{aX}(T_e)n_X + k_{a\Delta}(T_e)n_\Delta, \tag{12}$$

$$\tilde{K}_d = k_{dX}n_X + k_{d\Delta}n_\Delta + k_{dO}n_O, \tag{13}$$

which simplify the electron balance equation (11) to

$$\frac{dn_e}{dt} = -\tilde{K}_a n_e + \tilde{K}_d n_-, \tag{14}$$

$$n_e + n_- = n_{+0} \equiv \text{const}. \tag{15}$$

By the use of these effective rate coefficients $\tilde{K}_a$ and $\tilde{K}_d$ and the condition for quasi-neutrality (15) at a constant positive ion density, the differential equation (16) describes first order kinetics and can be solved analytically together with the steady state solution (17) and initial condition (18):

$$\frac{dn_e}{dt} = -(\tilde{K}_a + \tilde{K}_d)n_e + \tilde{K}_d n_{+0}, \tag{16}$$

$$\tilde{K}_a \cdot n_{e0} = \tilde{K}_d \cdot n_{-0}, \tag{17}$$

$$n_e(t=0) = n_{e0} + n_{-0} = n_{+0}. \tag{18}$$

As a result equation (19) for the electron density Δn_e, in addition to the steady state value n_{e0}, describes the decay of the detachment signal by a simple exponential function:

$$\Delta n_e(t) = (n_e(t) - n_{e0}) = n_{-0} \cdot \exp[-(\tilde{K}_a + \tilde{K}_d) \cdot t]. \tag{19}$$

From the measured decay time constant τ, as well as the electron (n_{e0}) and negative ion (n_{-0}) density in steady state, the effective rate coefficient for dissociative electron attachment ($\tilde{K}_a$) and collisional detachment ($\tilde{K}_d$) can be calculated from

$$\frac{\tilde{K}_a}{\tilde{K}_d} = \frac{n_{-0}}{n_{e0}} = \alpha = \frac{\tilde{n}_-}{\tilde{n}_e}, \tag{20}$$

$$\tilde{K}_a + \tilde{K}_d = \frac{1}{\tau} \tag{21}$$

and finally

$$\tilde{K}_a = \frac{1}{\tau} \cdot \frac{1}{1 + (1/\alpha)} \tag{22}$$

$$\tilde{K}_d = \frac{1}{\tau} \cdot \frac{1}{1 + \alpha}. \tag{23}$$

The results are also shown in table 1.

To discuss the experimentally determined effective rate coefficients $\tilde{K}_a$ and $\tilde{K}_d$, the relevant attachment and detachment rate coefficients from the literature are used, see table 2. It should be noted that in many publications the rate coefficients for electron attachment and negative ion detachment in oxygen discharges have their origin in only a few publications. In particular, a main source is the report on basic data for modelling by Eliasson *et al* [42]. Some new experimental work was done by Belostotsky *et al* [21] and Midey *et al* [43, 44]. They have studied the destruction of negative oxygen ions by $O(^3P)$ and $O_2(a\,^1\Delta_g)$ in the positive column of dc glow discharge, and in reactions with $O_2(a\,^1\Delta_g)$ by means of an ion flow tube setup. For the evaluation of our simple model we consider firstly the contribution of the different collision partners in the detachment reactions. The absolute atomic oxygen density in a similar oxygen rf plasma was determined by two photon laser-induced fluorescence spectroscopy (TALIF), and its maximum density was in the range of only 10^{19} m^{-3} [45–47]. Therefore, the detachment

Table 2. Attachment and detachment rate coefficients.

Reaction	Rate coefficient $\left[\frac{\mathrm{m}^3}{\mathrm{s}}\right]$	Remarks	Reference
(6)	k_{aX}		
	$8.8 \times 10^{-17} \exp\left(\frac{-4.4}{T_\mathrm{e}}\right)$		[42]
(7)	$k_{\mathrm{a}\Delta}$		
	$2.28 \times 10^{-16} \exp\left(\frac{-2.29}{T_\mathrm{e}}\right)$		[50]
(8)	k_{dX}	E/N [Td]	
	2.7×10^{-20}	91	[42]
	2.4×10^{-18}	121	[42]
	2.5×10^{-17}	200	[42]
(9)	$k_{\mathrm{d}\Delta}$		
	3.0×10^{-16}		[42]
	1.9×10^{-16}		[21]
	3.0×10^{-16}		[51]
	1.1×10^{-16}	$T_\mathrm{g} = 300\,\mathrm{K}$	[43]
	8.6×10^{-17}	$T_\mathrm{g} = 300\,\mathrm{K}$	[44]
(10)	k_{dO}		
	1.4×10^{-16}		[42]
	2.3×10^{-16}		[21]
	2.0×10^{-16}		[51]

by neutral atomic oxygen in the low pressure rf plasma was no longer considered. Furthermore, the detachment of atomic negative oxygen ions in reaction with ground state molecular oxygen depends strongly on the reduced electric field strength. The corresponding rate coefficient varies over three orders of magnitude by changing the reduced electric field strength from about 90 to 200 Td [42]. In the used discharge operation the rate coefficient for this reaction should have a value no higher than $10^{-18}\,\mathrm{m}^3\,\mathrm{s}^{-1}$ and this detachment reaction was also excluded in spite of the higher molecular ground state density. Therefore, we assume that the detachment of negative atomic oxygen ions in reaction with metastable singlet $O_2(a\,^1\Delta_g)$ is the main loss channel in our simple attachment–detachment model. Taking into account the detachment reaction (9) with the adequate rate coefficient $k_{\mathrm{d}\Delta} = 10^{-16}\,\mathrm{m}^3\,\mathrm{s}^{-1}$ from Mideay *et al* [43, 44] and the effective detachment rate coefficient $\tilde{K}_\mathrm{d}$ from the experimental data, the metastable molecular oxygen density n_Δ can be calculated for each rf power according to the remaining term of (13) $\tilde{K}_\mathrm{d} = k_{\mathrm{d}\Delta} n_\Delta$, see figure 10. The ground state molecular oxygen density can be estimated from the difference between the total particle density at 30 Pa total pressure and a temperature of 300 K, and the metastable density, see figure 10. As a result, the relative density of the metastable singlet $O_2(a\,^1\Delta_g)$ is in the order of 10%, which is in the right order of magnitude in comparison with the values in the literature [21, 48, 49].

The electron attachment reactions (6) and (7) are now considered. Equation (12) is evaluated by considering the dissociative attachment rate coefficients from the literature, which are provided as dependent on the electron temperature for ground state molecular oxygen [42] and metastable singlet molecular oxygen [50] (table 2, figure 11(*b*)), as well as the corresponding oxygen densities estimated above, see figure 10. Figure 11(*a*) shows the determined dissociative electron attachment rate coefficients k_{aX} and $k_{\mathrm{a}\Delta}$ as dependent

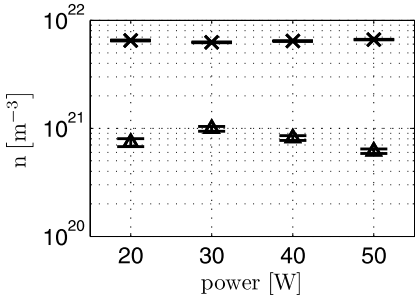

Figure 10. The experimentally determined density of ground state $O_2(X\,^3\Sigma_g^-)$ (×) and metastable molecular oxygen $O_2(a\,^1\Delta_g)$ (△) from the detachment reaction with metastable molecular oxygen and total particle density at 30 Pa and 300 K.

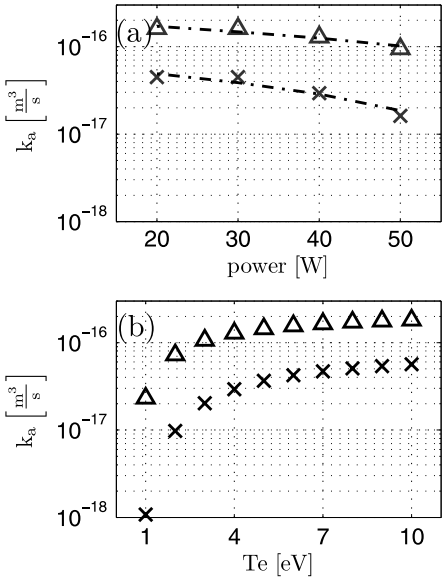

Figure 11. (*a*) The attachment rate coefficient for ground state (×) and metastable molecular oxygen (△) over the rf power, evaluated from the experimentally determined effective rate coefficient. (*b*) The literature values of the dissociative attachment rate coefficient for ground state k_{aX} (×) and metastable molecular oxygen $k_{\mathrm{a}\Delta}$ (△) over the electron temperature, see table 2.

on the rf power according to their variation with the electron temperature provided in figure 11(*b*). The attachment rate coefficient decreases slightly with increasing rf power due to the decrease in electron temperature from 6 to 2 eV. The estimated values for the attachment rate coefficients are in the appropriate order of magnitude, and show that the dissociative attachment in reactions with metastable singlet molecular oxygen is necessary to explain the effective attachment rate coefficient $\tilde{K}_\mathrm{a}$.

The model of the detachment signal in the case of weak electronegativity at higher rf powers, characterized by relatively large decay time constants for electron density relaxation, is considered to represent plasma kinetics created by multiple plasma species, e.g. γ-electrons, molecular

positive ions, atomic and molecular negative oxygen ions, neutral atomic oxygen, and metastables, as well as the transport processes in/out the detachment volume.

4. Conclusions

For the first time, the negative ion density in low pressure capacitively coupled rf oxygen plasma was measured simultaneously by means of laser photodetachment and 160 GHz microwave interferometry. The additional electrons produced after the detachment laser pulse were measured as a phase shift in the microwave interferometer. This phase shift can be converted directly into the line-integrated electron density. Hence, the peak of the line-integrated electron density corresponds to the line-integrated negative oxygen ion density which is in the range of 2.5×10^{14} and 10^{15} m^{-2}. Additionally, parameter studies have shown that the oxygen rf plasma can be divided into two plasma modes with regard to its electronegativity. For example, at a constant total pressure of 30 Pa the plasma switches from high electronegativity ($\alpha > 2$) to low electronegativity ($\alpha < 0.2$) at rf powers greater than 50 W. This also correlates with different electron density relaxations as expressed by a strong change in the decay time constant of the detachment signal from a few microseconds to about a hundred microseconds. This step-like behaviour may correlate with the transition from the α-mode to the γ-mode of the capacitively coupled rf plasma. Furthermore, a simple 0D-attachment–detachment model was applied to the discharge mode at high electronegativity to calculate the effective rate coefficient for dissociative electron attachment ($\tilde{K}_a$) and collisional detachment ($\tilde{K}_d$) from the experimentally determined values of steady state electron and negative ion density, as well as the decay time constant of the detachment signal. The evaluation of the attachment and detachment reactions by the use of the effective rate coefficients, as well as rate coefficients from the literature, has provided information about the main reaction channels in the investigated low pressure capacitively coupled rf plasma. The metastable molecular singlet state $O_2(a\,^1\Delta_g)$ has to be implemented for interpretation of both the effective attachment and detachment rate coefficients as determined from the experimental data.

This paper has demonstrated the possibility of detecting laser photodetached electrons by means of 160 GHz microwave interferometry using Gaussian beam propagation. Additional investigations will be performed in a wider range of parameters, including attachment-induced ionization instabilities. Langmuir probe measurements will be carried out to characterize the spatial plasma density distribution, in particular in the region of the microwave beam.

Acknowledgments

This work was supported by the Deutsche Forschungsgemeinschaft (DFG) in the framework of the Sonderforschungsbereich Transregio 24 'Fundamentals of Complex Plasmas'.

The authors wish to thank Dr M Hirsch and Professor Dr H-J Hartfuss from IPP, Greifswald branch, for helpful discussion and advice on microwave diagnostics. Moreover, we thank the IPF Stuttgart for the construction of the special feed-horns.

References

[1] Descoeudres A, Sansonnens L and Hollenstein Ch 2003 Attachment-induced ionization instability in electronegative capacitive RF discharges *Plasma Sources Sci. Technol.* **12** 152–7

[2] Katsch H-M, Goehlich A, Kawetzki T, Quandt E and Döbele H-F 1999 Attachment-induced ionization instability of a radio frequency excited discharge in oxygen *Appl. Phys. Lett.* **75** 2023–5

[3] Nighan W L and Wiegand W J 1974 Influence of negative-ion processes on steady-state properties and striations in molecular gas discharges *Phys. Rev.* A **10** 922–45

[4] Lieberman M A, Lichtenberg A J and Marakhtanov A M 1999 Instabilities in low-pressure inductive discharges with attaching gases *Appl. Phys. Lett.* **75** 3617–9

[5] Chabert P, Lichtenberg A J, Lieberman M A and Marakhtanov A M 2001 Instabilities in low-pressure electronegative inductive discharges *Plasma Sources Sci. Technol.* **10** 478–89

[6] Corr C S, Steen P G and Graham W G 2003 Instabilities in an inductively coupled oxygen plasma *Plasma Sources Sci. Technol.* **12** 265–72

[7] Katsch H M, Manthey C and Döbele H F 2003 Charge carrier dynamics in a pulsed inductive RF discharge in oxygen *Plasma Sources Sci. Technol.* **12** 475–83

[8] Hollenstein Ch, Schwarzenbach W, Howling A A, Courteille C, Dorier J L and Sansonnens L 1996 Anionic clusters in dusty hydrocarbon and silane plasmas *J. Vac. Sci. Technol.* A **14** 535

[9] Boyd F R L and Thompson J B 1959 The operation of Langmuir probes in electronegative plasmas *Proc. R. Soc.* A **252** 102

[10] Braithwaite N St J and Allen J E 1988 Boundaries and probes in electronegative plasmas *J. Phys. D: Appl. Phys.* **21** 1733–7

[11] Zeuner M, Meichsner J and Rees J A 1996 High energy negative ions in a radio-frequency discharge *J. Appl. Phys.* **79** 9379

[12] Dittmann K, Matyash K, Nemschokmichal S, Meichsner J and Schneider R 2010 Excitation mechanisms and sheath dynamics in capacitively coupled radio-frequency oxygen plasmas *Contrib. Plasma Phys.* **50** in press

[13] Mosbach T, Katsch H-M and Döbele H F 1998 Temporal behaviour of the H-minus density in a pulsed multipole discharge investigated by the photodetachment technique *Plasma Sources Sci. Technol.* **7** 75–81

[14] Bacal M 2000 Photodetachment diagnostic techniques for measuring negative ion densities and temperatures in plasmas *Rev. Sci. Instrum.* **71** 3981–4006

[15] Arndt S, Sigeneger F, Testrich H and Brandt C 2005 Self-consistent analysis of the spatial relaxation of a disturbed neon glow discharge *Plasma Chem. Plasma Process.* **25** 567–94

[16] Brandt C, Testrich H, Kozakov R and Wilke C 2006 Investigation of the disturbance of a Langmuir probe and its influence on measurement results *Rev. Sci. Instrum.* **77** 023504

[17] Demidov V I, Ratynskaia S V and Rypdal K 2002 Electric probes for plasmas: the link between theory and instrument *Rev. Sci. Instrum.* **73** 3409–39

[18] Godyak V A, Piejak R B and Alexandrovich B M 1992 Measurements of electron energy distribution in low-pressure RF discharges *Plasma Sources Sci. Technol.* **1** 36–58

[19] Godyak V A, Piejak R B and Alexandrovich B M 1993 Probe diagnostics of non-Maxwellian plasmas *J. Appl. Phys.* **73** 3657–63

[20] Katsch H M, Sturm T, Quandt E and Döbele H F 2000 Negative Ions and the role of metastable molecules in a capacitively coupled radiofrequency excited discharge in oxygen *Plasma Sources Sci. Technol.* **9** 323–30

[21] Belostotsky S G, Economou D J, Lopaev D V and Rakhimova T V 2005 Negative ion destruction by $O(^3P)$ atoms and $O_2(a\,^1\Delta_g)$ molecules in an oxygen plasma *Plasma Sources Sci. Technol.* **14** 532–42

[22] Niemöller N, Schulz-von der Gathen V, Stampa A and Döbele H F 1997 A quasi-optical 1 mm microwave heterodyne interferometer for plasma diagnostics using a frequency-tripled Gunn oscillator *Plasma Sources Sci. Technol.* **6** 478–83

[23] Lukas Ch, Müller M, Schulz-von der Gathen V and Döbele H F 1999 Spatially resolved electron density distribution in an RF excited parallel plate plasma reactor by 1 mm microwave interferometry *Plasma Sources Sci. Technol.* **8** 94–9

[24] Krämer M, Clarenbach B and Kaiser W 2006 A 1 mm interferometer for time and space resolved electron density measurements on pulsed plasmas *Plasma Sources Sci. Technol.* **15** 332–7

[25] Cappelli M A, Gascon N and Hargus W A Jr 2006 Millimetre wave plasma interferometry in the near field of a Hall plasma accelerator *J. Phys. D: Appl. Phys.* **39** 4582–8

[26] Lee J and Cappelli M A 2008 An analysis of millimetre-wave interferometry on Hall thruster plumes by finite difference time domain simulations *J. Phys. D: Appl. Phys.* **41** 185205

[27] Haverlag M, Kono A, Passchier D, Kroesen G M W, Goedheer W J and de Hoog F J 1991 Measurements of negative ion densities in 13.56 MHz rf plasmas of CF_4, C_2F_6, CHF_3, and C_3F_8 using microwave resonance and the photodetachment effect *J. Appl. Phys.* **70** 3472–80

[28] Rauf S, Ventzek P L G, Abraham I C, Hebner G A and Woodworth J R 2002 Charged species dynamics in an inductively coupled Ar/SF_6 plasma discharge *J. Appl. Phys.* **92** 6998–7007

[29] Hebner G A and Abraham I C 2001 Characterization of electron and negative ion densities in fluorocarbon containing inductively driven plasmas *J. Appl. Phys.* **90** 4929–37

[30] Shibata M, Nakano N and Makabe T 1997 The effect of laser-induced photodetachment in O_2 rf discharges *J. Phys. D: Appl. Phys.* **30** 1219–24

[31] Vender D, Stoffels W W, Stoffels E, Kroesen G M W and de Hoog F J 1995 Charged-species profiles in electronegative radio-frequency plasmas *Phys. Rev.* E **51** 2436–44

[32] Stoffels E, Stoffels W W, Vender D, Kando M, Kroesen G M W and de Hoog F J 1995 Negative ions in a radio-frequency oxygen plasma *Phys. Rev.* E **51** 2425–35

[33] Suzuki T and Kasuya T 1987 Optogalvanic study of photodetachment of O^- near threshold *Phys. Rev.* A **36** 2129–33

[34] Dittmann K, Drozdov D, Krames B and Meichsner J 2007 Radio-frequency discharges in oxygen: II. Spatio-temporally resolved optical emission pattern *J. Phys. D: Appl. Phys.* **40** 6593–600

[35] Dittmann K 2009 Detailed investigations of the sheath dynamics and elementary processes in capacitively coupled rf plasmas *PhD Thesis* Institute of Physics, Ernst-Moritz-Arndt University of Greifswald

[36] Goldsmith P F 1998 *Quasioptical Systems* (New York: IEEE Press)

[37] Véron D 1979 Submillimeter interferometry of high-density plasmas *Infrared and Millimeter Waves* vol 2, ed K J Button (New York: Academic) chapter 2

[38] Burch D S, Smith S J and Branscomb L M 1958 Photodetachment of O_2^- *Phys. Rev.* **112** 171–5

[39] Schiffer C and Uhlenbusch J 1995 Negative–oxygen–ion detection by a crossed-beam photodetachment technique *Plasma Sources Sci. Technol.* **4** 345–52

[40] Greenberg K E, Hebner G A and Verdeyen J T 1984 Negative ion densities in NF_3 discharges *Appl. Phys. Lett.* **44** 299–300

[41] Klagge S 1992 Space- and direction-resolved Langmuir probe diagnostic in RF planar discharges *Plasma Chem. Plasma Process.* **12** 103–28

[42] Eliasson B and Kogelschatz U 1986 Basic data for modelling of electrical discharges in gases: oxygen *Technical report* Brown Boveri Forschungszentrum CH-5405 Baden

[43] Midey A, Dotan I, Lee S, Rawlins W T, Johnson M A and Viggiano A A 2007 Kinetics for the reactions of O^- and O_2^- with $O_2(a\,^1\Delta_g)$ measured in a selected ion flow tube at 300 K *J. Phys. Chem.* A **111** 5218–22

[44] Midey A, Dotan I and Viggiano A A 2008 Temperature dependences for the reactions of O^- and O_2^- with $O_2(a\,^1\Delta_g)$ from 200 to 700 K *J. Phys. Chem.* A **112** 3040–45

[45] Geigl M, Peters S, Gabriel O, Krames B and Meichsner J 2005 Analysis and kinetics of transient species in electrode near plasma and plasma boundary sheath of rf plasmas in molecular gases *Contrib. Plasma Phys.* **45** 369–77

[46] Goehlich A, Kawetzki T and Döbele H F 1998 On absolute calibration with xenon of laser diagnostic methods based on two-photon absorption *J. Chem. Phys.* **108** 9362–70

[47] Katsch H M, Tewes A, Quandt E, Goehlich A, Kawetzki T and Döbele H F 2000 Detection of atomic oxygen: improvement of actinometry and comparison with laser spectroscopy *J. Appl. Phys.* **88** 6232–8

[48] Shibata M, Nakano N and Makabe T 1996 Effect of $O_2(a\,^1\Delta_g)$ on plasma structures in oxygen radio frequency discharges *J. Appl. Phys.* **80** 6142–7

[49] Gudmundsson J T 2004 Recombination and detachment in oxygen discharges: the role of metastable oxygen molecules *J. Phys. D: Appl. Phys.* **37** 2073–81

[50] Gudmundsson J T, Marakhtanov A M, Patel K K, Gopinath V P and Lieberman M A 2000 On the plasma parameters of a planar inductive oxygen discharge *J. Phys. D: Appl. Phys.* **33** 1323–31

[51] Fehsenfeld F C, Albritton D L, Burt J A and Schiff H I 1969 Associative-detachment reactions of O^- and O_2^- by $O(^1\Delta_g)$ *Can. J. Chem.* **47** 1793–5

Article IV

PHYSICS OF PLASMAS **19**, 073517 (2012)

Detachment-induced electron production in the early afterglow of pulsed cc-rf oxygen plasmas

C. Küllig,[a] K. Dittmann,[b] and J. Meichsner[c]
University of Greifswald, Institute of Physics, Felix-Hausdorff-Str. 6, 17489 Greifswald, Germany

(Received 10 May 2012; accepted 28 June 2012; published online 23 July 2012)

Line integrated electron densities are measured by 160.28 GHz Gaussian beam microwave interferometry in a 10 Hz pulsed (50% duty cycle) cc-rf oxygen discharge, operating at 13.56 MHz. Depending on the processing parameters, the oxygen rf discharge displays two different operation modes regarding its electronegativity. For higher rf power with negative self-bias voltage above −220 V, the oxygen discharge acts as electropositive plasma ($n_-/n_e \ll 1$), whereas at lower rf power and self-bias voltage the plasma becomes strongly electronegative ($n_-/n_e > 2$). In the latter mode, a significant electron density increase is measured in the early afterglow (<100 μs) within a pressure range from 20 to 100 Pa. By use of a simple rate equation model, the temporal behavior of the electron density could be reproduced for both modes of electronegativity. The electron production in the early afterglow is mainly caused due to the detachment of negative atomic oxygen ions by metastable oxygen molecules. © *2012 American Institute of Physics*. [http://dx.doi.org/10.1063/1.4737196]

I. INTRODUCTION

Capacitively coupled rf plasmas are widely applied in plasma technologies, e.g., the plasma treatment of material surfaces for chemical modification, cleaning, etching, patterning, or for thin film deposition. Thus, pulsed plasmas are of interest with regard to the controlling of the mean electric power input and the influence on plasma chemical reactions in molecular plasmas. Furthermore, the thermal loading in surface treatment of sensitive materials can be reduced. Nevertheless, the oxygen plasma is interesting as model system for a complex multi-species plasma consisting of different charged species such as positive and negative ions, electrons as well as different neutral species like metastable oxygen molecules and reactive atomic oxygen, which can strongly affect the charged particle species balance.

The standard method for electron density determination is the use of a Langmuir probe, despite several disadvantages. For instance, being an invasive diagnostics, it can affect the plasma properties drastically.[1–3] Furthermore, complex model assumptions are necessary to interpret the probe characteristics and to determine the plasma parameter of interest, e.g., the electron energy distribution function (EEDF) or the electron density.[4,5] The formation of high resistance layers on the probe surface in reactive plasmas strongly influences the probe characteristics.[6–10] Moreover, the necessary electronics for compensation and filtering of the rf signal in the probe circuit limits the temporal resolution, especially for the measurement of fast electron density alteration in photodetachment experiments.

Therefore, the microwave interferometry has been used to determine electron densities. In comparison to the standard probe diagnostics, the microwave interferometry is a minimal-invasive method which directly allows the measurement of the line integrated electron density ($\bar{n}_e$) by the phase shift of the microwave due to the change of electron density. Further, no model assumption is required. The electron density is directly coupled with the plasma frequency and therefore with the refractive index of the plasma. Moreover, reactive plasmas have no influence on the microwave diagnostics.

In plasmas with negative ions, the electron kinetics is strongly influenced by attachment and detachment processes. In dependence on the ratio between negative ion and electron density, the cc-rf discharge may be operated in different modes. The negative oxygen ions were measured by laser photodetachment and simultaneous microwave interferometry. In this paper, we present results concerning the temporal behavior of the electron and negative ion density in the afterglow of a pulsed capacitively coupled radio frequency plasma in oxygen.

Many investigations about the afterglow behavior of low pressure plasmas can be found in the literature. In electronegative gases, an ion-ion-plasma was observed in the afterglow plasma due to different electron attachment processes.[11–13] Furthermore, electron density peaks were measured in the early afterglow in an inductively coupled oxygen plasma[14] as well as in helium[15,16] and hydrogen[17] plasmas. In this paper, we discuss electron density peaks measured in the early afterglow of a capacitively coupled oxygen rf plasma, which, to the knowledge of the authors, is not reported in the literature.

II. EXPERIMENTAL SETUP

The asymmetric capacitively coupled rf discharge (cc-rf) is operating at a frequency of 13.56 MHz. The cylindrical stainless steel vacuum chamber has a diameter and a height of 400 mm, respectively.

The chamber is pumped by a 200 l/s turbo pump to a base pressure of 5×10^{-5} Pa. The process pressure is varied from 5 to 100 Pa and is maintained by a 16 m^3/h stage rotary

[a]Electronic mail: kuellig@physik.uni-greifswald.de.
[b]Electronic mail: dittmann@physik.uni-greifswald.de.
[c]Electronic mail: meichsner@physik.uni-greifswald.de.

TABLE I. This table presents and explains the acronyms of this paper.

Acronym	Description
$\tilde{n}_{\langle index\rangle}$, $n_{\langle index\rangle}$	Line integrated density, absolute density
$\langle index\rangle = O_2^+, O^-, O_2^-, -, e, O, X, \Delta$	Positive molecular ion, negative atomic ion, negative molecular ion, negative ion, electron, atomic oxygen, molecular ground state ($O_2(X^3\Sigma_g^-)$), molecular metastable state ($O_2(a^1\Delta_g)$) oxygen
$n_-(0)$, $n_e(0)$	Afterglow initial negative ion and electron density
$\tilde{n}_{e,P}$, $n_{e,P}$	Line integrated, absolute electron afterglow peak density
$k_{\langle a,d,r,c\rangle}$	Rate coefficients for *a*ttachment, *d*etachment, *r*ecombination and *c*harge transfer, respectively, see Eqs. (7) to (15) and Table II
T_e	Electron temperature
τ_D, τ	Time constant for ambipolar diffusion and electron detachment from negative ions in the early afterglow, respectively
L_D	Diffusion length
D_a	Ambipolar diffusion coefficient

pump. Oxygen (O_2) is used as process gas which is filled into the reactor via a mass flow controller (mks 647 C) with a constant gas flow rate of 5 sccm.

The discharge configuration consists of a stainless steel electrode of 10 cm in diameter. This electrode is water cooled and powered by a rf generator at 13.56 MHz (ENI ACG-3B). A fully tunable π-type matching network (ENI MW-10D) ensures an ideal power coupling into the discharge. The shielding of the powered electrode and the chamber wall acts as grounded electrode. Due to the capacitive coupling and the large area ratio between the effective grounded and powered electrode, an asymmetric rf plasma is generated. It is characterized by a negative self-bias voltage at the powered electrode. The used forward rf power is between 5 and 150 W with corresponding self-bias voltages between -100 and -500 V. The rf discharge is pulsed at a frequency of 10 Hz with a duty cycle of 50% using a pulse delay generator (SR DG535).

Four windows of 140 mm in diameter each are mounted in the vacuum chamber angled 5 degree in the horizontal axis to avoid the disturbance of the microwave beam. The windows are made of fused silica (Suprasil II) to provide a small absorption coefficient in the microwave spectral range.

The investigated oxygen plasma is characterized by electron densities in the range from 10^{15} to $10^{16}\,m^{-3}$. The resulting small phase shifts of the interferometer signal are expected to be merely between 0.03° and 0.3°, which is the big challenge of the diagnostics. Therefore, the construction of mechanically stable optical units of the microwave interferometer is required. Hence, the complete experimental setup, i.e., the interferometer components together with the plasma reactor are mounted on an optical table using massive holders for the wave guiding components, i.e., the horn antennas and elliptic mirrors. Furthermore, a very stable frequency of the interferometer signal is necessary to minimize frequency fluctuations and to improve the signal-to-noise ratio in the phase shift measurement. Therefore, the microwave interferometer itself is a frequency stabilized (PLL) heterodyne system operating at a frequency of 160.28 GHz with a corresponding wavelength of 1.87 mm. The output power of the interferometer amounts to 1.3 mW.[18]

The Gaussian beam propagation theory was used to calculate the microwave free space propagation and to design the optical components (horn antennas, elliptical mirrors). They are important for the transition between D-band wave guides and the free space as well as the formation of the beam waist for an optimal axial resolution. As a consequence, the microwave optical axis is aligned 20 mm above the powered electrode in the plasma bulk with spatial (axial) resolution of 10 mm in the discharge center. Beside the optimum in axial resolution, the high temporal resolution of about 200 ns permits the investigation of fast fluctuations in the line integrated electron density due to plasma instabilities, pulsed mode operation, and laser photodetachment. The phase shift resolution was optimized down to 0.016°, which corresponds to a line integrated electron density of $5.3 \times 10^{13}\,m^{-2}$ and an averaged electron density of $5.3 \times 10^{14}\,m^{-3}$, respectively, assuming the electrode diameter as effective microwave path length.

Microwave interferometry and laser photodetachment are simultaneously applied to determine the negative atomic oxygen ion density in a low pressure capacitively coupled rf oxygen plasma, which is presented in more detail in Ref. 19. The frequency doubled, 10 Hz pulsed Nd:YAG laser with an expanded beam diameter of 13 mm is merged with the Gaussian microwave beam under an angle of 12.6° (Fig. 1). By use of appropriate experimental conditions, e.g., laser pulse energy greater than 300 mJ, the detached electrons correspond to the negative ion density within the overlapping volume of the microwave and laser beam.

III. RESULTS

A. Electron and negative ion density—operation modes at different electronegativity

The variation of rf power between 20 and 100 W reveals line integrated electron densities from 3×10^{14} to $10^{16}\,m^{-2}$ in the plasma on-phase at 40 Pa. (Fig. 2(a)). In particular, a significant increase of the electron density is found for rf power larger than 50 W or -220 V self-bias voltage, respectively. This correlates with a reduction of the line integrated negative oxygen ion density and the electronegativity ($\tilde{n}_-/\tilde{n}_e$) from about 4 to 0.03, respectively, see Fig. 2(b). Hence, a distinct separation between two different discharge modes was found, which is discussed more detailed in

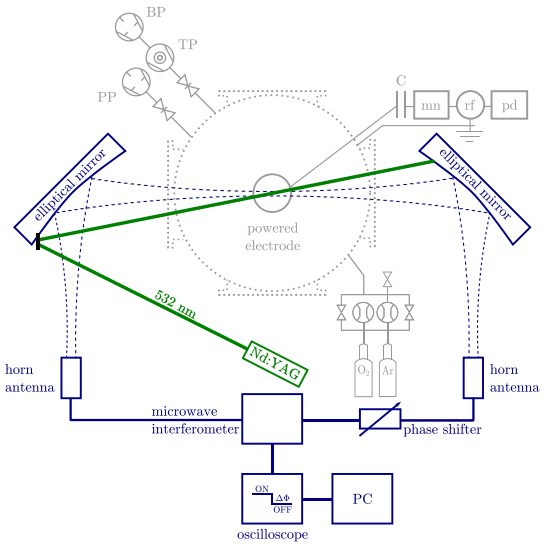

FIG. 1. Schematic sketch of the experimental setup with vacuum equipment for low pressure plasma processing, rf power supply and matching network, as well as the implementation of the 160.28 GHz Gaussian beam microwave interferometer and Nd:YAG laser for photodetachment.

Ref. 19. These investigations have shown that the first mode is the α-mode of the discharge for rf power less than 50 W and is indicated as the high electronegative mode. Usually, the α-mode is characterized by a higher electron temperature T_e, which reveals higher rate coefficients ($k_{aX}, k_{a\Delta}$) for dissociative electron attachment, see Table II. The second discharge mode for rf power larger than 50 W is indicated as the low electronegative mode which is connected with the transition into the γ-mode of the discharge. This mode exhibits a higher electron density at low electron temperature.[20]

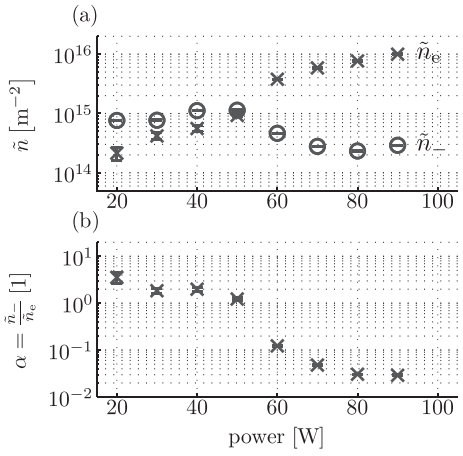

FIG. 2. (a) Mean line integrated electron density $\tilde{n}_e$ (×) and negative ion density $\tilde{n}_-$ (○) as a function of rf power in oxygen rf plasma (40 Pa, 5 sccm), measured by microwave interferometry and simultaneous laser photodetachment.[19] (b) Proportion of the negative ion density to the electron density (electronegativity).

TABLE II. Rate coefficients for attachment, recombination, detachment, and charge transfer processes in an oxygen discharge.

Reaction	Rate coefficient (m^3/s)	Remarks	Ref.
	k_{aX}		
	$8.8 \times 10^{-17} \exp\left(\frac{-4.4}{T_e}\right)$		21
	$k_{a\Delta}$		
	$2.28 \times 10^{-16} \exp\left(\frac{-2.29}{T_e}\right)$		29
(7)	k_{re}		
	1.4×10^{-13}		21
(8)	k_{r-}		
	9.6×10^{-14}		21
(9)	k_{r2-}		
	$4.2 \cdot 10^{-13}$		21
(10)	k_{dO}		
	1.4×10^{-16}		21
	2.3×10^{-16}		22
	2.0×10^{-16}		27
(11)	k_{d2O}		
	3.3×10^{-16}		21
(12)	k_{dX}	E/N [Td]	
	2.7×10^{-20}	91	21
	2.4×10^{-18}	121	21
	2.5×10^{-17}	200	21
(13)	$k_{d\Delta}$		
	3.0×10^{-16}		21
	1.9×10^{-16}		22
	3.0×10^{-16}		27
	1.1×10^{-16}	$T_g = 300$ K	25
	8.6×10^{-17}	$T_g = 300$ K	26
(14)	$k_{d2\Delta}$		
	2.0×10^{-16}		21
(15)	$k_{c\Delta}$		
	1.0×10^{-16}		30

The lower electron temperature reduces the dissociative electron attachment rate coefficients and gives an explanation for the low electronegativity.

In particular, these two modes provide significantly different afterglow behavior in a 10 Hz pulsed oxygen discharge. The different temporal behavior of the electron density is exemplarily shown in Figure 3 for high rf power at 91 W (low electronegativity, Fig. 3(a)) and low rf power at 48 W (high electronegativity, Fig. 3(b)), respectively, both at 40 Pa. Here, the rf power is enabled at −50 ms and disabled at 0 ms. The line integrated electron density in the case of higher rf power at 91 W (−360 V self-bias voltage) increases significantly in a few milliseconds and rises to a steady state value of about 10^{16} m^{-2}. After disabling the rf power, the electron density decreases immediately. Here the afterglow behavior is similar to an electropositive plasma like argon, which is discussed in detail in Sec. III B. In the high electronegative mode at lower rf power (48 W, −200 V self-bias voltage), the line integrated electron density also quickly rises after enabling the rf power, but achieves about one order of magnitude lower steady state value of 0.8×10^{15} m^{-2}. In contrast to the afterglow behavior

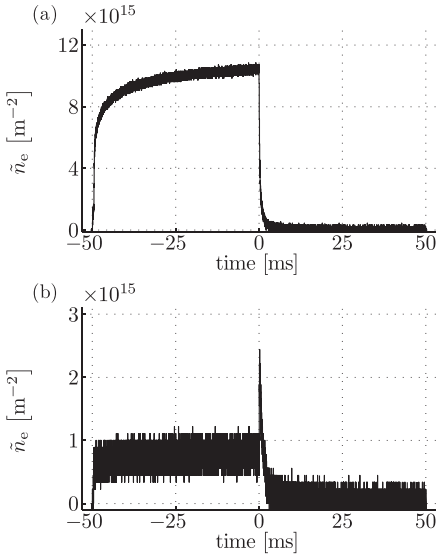

FIG. 3. Temporally resolved line integrated electron density in a 10 Hz (50% duty cycle) pulsed oxygen rf plasma (40 Pa, 5 sccm) at rf power of (a) 91 W (low electronegative mode) and (b) 48 W (high electronegative mode), respectively. The rf power is enabled at −50 ms and disabled at 0 ms.

of the low electronegative mode, an additional increase of the electron density up to $2 \times 10^{15}\,\mathrm{m}^{-2}$ is measured in the early afterglow, see Sec. III C.

B. Afterglow behavior in the low electronegative mode

A direct comparison regarding the afterglow behavior of oxygen and argon for 91 W and 40 Pa is presented in Figure 4. For both gases, the electron density immediately decreases after disabling the rf power. However, some differences in the afterglow behavior are perceived. The time constant of the electron density reduction in oxygen is about 1.5 ms, which is much shorter than in argon. Additionally, the electron kinetics in oxygen rather suggests to be described with a second order reaction kinetics, whereas in argon a first order reaction kinetics seems to be sufficient. The primary loss channels for the electrons in the argon afterglow are diffusion and surface recombination. Contrary, in the oxygen afterglow, the electrons seem to be lost due to dissociative recombination and diffusion processes.

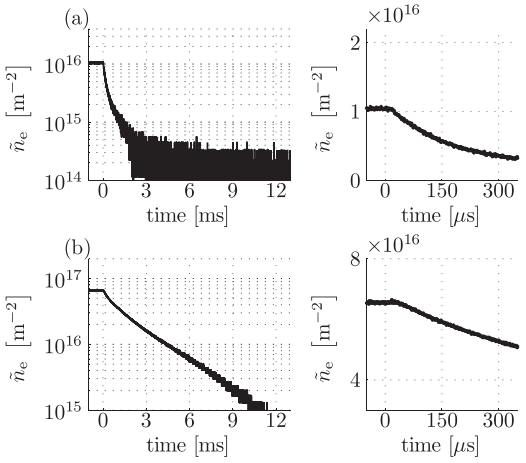

FIG. 4. Total and early afterglow behavior of the line integrated electron density of a 10 Hz (50% duty cycle) pulsed (a) oxygen and (b) argon rf plasma (91 W, 40 Pa, 5 sccm).

C. Afterglow behavior in the high electronegative mode—electron density peaks

Electron density peaks appear in the early afterglow within the pressure range from 20 to 100 Pa below 50 W rf power and −220 V self-bias voltage, respectively. In Figure 5, the line integrated electron density is plotted over the total and the early afterglow phase of a 10 Hz pulsed oxygen rf plasma at 40 Pa and 24 W. The line integrated electron density increases to $1.3 \times 10^{15}\,\mathrm{m}^{-2}$ within 200 μs in the early afterglow. This value is about four times larger than the on-phase line integrated electron density of $0.3 \times 10^{15}\,\mathrm{m}^{-2}$.

In Figure 6(a), the mean line integrated on-phase electron density ($\tilde{n}_e$) is shown in comparison to the electron peak density ($\tilde{n}_{e,P}$) in the afterglow for 40 Pa and rf power values from 20 to 50 W. The mean line integrated electron density rises with increasing rf power from 3×10^{14} to $7 \times 10^{14}\,\mathrm{m}^{-2}$. The electron peak density increases from 2×10^{15} to $2.5 \times 10^{15}\,\mathrm{m}^{-2}$. The difference of the peak and mean line integrated electron density, divided by the mean line integrated electron density (Fig. 6(b)) is a measure for the electronegativity. The electronegativity decreases from about 5.5 to 2.5 with rising rf power. This confirms the behavior of the electronegativity determined from the measured electron and negative ion density in the plasma on-phase, see Fig. 2(b). The temporal increase of the electron density to the peak value can be approximated by an exponential function, see Fig. 5. The corresponding time constant in the exponential function decreases from about 60 to 30 μs with rising rf power from 24 to 45 W, see Fig 6(c).

The increasing electron density in the afterglow is connected with the detachment of negative atomic oxygen ions O^-, e.g., by collisions with atomic oxygen O (1), ground state molecules $O_2(X^3\Sigma_g^-)$ (2), or metastable oxygen molecules $O_2(a^1\Delta_g)$ (3).

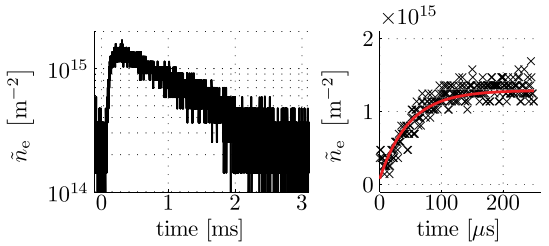

FIG. 5. Total and early afterglow behavior of the line integrated electron density of a 10 Hz (50% duty cycle) pulsed oxygen plasma (24 W, 40 Pa, 5 sccm). Additionally, the exponential fit function (6) $\tilde{n}_e(t) = \tilde{n}_e(0) + [\tilde{n}_{e,P} - \tilde{n}_e(0)] \times (1 - \exp(-t/\tau))$ for the early afterglow phase is shown. The corresponding fit parameters are $\tilde{n}_e(0) = 0.3 \times 10^{15}\,\mathrm{m}^{-2}$, $\tilde{n}_{e,P} = 1.3 \times 10^{15}\,\mathrm{m}^{-2}$, and $\tau = 53$ μs. (acronyms in Table I)

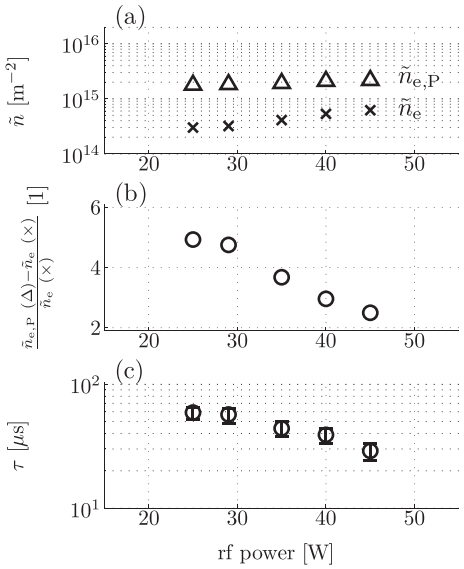

FIG. 6. (a) Line integrated electron density $\tilde{n}_e$ in the plasma on-phase compared with the afterglow electron peak density $\tilde{n}_{e,P}$, (b) the difference of peak ($\tilde{n}_{e,P}$) and on-phase electron density ($\tilde{n}_e$) divided by the on-phase electron density, and (c) the time constant (τ) of the electron density increase in the early afterglow versus rf power variation at 40 Pa and 5 sccm in an oxygen discharge.

$$O^- + O(^3P) \xrightarrow{k_{dO}} O_2(X^3\Sigma_g^-) + e, \quad (1)$$

$$O^- + O_2(X^3\Sigma_g^-) \xrightarrow{k_{dX}} \text{products} + e \quad (2)$$

$$O^- + O_2(a^1\Delta_g) \xrightarrow{k_{d\Delta}} \text{products} + e \quad (3)$$

Taking these processes into calculation as the main electron source, they are also aligned with the consumption of negative ions according to the following first order rate equation:

$$\frac{dn_e}{dt} = -\frac{dn_-}{dt} = (k_{dO}n_O + k_{d\Delta}n_\Delta + k_{dX}n_X)n_- = \frac{1}{\tau}n_-. \quad (4)$$

If one assumes constant densities of the involved neutral species within the early afterglow phase, the rate Eq. (4) can be solved for the negative ion (5) and electron (6) density taking into account the corresponding initial conditions for negative ions $n_-(0) = n_{e,P} - n_e(0)$ and electrons $n_e(0)$, respectively,

$$n_-(t) = n_-(0) \cdot \exp(-t/\tau) \propto [n_{e,P} - n_e(0)] \times (\exp(-t/\tau)), \quad (5)$$

$$n_e(t) = n_e(0) + [n_{e,P} - n_e(0)] \times (1 - \exp(-t/\tau)). \quad (6)$$

Thereby, $n_{e,P}$ is the electron afterglow peak density and τ the corresponding effective time constant. Figure 5 displays exemplarily the evaluated fit function for 40 Pa and 24 W and leads to a time constant of $\tau = 53\,\mu s$. The exponential function fits very well to the experimental data, which is a first indication that the detachment of the negative ions is an important channel of electron production in the afterglow. To benchmark these estimations above, it was measured the temporal behavior of the negative ion density $\tilde{n}_-$ in the afterglow. The comparison of the measured increasing electron density and the decreasing negative ion density is shown in Figure 7. For reasons of comparability, the electron density growth is plotted as $(\tilde{n}_{e,P} - \tilde{n}_e(t))/[\tilde{n}_{e,P} - \tilde{n}_e(0)] = \exp(-t/\tau)$ and the negative ion decrease as $\tilde{n}_-(t)/\tilde{n}_-(0) = \exp(-t/\tau)$, respectively. Both exponential functions are following the same time constant $\tau = 53\,\mu s$, as it is assumed in Eqs. (5) and (6). To classify the measured time constant, we discuss the considered detachment processes in Eq. (4). The detachment of negative ions by neutral atomic oxygen can be neglected because of its low density in the order of magnitude of 10^{19} m^{-3}, see also Sec. III D. Further, the detachment rate coefficient for ground state oxygen molecules strongly declines with decreasing reduced electric field strength, e.g., over three orders of magnitude by reduced electric field reduction from 200 to 90 Td.[21] For our discharge conditions, this value of the rate coefficient should be about $k_{dX} = 10^{-18}\,m^3s^{-1}$. Using the ideal gas law for 40 Pa and 300 K, the molecular oxygen ground state density is approximately $n_X = 10^{22}\,m^{-3}$. Therefore, the time constant for this detachment reaction is about $(k_{dX} \cdot n_X)^{-1} \propto 100\,\mu s$. The time constant for the detachment reaction with metastables can be estimated in the same way. The metastable density is assumed to be approximately 10% of the ground state density.[22–24] This reaction channel is important and has to be considered. First, the corresponding detachment rate coefficient of about $k_{d\Delta} = 10^{-16}\,m^3\,s^{-1}$ is significantly larger[21,22,25–27] compared to that of ground state molecular oxygen, and, second, the metastable molecular oxygen has a long lifetime up to 10^3 s.[21,28] Under the used discharge conditions, the effective life time is in the millisecond range. Hence, the detachment of negative atomic oxygen ions by metastable molecular oxygen is a significant reaction channel. Following, the time constant $(k_{d\Delta} \cdot n_\Delta)^{-1} = 10\,\mu s$ is one order of magnitude lower compared to the detachment reaction with molecular oxygen ground state $O_2(X^3\Sigma_g^-)$. The estimated time constants and the comparison with the measured values of between 60 µs and 20 µs reveal the important role of the metastable molecular oxygen in negative ion detachment.

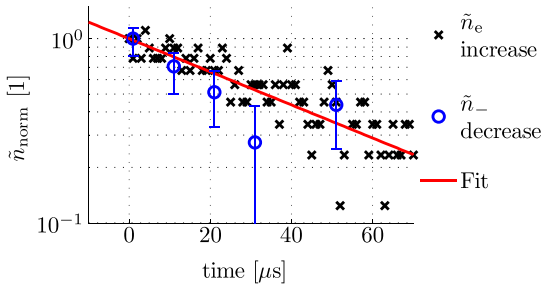

FIG. 7. Fit of the re-arranged analytical functions for electrons (6) $(\tilde{n}_{e,P} - \tilde{n}_e(t))/[\tilde{n}_{e,P} - \tilde{n}_e(0)] = \exp(-t/\tau)$ (×) and negative ions (5) $\tilde{n}_-(t)/\tilde{n}_-(0) = \exp(-t/\tau)$ (○) to the experimental data. Whereby, the acronyms are explained in Table I. As expected, both exponential functions have about the same time constant of 53 µs, which reveals the electron production by negative ion detachment in the early afterglow.

D. Modeling of the afterglow behavior

The electron density afterglow behavior of the pulsed cc-rf oxygen discharge is described using a 0d rate equation model. The following elementary processes (7)–(15) are considered involving recombination, detachment, and charge transfer reactions. The included neutral particles are molecular ground state oxygen ($O_2(X^3\Sigma_g^-)$), molecular metastable oxygen ($O_2(a^1\Delta_g)$), and atomic oxygen (O). The charged particles are electrons (e) and negative oxygen ions (O^-, O_2^-) as well as the positive molecular oxygen ions (O_2^+),

$$O_2^+ + e \xrightarrow{k_{re}} O(^3P) + O(^3P), \tag{7}$$

$$O_2^+ + O^- \xrightarrow{k_{r-}} O_2(X^3\Sigma_g^-) + O(^3P), \tag{8}$$

$$O_2^+ + O_2^- \xrightarrow{k_{r2-}} O_2(X^3\Sigma_g^-) + O_2(X^3\Sigma_g^-), \tag{9}$$

$$O^- + O(^3P) \xrightarrow{k_{dO}} O_2(X^3\Sigma_g^-) + e, \tag{10}$$

$$O_2^- + O(^3P) \xrightarrow{k_{d2O}} O_2(X^3\Sigma_g^-) + O(^3P) + e, \tag{11}$$

$$O^- + O_2(X^3\Sigma_g^-) \xrightarrow{k_{dX}} O_3 + e, \tag{12}$$

$$O^- + O_2(a^1\Delta_g) \xrightarrow{k_{d\Delta}} O_3 + e, \tag{13}$$

$$O_2^- + O_2(a^1\Delta_g) \xrightarrow{k_{d2\Delta}} O_2(X^3\Sigma_g^-) + O_2(X^3\Sigma_g^-) + e, \tag{14}$$

$$O^- + O_2(a^1\Delta_g) \xrightarrow{k_{c\Delta}} O_2^- + O(^3P). \tag{15}$$

Not considered are any attachment reactions of free electrons with ground state or metastable molecules because of their rather low reaction rate coefficients (k_{aX}, $k_{a\Delta}$) at rather low electron temperature T_e, see Table II. As known from literature,[14,15] the electron temperature decreases over orders of magnitudes in the nanosecond timescale after disabling the rf power. Therefore, the attachment reaction coefficients rapidly decrease.

The rate equations (16)–(21) result from the elementary reactions (7)–(15),

$$\frac{dn_{O_2^+}}{dt} = -k_{r-}n_{O_2^+}n_{O^-} - k_{r2-}n_{O_2^+}n_{O_2^-} - k_{re}n_{O_2^+}n_e - \frac{D_a}{L_D^2}n_{O_2^+}, \tag{16}$$

$$\frac{dn_{O_2^-}}{dt} = -k_{r2-}n_{O_2^-}n_{O_2^+} - k_{d2O}n_{O_2^-}n_O - k_{d2\Delta}n_{O_2^-}n_\Delta + k_{c\Delta}n_{O^-}n_\Delta, \tag{17}$$

$$\frac{dn_{O^-}}{dt} = -k_{r-}n_{O^-}n_{O_2^+} - k_{dO}n_{O^-}n_O - k_{d\Delta}n_{O^-}n_\Delta - k_{dX}n_{O^-}n_X - k_{c\Delta}n_{O^-}n_\Delta, \tag{18}$$

$$\frac{dn_e}{dt} = +k_{dO}n_{O^-}n_O + k_{d\Delta}n_{O^-}n_\Delta + k_{d2O}n_{O_2^-}n_O + k_{d2\Delta}n_{O_2^-}n_\Delta - k_{re}n_en_{O_2^+} - \frac{D_a}{L_D^2}n_e, \tag{19}$$

$$\frac{dn_\Delta}{dt} = -k_{d\Delta}n_\Delta n_{O^-} - k_{c\Delta}n_\Delta n_{O^-} - k_{d2\Delta}n_\Delta n_{O_2^-}, \tag{20}$$

$$\frac{dn_O}{dt} = -k_{dO}n_On_{O^-} + k_{r-}n_{O_2^+}n_{O^-} + k_{c\Delta}n_{O^-}n_\Delta. \tag{21}$$

Additionally, it is considered an effective loss term for positive ions and electrons due to ambipolar diffusion, taking into account the effective diffusion time constant $\tau_D = L_D^2/D_a$, with the effective diffusion length L_D and the ambipolar diffusion coefficient D_a, respectively. The diffusive loss of negative ions in the early afterglow at high electronegativity was neglected because of the short time constant for detachment reactions (few 10 µs) compared to diffusion time constant in the millisecond scale. A rough estimation of the ambipolar diffusion coefficient in the afterglow at the pressure of 40 Pa and room temperature yields $D_a \propto 0.1\,m^2/s$. By use of the diffusion length of 20 mm, the diffusion time constant is about 4 ms. The diffusion length (L_D) is set to 20 mm (distance from the microwave beam axis to the powered electrode).

This set of differential equations is numerically solved, with a defined time step of $\Delta t = 1$ µs. Moreover, the numerical fit routine is treated as a least square fit to achieve the best accordance of the modeled and the measured electron density. This requires some initial values for the model at $t = 0$, which are allowed to differ within some suitable limits during the fit routine. The density of O_2^- ($n_{O_2^-}$) is allowed to be in the range of $0 \ldots 3 \times 10^{15}\,m^{-3}$. The atomic oxygen density (n_O) amounts to about $10^{19}\,m^{-3}$, which was shown in a similar oxygen rf plasma by two photon laser-induced fluorescence spectroscopy (TALIF).[31–33] The density of metastable oxygen molecules (n_Δ) is in the order of 10% of the total ground state gas pressure[22–24] The ambipolar diffusion coefficient is between $D_a = 0.05 \ldots 1.5\,m^2/s$. The density of the positive oxygen ion ($n_{O_2^+}$) was determined by the quasineutrality equation $n_{O_2^+} = n_e + n_{O^-} + n_{O_2^-}$. The corresponding electron and negative ion density were taken from the experiment (Sec. II). The measurement provides line integrated electron density ($\tilde{n}_e$) and atomic negative oxygen ion density ($\tilde{n}_{O^-}$), which were converted into absolute values by assuming an averaged density above the diameter of the powered electrode (0.1 m) as effective absorption length of the microwave interferometry. Consequently, the averaged particle density was calculated with $n[m^{-3}] = \tilde{n}[m^{-2}]/0.1\,m$.

The required rate coefficients are listed in Table II. Many rate coefficients are taken from Eliasson and Kogelschatz.[21] New experimental results were presented by Belostotsky *et al.*[22] and Midey *et al.*[25,26] Unfortunately, for some elementary reactions different rate coefficients were found. In that case, an averaged rate coefficient has been taken.

Under this requirements, this 0d model is used to evaluate the electron density afterglow behavior for the low rf power case of 48 W (Fig. 3(b)) and the high rf power case of 91 W (Figs. 3(a) and 4(a)) both at a gas pressure of 40 Pa oxygen. The determined optimal initial parameters from the fit routine for O_2^-, $O_2(a^1\Delta_g)$, O and D_a are listed in Table III. Furthermore, this table shows the initial electron density (n_e) and negative atomic oxygen density (n_{O^-}) from the experiment.

TABLE III. Initial conditions for the electron and negative atomic oxygen ion density from measurements, and the optimized initial conditions of other densities ($n_{O_2^-}$, n_Δ, n_O) as well as the ambipolar diffusion coefficient by least square fit routine of the numerical 0d model calculations.

	48 W	91 W
n_e (Exp.)	$7.6 \times 10^{15}\,m^{-3}$	$1.05 \times 10^{17}\,m^{-3}$
n_{O^-} (Exp.)	$1.14 \times 10^{16}\,m^{-3}$	$3 \times 10^{15}\,m^{-3}$
$n_{O_2^-}$	$10^{13}\,m^{-3}$	$10^{13}\,m^{-3}$
n_Δ	$10^{20}\,m^{-3}$	$10^{20}\,m^{-3}$
n_O	$10^{19}\,m^{-3}$	$10^{19}\,m^{-3}$
D_a	$0.05\,m^2/s$	$0.05\,m^2/s$

The model reveals that the initial O_2^- density is approximately 10% of the O^- density. This is in good accordance with other investigations in rf oxygen plasmas.[34,35] The temporal behavior of the electron density in the afterglow is shown in Figure 8 by comparison of the measured electron density (gray) with the model calculation (×) for the high and low electronegative mode, respectively. Additionally, the temporal development of the negative ion densities (O^-, O_2^-) from the model calculations is included. The model supports very well the discussion to Eqs. (5) and (6) concerning the density behavior in the early afterglow and confirms the decreasing negative ion density from the laser photodetachment experiment (Fig. 7).

For the case of low rf power at 48 W, the model shows that at first the electron density increases, reaching a maximal value and subsequently decreases. Hence, the model qualitatively shows the same behavior as observed in the experimental determined electron density. Whereby, the modeled

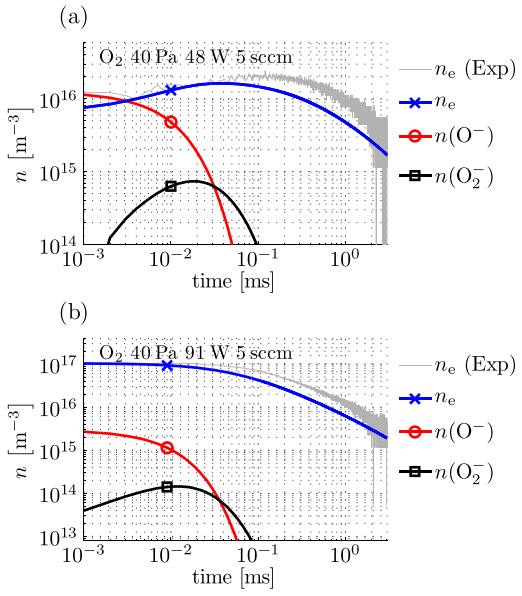

FIG. 8. Comparison between the experimental (gray) and model based (×) electron density afterglow behavior for (a) 48 W and (b) 91 W, both at gas pressure of 40 Pa. Moreover, the calculated negative ion density of O^- (○) and of O_2^- (□) is shown.

electron density is underestimated compared to the measured density, in particular, in the late afterglow. The late afterglow is rather dominated by diffusion loss and surface recombination which is not correctly considered in the applied 0d model. The negative ion density measurement probes the overlapping volume of the laser and the microwave beam, which is smaller than the effective line of sight of the microwave beam for the measurement of the line integrated electron density.[19] Further, the absolute density of the electrons and the negative atomic oxygen ions were estimated by an averaged density profile above the powered electrode, as mentioned above. This may contribute to an underestimation of the negative atomic oxygen ion density. Parameter studies of the model have shown that the detachment of the negative ions is the most important reaction channels for electron production in the early afterglow of the rf oxygen plasma in the high electronegative mode. In particular, the metastable molecular oxygen plays an essential role.

The temporal behavior of the electron density in the afterglow of the oxygen rf plasma in the low electronegative mode is plotted in Figure 8(b). In comparison with the discussed afterglow behavior of the high electronegative mode, the electron density is immediately decreasing after disabling the rf power at $t = 0$. The negative ion densities are up to one order of magnitude lower as expected. Parameter studies of the model for this mode have shown that the decreasing electron density is dominated by the recombination and diffusion processes.

IV. CONCLUSION

The 10 Hz (50% duty cycle) pulsed cc-rf oxygen plasma was systematically studied by Gaussian beam microwave interferometry at 160 GHz and laser photodetachment, simultaneously. In particular, the temporal development of the electron density in the afterglow was investigated for two different operation modes of the oxygen rf plasma, the high and low electronegative modes, respectively.

In the low electronegative mode, the afterglow behavior is similar to an electropositive plasma like argon. In the high electronegative mode, a significant electron density peak in the early afterglow is observed, which can be up to six times larger than the mean plasma on-phase electron density. The electron density peaks have their origin in the electron production due to detachment of negative atomic oxygen ions, in particular, by collisions with metastable molecular oxygen. Complementary, the decreasing negative ion density in the early afterglow was measured by simultaneous laser photodetachment. The negative ion loss and the electron production in the early afterglow could be well described using one simple first order rate equation for the negative ion detachment and electron production. The total afterglow was modeled with a 0d rate equation system taking into account the particle balance of six species (electrons, O_2^+, O^-, O_2^-, $O_2(a^1\Delta_g), O$) and nine elementary reactions involving recombination, detachment, and charge transfer. Furthermore, a loss term due to ambipolar diffusion was included. Within the limits of the 0d model, it describes very well the temporal electron density development in the afterglow of

both electronegative modes observed in the cc-rf plasma in oxygen. Parameter studies reveal the significant role of metastable molecular oxygen.

ACKNOWLEDGMENTS

This work was supported by the Deutsche Forschungsgemeinschaft (DFG) in the framework of the Sonderforschungsbereich Transregio 24 "Fundamentals of Complex Plasmas," project B5.

[1]V. I. Demidov, S. V. Ratynskaia, and K. Rypdal, "Electric probes for plasmas: The link between theory and instrument," Rev. Sci. Instrum. **73**, 3409 (2002).
[2]S. Arndt, F. Sigeneger, H. Testrich, and C. Brandt, "Self-consistent analysis of the spatial relaxation of a disturbed neon glow discharge," Plasma Chem. Plasma Process. **25**, 567 (2005).
[3]C. Brandt, H. Testrich, R. Kozakov, and C. Wilke, "Investigation of the disturbance of a Langmuir probe and its influence on measurement results," Rev. Sci. Instrum. **77**, 023504 (2006).
[4]V. A. Godyak, R. B. Piejak, and B. M. Alexandrovich, "Measurements of electron energy distribution in low-pressure RF discharges," Plasma Sources Sci. Technol. **1**, 36 (1992).
[5]V. A. Godyak, R. B. Piejak, and B. M. Alexandrovich, "Probe diagnostics of non-Maxwellian plasmas," J. Appl. Phys. **73**, 3657 (1993).
[6]S. Klagge, "Sondendiagnostik, Weiterbildungskurs Plasmaphysik," Vorlesungsmanuskript Sektion Physik/Elektronik, Universität Greifswald (1993).
[7]H. Sabadil, S. Klagge, and M. Kammeyer, "Langmuir probe measurements of axial variation of plasma parameters in 27.1 MHz rf oxygen planar discharges," Plasma Chem. Plasma Process. **8**, 425 (1988).
[8]G. Wehner and G. Medicus, "Reliability of probe measurements in hot cathode gas diodes," J. Appl. Phys. **23**, 1035 (1952).
[9]T. L. Thomas and E. L. Battle, "Effects of contamination on Langmuir probe measurements in glow discharge plasmas," J. Appl. Phys. **41**, 3428 (1970).
[10]R. A. Olson and D. R. Nordlund, "Automatic plotting of Langmuir-probe susceptance- and conductance-voltage curves," J. Appl. Phys. **43**, 2780 (1972).
[11]J. A. Wagner and H.-M. Katsch, "Negative oxygen ions in a pulsed RF-discharge with inductive coupling in mixtures of noble gases and oxygen," Plasma Sources Sci. Technol. **15**, 156 (2006).
[12]H. M. Katsch, C. Manthey, and H. F. Döbele, "Charge carrier dynamics in a pulsed inductive RF discharge in oxygen," Plasma Sources Sci. Technol. **12**, 475 (2003).
[13]S. Panda, D. J. Economou, and M. Meyyappan, "Effect of metastable oxygen molecules in high density power-modulated oxygen discharges," J. Appl. Phys. **87**, 8323 (2000).
[14]A. Brockhaus, G. F. Leu, V. Selenin, Kh. Tarnev, and J. Engemann, "Electron release in the afterglow of a pulsed inductively-coupled radio-frequency oxygen plasma," Plasma Sources Sci. Technol. **15**, 171 (2006).
[15]K. E. Greenberg and G. A. Hebner, "Electron and metastable densities in parallel-plate radio-frequency discharges," J. Appl. Phys. **73**, 8126 (1993).
[16]L. J. Overzet, "Microwave diagnostic results from the gaseous electronics conference RF reference cell," J. Res. Natl. Inst. Stand. Technol. **100**, 401 (1995).
[17]C. Gaman, S. K. Karkari, and A. R. Ellingboe, "Observation of transient electron density rise in an afterglow H_2 plasma with confined capacitive radio-frequency source," in *28th ICPIG*, July 15-20 (2007).
[18]K. Dittmann, C. Küllig, and J. Meichsner, "160 GHz Gaussian beam microwave interferometry in low density RF plasmas," Plasma Sources Sci. Technol. **21**, 024001 (2012).
[19]C. Küllig, K. Dittmann, and J. Meichsner, "A novel approach for negative ion analysis using 160 GHz microwave interferometry and laser photodetachment in oxygen cc-rf plasmas," Plasma Sources Sci. Technol. **19**, 065011 (2010).
[20]S. Klagge, "Space- and direction-resolved Langmuir probe diagnostic in RF planar discharges," Plasma Chem. Plasma Process. **12**, 103 (1992).
[21]B. Eliasson and U. Kogelschatz, "Basic data for modelling of electrical discharges in gases: oxygen," Technical Report No. KLR 86-11 C (Brown Boveri Forschungszentrum CH-5405 Baden, 1986).
[22]S. G. Belostotsky, D. J. Economou, D. V. Lopaev, and T. V. Rakhimova, "Negative ion destruction by $O(^3P)$ atoms and $O_2(a^1\Delta_g)$ molecules in an oxygen plasma," Plasma Sources Sci. Technol. **14**, 532 (2005).
[23]M. Shibata, N. Nakano, and T. Makabe, "Effect of $O_2(a^1\Delta_g)$ on plasma structures in oxygen radio frequency discharges," J. Appl. Phys. **80**, 6142 (1996).
[24]J. T. Gudmundsson, "Recombination and detachment in oxygen discharges: the role of metastable oxygen molecules," J. Phys. D: Appl. Phys. **37**, 2073 (2004).
[25]A. Midey, I. Dotan, S. Lee, W. T. Rawlins, M. A. Johnson, and A. A. Viggiano, "Kinetics for the reactions of O^- and O_2^- with $O_2(a^1\Delta_g)$ measured in a selected ion flow tube at 300 K," J. Phys. Chem. **111**, 5218 (2007).
[26]A. Midey, I. Dotan, and A. A. Viggiano, "Temperature dependences for the reactions of O^- and O_2^- with $O_2(a^1\Delta_g)$ from 200 to 700 K," J. Phys. Chem. **112**, 340 (2008).
[27]F. C. Fehsenfeld, D. L. Albritton, J. A. Burt, and H. I. Schiff, "Associative-detachment reactions of O^- and O_2^- by $O_2(^1\Delta_g)$," Can. J. Chem. **47**, 1793 (1969).
[28]G. G. Arutunyan and L. P. Babalyants, "Energetic characteristics of oxygen plasma," Contrib. Plasma Phys. **30**, 733 (1990).
[29]J. T. Gudmundsson, A. M. Marakhtanov, K. K. Patel, V. P. Gopinath, and M. A. Lieberman, "On the plasma parameters of a planar inductive oxygen discharge," J. Phys. D: Appl. Phys. **33**, 1323 (2000).
[30]I. A. Kossyi, A. Yu. Kostinsky, A. A. Matveyev, and V. P. Silakov, "Kinetic scheme of the non-equilibrium discharge in nitrogen-oxygen mixtures," Plasma Sources Sci. Technol. **1**, 207 (1992).
[31]M. Geigl, S. Peters, O. Gabriel, B. Krames, and J. Meichsner, "Analysis and kinetics of transient species in electrode near plasma and plasma boundary sheath of rf plasmas in molecular gases," Contrib. Plasma Phys. **45**, 369 (2005).
[32]A. Goehlich, T. Kawetzki, and H. F. Döbele, "On absolute calibration with xenon of laser diagnostic methods based on two-photon absorption," J. Chem. Phys. **108**, 9362 (1998).
[33]H. M. Katsch, A. Tewes, E. Quandt, A. Goehlich, T. Kawetzki, and H. F. Döbele, "Detection of atomic oxygen: Improvement of actinometry and comparison with laser spectroscopy," J. Appl. Phys. **88**, 6232 (2000).
[34]D. Vender, W. W. Stoffels, E. Stoffels, G. M. W. Kroesen, and F. J. de Hoog, "Charged-species profiles in electronegative radio-frequency plasmas," Phys. Rev. E **51**, 2436 (1995).
[35]E. Stoffels, W. W. Stoffels, D. Vender, M. Kando, G. M. W. Kroesen, und F. J. de Hoog, "Negative ions in a radio-frequency oxygen plasma," Phys. Rev. E **51**, 2425 (1995).

Article V

2564 IEEE TRANSACTIONS ON PLASMA SCIENCE, VOL. 39, NO. 11, NOVEMBER 2011

Electron Density Oscillations in CC-RF Oxygen Plasma Investigated by Gaussian Beam Microwave Interferometry

Christian Küllig, Kristian Dittmann, and Jürgen Meichsner

***Abstract*—Gaussian beam microwave interferometry (160 GHz, beam waist of 5 mm) is applied to study the electron density in capacitively coupled radio-frequency (RF) oxygen plasma. The microwave interferometry provides immediately the line-integrated electron density without model assumptions. In the considered range of RF power and total pressure, the investigations have shown that the oxygen plasma is dominated by electron density oscillations due to the attachment-induced ionization instability. The frequency of the mostly nonharmonic oscillations ranges between 0.3 and 3 kHz with peak-to-peak line-integrated electron density variations up to 3.5×10^{15} m^{-2}.**

***Index Terms*—Electrons, interferometry, plasma diagnostics, plasma stability.**

THE LOW-pressure capacitively coupled radio-frequency (RF) plasma (CC-RF plasma) is widely used for plasma surface treatment, e.g., chemical modification, cleaning, etching, patterning, and thin-film deposition. In particular, the oxygen plasma is interesting both as a model system for studying electronegative plasmas and as reactive plasma in polymer surface modification, oxidation, and surface cleaning. In the fundamental research, the oxygen plasma is under special investigation as complex multispecies plasma consisting of positive and negative ions, electrons, metastable species, and reactive atomic oxygen. In particular, the electron density as an important plasma parameter has to be investigated to understand the discharge mechanisms in more detail. Aside from the widely applied Langmuir probe technique with all the known limitations, the microwave interferometry is a powerful tool in plasma diagnostics. This diagnostics has many advantages in comparison to the standard probe diagnostics but is not as common in low-density plasmas like the CC-RF discharge. In this paper, we present results of the 160 GHz microwave interferometry in the asymmetric CC-RF oxygen plasma, whereby the microwave propagation has to be described quasi-optical as a Gaussian beam. The measured phase shift is directly proportional to the line-integrated electron density. The main challenge of this diagnostics is the measurement of very small phase shifts on the order of 0.01°.

The experimental setup consists of a stainless steel vacuum chamber being 400 mm in height and diameter, respectively. An oxygen pressure between 10 and 100 Pa was obtained by means of a 16 m^{3}h^{-1} stage rotary pump in combination with a throttle valve to control the total pressure independent of the process gas flow via a mass flow controller at the constant gas flow rate of 5 sccm. The water-cooled planar RF electrode ($\varnothing$10 cm) was powered in the range of 10–100 W by means of a 13.56 MHz generator via a fully tunable π-type matching network. The shielding of the powered electrode and the chamber wall provide the grounded electrode. This leads to an asymmetric RF discharge with self bias voltages from -50 to -600 V, depending on RF power and total pressure.

The microwave interferometer consists of a frequency-stabilized heterodyne system operating at a frequency of 160.28 GHz. This frequency requires the Gaussian beam propagation theory to realize a proper alignment for the microwave transfer from the interferometer (waveguide) via a special designed horn antenna into free space and backward. Furthermore, two elliptical mirrors were used for redirecting and refocusing the microwave beam into the plasma center. The microwave optical axis was aligned 20 mm above the powered electrode in the RF bulk plasma. The beam waist was 5 mm at the discharge center. The temporal resolution of the interferometer amounts to 0.2 μs, and the phase shift resolution was optimized to 0.016° corresponding to a line-integrated electron density $\widetilde{n}_e = 5.3 \times 10^{13}$ m^{-2}.

Fig. 1 shows the color-coded oscillations of the line-integrated electron density for the RF power variation between 10 and 100 W and constant total pressure of 60 Pa. This figure only pictures the time-depending change of the line-integrated electron density, the background electron density was subtracted. The background density amounts to 10^{14} to 10^{16} m^{-2} with increasing RF power. The peak-to-peak values of the line-integrated electron density oscillations range from about 0.2 to 3.5×10^{15} m^{-2}. The oscillation frequencies were measured between 0.3 and 3 kHz.

In the presented case of a 60 Pa oxygen pressure, a stable RF plasma, which means the RF plasma without electron density oscillation, was only observed in the RF power range of 30–40 W. Generally, the line-integrated electron density oscillations were found at all investigated pressure values from 10 to 100 Pa, excluding specific ranges of RF power like that

Manuscript received December 1, 2010; revised April 26, 2011; accepted May 4, 2011. Date of publication July 22, 2011; date of current version November 9, 2011. This work was supported by the Deutsche Forschungsgemeinschaft in the framework of the Sonderforschungsbereich Transregio 24, Project B5.

The authors are with the Institute of Physics, University of Greifswald, D-17489 Greifswald, Germany (e-mail: kuellig@physik.uni-greifswald.de; dittmann@physik.uni-greifswald.de; meichsner@physik.uni-greifswald.de).

Digital Object Identifier 10.1109/TPS.2011.2156430

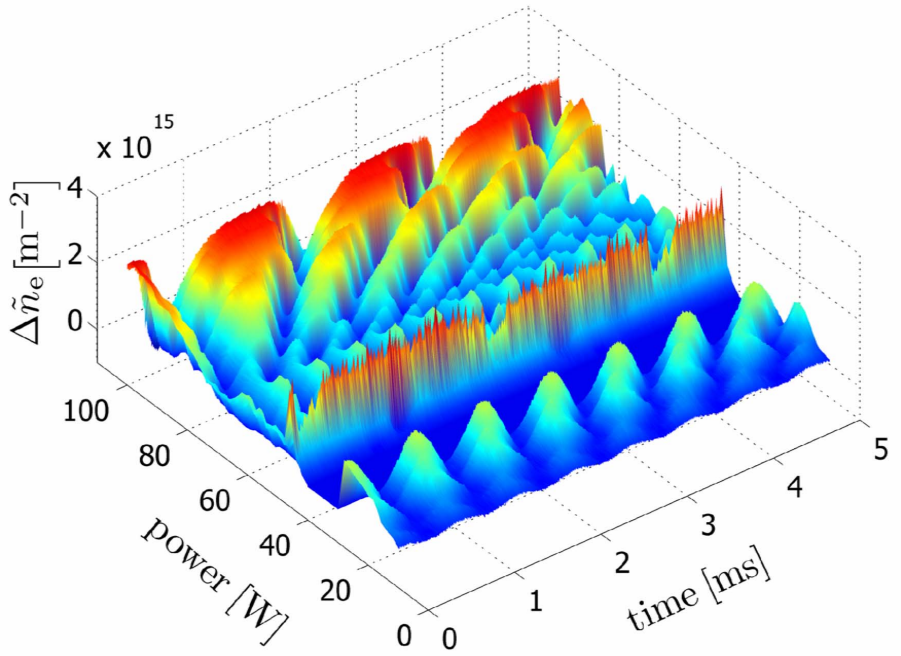

Fig. 1. Electron density oscillation due to attachment-induced ionization instability in an asymmetric CC-RF oxygen discharge (60 Pa, 5 sccm) in dependence on the RF power from 10 to 100 W. The different colors indicate the peak-to-peak line-integrated electron density variation ($\Delta\widetilde{n}_e$).

in Fig. 1. At total pressures from 70 to 100 Pa, no stable CW RF plasma was observed for all investigated values of RF power. Furthermore, the electron density oscillations were also found in pulsed RF plasmas (10 Hz, 50% duty cycle) with characteristic start-up time in the millisecond range.

The electron density oscillations have their origin in the known attachment-induced ionization instability [1]–[3]. The underlying mechanism of these instabilities was described in detail by Nighan and Wiegand [3]. A disturbance increases the initial electron density and results in a decrease of the electron temperature. In the case that the attachment rate coefficient $k_{\mathrm{att}}(T_e)$ decreases more strongly than the ionization rate coefficient $k_{\mathrm{ion}}(T_e)$, more electrons are produced effectively. Therewith, the initial disturbance is not compensated, and the instability is observed. This can be described by the critical ratio of the differential change of rate coefficients for attachment and ionization with electron temperature variation [3]. For the investigated RF plasma, the critical ratio may be approximately at $T_e = 1.6$ eV.

A second condition for the appearance of the instabilities is that the electron density has to be nearly the same value as the density of the negative oxygen ions. The behavior of electron and negative ion density has been discussed in more detail by Küllig *et al.* [4].

References

[1] A. Descoeudres, L. Sansonnens, and C. Hollenstein, "Attachment-induced ionization instability in electronegative capacitive RF discharges," *Plasma Sources. Sci. Technol.*, vol. 12, no. 2, pp. 152–157, May 2003.

[2] H.-M. Katsch, A. Goehlich, T. Kawetzki, E. Quandt, and H.-F. Döbele, "Attachment-induced ionization instability of a radio frequency excited discharge in oxygen," *Appl. Phys. Lett.*, vol. 75, no. 14, pp. 2023–2025, Oct. 1999.

[3] W. L. Nighan and W. J. Wiegand, "Influence of negative-ion processes on steady-state properties and striations in molecular gas discharges," *Phys. Rev. A*, vol. 10, no. 3, pp. 922–945, Sep. 1974.

[4] C. Küllig, K. Dittmann, and J. Meichsner, "A novel approach for negative ion analysis using 160 GHz microwave interferometry and laser photodetachment in oxygen CC-RF plasmas," *Plasma Sources Sci. Technol.*, vol. 19, no. 6, p. 065011, Dec. 2010.

Article VI

Contrib. Plasma Phys. **52**, No. 10, 836 – 846 (2012) / **DOI** 10.1002/ctpp.201200048

Dynamics and Electronegativity of Oxygen RF Plasmas

C. Küllig[1], **K. Dittmann**[1], **T. Wegner**[1], **I. Sheykin**[2], **K. Matyash**[1], **D. Loffhagen**[2], **R. Schneider**[1], and **J. Meichsner**[1]*

[1] Institute of Physics, University of Greifswald, Felix-Hausdorff-Str. 6, 17489 Greifswald, Germany
[2] Leibniz Institute for Plasma Science and Technology (INP Greifswald e.V.), Felix-Hausdorff-Str. 2, 17489 Greifswald, Germany

Received 25 May 2012, revised 17 August 2012, accepted 06 September 2012
Published online 08 November 2012

Key words Low pressure rf discharge, oxygen plasma, electron and negative ion density, plasma instability.

The capacitively coupled radio frequency plasma at 13.56 MHz in oxygen was systematically studied by 160 GHz Gaussian beam microwave interferometry at high temporal resolution (200 ns) and simultaneous laser photodetachment for electron and negative ion density analysis. Additionally, spatio-temporally resolved electric probe measurements were performed for comparison with microwave interferometry. A high and low electronegative operation mode was found in the asymmetric rf discharge. In the high electronegative mode it was shown the significant role of the metastable excited oxygen molecules in electron attachment and detachment processes. In particular, a temporary electron density increase is observed in the early afterglow of a pulsed rf plasma. The transition between both modes is driven by the rf power and the self-bias voltage, respectively. In connection with the phase resolved optical emission spectroscopy and the study of the electron heating mechanisms the transition into the low electronegative mode at higher rf power shows a relation to the alpha to gamma mode transition. Furthermore, electron density fluctuations are measured over a wide field of processing parameters, e.g. due to the attachment-induced ionization instability. PIC-MCC simulation and fluid model calculation of a symmetric oxygen rf discharge confirm the different electron heating mechanisms and the dominance of negative atomic oxygen ions.

1 Introduction

The non-thermal plasma in electronegative gases represents an extraordinary many particle system which reveals drastic changes in the physical and chemical properties compared with usual plasmas generated in electropositive gases [1]. Therefore, the fundamental investigation of such complex plasmas, consisting of electrons, multiple negative and positive ions as well as neutral transient and stable molecules, is still an ambitious task in the plasma physics. In particular, the electronegativity (ratio of negative ion to electron density) may strongly influence the plasma dynamics, e.g. the electron heating [2,3] and plasma stability [4,5] as well as the properties of the plasma boundary sheath [6,7]. In the case of plasmas with electronegative organic molecules the ion-molecule reactions are extended by charge transfer reactions with negative ions, which result in the formation of larger molecules and small clusters [8]. Furthermore, the electronegative plasmas have been applied in many plasma technologies, e.g. plasma treatment of material surfaces (chemical modification, cleaning, etching, patterning), thin film deposition, ozone production, exhaust gas cleaning and as electron capture in gas circuit-breaker [9]. Currently, the application of non-thermal plasmas at atmospheric pressure in life science is a hot topic [10]. Here, the negative ions are an important reaction partner, e.g. in generation of reactive oxygen-nitrogen molecules. The systematic investigations are focused on two electronegative gases as model systems, oxygen and tetrafluoromethane. Thereby, the low pressure capacitively coupled radio frequency plasma (cc-rf-plasma) was used for plasma generation. In this paper, the results are presented and discussed from the fundamental study of oxygen cc-rf plasmas. The experimental investigations are performed using high-end diagnostics. A specific Gaussian beam microwave interferometer (MWI) at 160 GHz (beam waist 5 mm) was introduced for electron density analysis at high temporal resolution (200 ns) simultaneously with the laser photodetachment of negative ions [2]. Additionally, the

* Corresponding author. E-mail: meichsner@physik.uni-greifswald.de, Phone: +49 3834 86 4740, Fax: +49 3834 86 4701

Contrib. Plasma Phys. **52**, No. 10 (2012) / www.cpp-journal.org

Langmuir probe technique is used to provide information on the spatial distribution of the plasma density and fluctuations of plasma parameters, respectively, for comparison with the line integrated electron density from MWI. Furthermore, the phase-resolved optical emission spectroscopy (PROES) was applied to study the rf sheath dynamics and electron heating [3].

The experimental investigations are in close connection with numerical and analytical modeling of the electronegative oxygen rf plasma. Beside a simple 0d rate equation model, the Particle-in-Cell method combined with Monte-Carlo collisions (PIC-MCC) [11] and a specific fluid model calculation (FMC) [12] are applied.

At the beginning, the experimental setup and diagnostics as well as the simulation and modeling methods are described briefly. Then, the high and low electronegative mode of the oxygen rf plasma is discussed and their influence on the afterglow behavior in pulsed plasmas. The transition into the low electronegative mode at higher rf power is explained together with the rf sheath dynamics and electron heating. Furthermore, the appearance of electron density fluctuations is discussed in connection with an attachment-induced ionization instability [13]. Finally, the conclusions and outlook involve a short summary, and gives the view on the exciting scientific questions and goals for the following study of electronegative plasmas, including tetrafluoromethane as a model system, within the collaborative research center "Fundamentals of Complex Plasmas" as well as by cooperation with external groups.

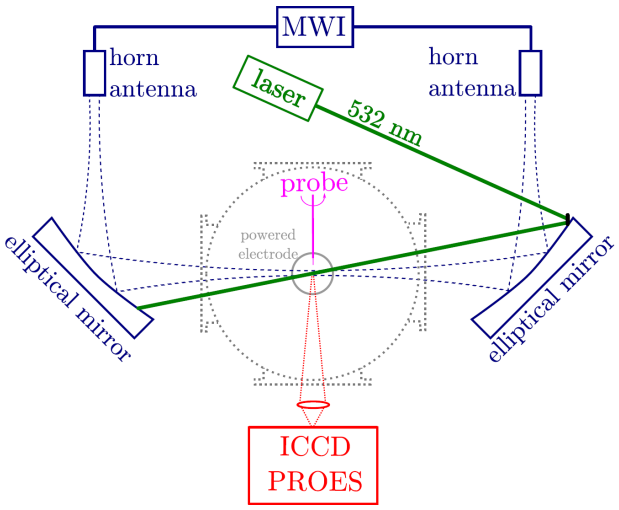

Fig. 1 Schematic sketch of the experimental setup and the implemented diagnostics composing the 160.28 GHz Gaussian beam microwave interferometry (MWI) for electron density measurements, the Nd:YAG laser for photodetachment of negative ions, the Langmuir probe system and the fast gateable ICCD camera for PROES measurements.

2 Experiment and modeling

2.1 Experimental setup and diagnostics

A cylindrical vacuum chamber with a volume of about 50 l was applied which houses a planar rf powered electrode with 100 mm in diameter, both made of stainless steel. The vacuum pumping and gas supply system allowed a base pressure of 5×10^{-5} Pa, whereas the plasma process is driven by a pressure of between 5 and 100 Pa at a constant gas flow rate of 5 sccm. The rf electrode was powered via a matching network in cw or pulsed mode operation by a 13.56 MHz generator at forward power from 5 to 150 W. Due to the larger grounded electrode (rf electrode shielding and chamber wall) an asymmetric rf discharge with self-bias voltage from -100 to -600 V is generated, [2, 14]. The MW interferometer for electron density analysis consists of a frequency stabilized (PLL) heterodyne system operating at a frequency of 160.28 GHz with output power of 1.3 mW, [14]. The Gaussian beam propagation theory is applied for the microwave free space propagation. Thereby, special designed cylindrical horn antennas and elliptical mirrors are used to realize carefully both, the microwave transformation from the rectangular waveguides into free space and vice versa as well as the changing of the propagation direction and re-focusing of the microwave beam into the plasma chamber with a Gaussian beam waist of $w_0 = 5$ mm (axial resolution 10 mm) 20 mm above the powered electrode in the bulk plasma. The resolution of the microwave interferometer is optimized for measuring line integrated electron densities down to 5×10^{13} m^{-2}. This corresponds

to an averaged electron density of $5 \times 10^{14}\,\mathrm{m}^{-3}$ using the electrode diameter as the effective line of sight length. In particular, a high temporal resolution of about 200 ns was achieved which is necessary for the analysis of fast electron density fluctuations, the laser photodetachment experiment and the afterglow study of pulsed plasmas. For the first time, the MWI and the laser photodetachment were simultaneously used to determine the line integrated negative oxygen ion density in cc-rf oxygen plasmas, [2]. Briefly, a frequency doubled, 10 Hz pulsed Nd:YAG laser with expanded beam diameter of 13 mm is merged with the Gaussian microwave beam under the angle of about 13°, (fig. 1). The laser pulse energy above 350 mJ ensures the detachment of all negative oxygen ions in the detection volume. Spatially resolved electric probe measurements were performed to get additional information on the axial and radial plasma density distribution and fluctuations in the floating potential due to plasma instabilities, respectively. The probe tip has a diameter of 250 µm and a length of 8 mm. The probe is passively rf compensated and the first and second harmonic in the probe current is additionally reduced by specific filter technique [15]. The PROES was applied to study the rf sheath dynamics and electron heating in oxygen rf plasma. Using the optical transition at 844 nm or 777 nm of atomic oxygen, the spatio-temporal pattern of the excitation rates provide detailed information on the rf sheath dynamics and the origin of the excitation due to different mechanisms of the electron heating or the excitation by fast heavy particles species within the rf cycle (74 ns) at a temporal resolution of 1.5 ns, [3, 16, 17]. In particular, the PROES measurements (ns-scale) were performed at different phase positions of the fluctuating optical emission (ms-scale) in the plasma instability.

2.2 Particle-in-Cell and fluid model calculation

The 1d3v Particle-in-Cell method in combination with Monte-Carlo collisions (PIC-MCC) was developed [11] for the simulation of the charged particles distribution functions and their fluxes to the electrode in oxygen capacitive rf discharges. It is a reduced model because, out of up to 75 listed reaction and scattering processes which potentially affect the properties of the discharge, only 20 are included in the model. These 20 are the ones with the largest cross sections, representing the most important atomic and molecular processes in the oxygen plasma. Whereby, the electrons (e) and the negative and positive ions (O^-, O_2^+) are completely calculated 1d axially and 3d velocity resolved. Although the simulation system is actually three dimensional, the discharge behavior is assumed to be one dimensional along the axis of a symmetric rf discharge. This is supported by the fact that the electrode diameter is larger than the electrode spacing of 4.5 cm used in the simulation and that the radial dependence of the plasma parameters close to the symmetry axis can be neglected. Disregarding the electric asymmetry between the powered and the grounded electrode in the experiment, this interesting part of the discharge can be simulated by a planar, one-dimensional model, [3].

Furthermore, the numerical fluid model calculation was performed for a symmetric discharge basing on two circular planar-parallel electrodes at a distance of 2.5 cm driven by a sinusoidal voltage $V(t) = V_0 \sin(2\pi f t)$ with $f = 1/T = 13.56$ MHz and voltage amplitudes V_0 between 100 and 1000 V. Assuming radial symmetry of the rf plasma, a spatially one-dimensional description has been employed to characterize the axial behavior of the plasma between the electrodes. In the framework of the fluid model the time- and space-dependent balance equations of 17 heavy particle species, the electron component and the mean electron energy have been solved coupled with Poisson's equation for the determination of the electric field. The fluxes of particles and electron energy are treated in drift-diffusion approximation, where, in particular, the consistent diffusion coefficient and mobility of the electron transport have been used [18]. The general procedure for solving the coupled set of equations is similar to that described in [12]. The reaction kinetic model is based on the data reported in [19–21]. It distinguishes the neutral species $O_2(X^3\Sigma_g^-)$, $O_2(X, v > 0)$, $O_2(a^1\Delta_g)$, $O_2(b^1\Sigma_g^+)$, O_2^*, $O(^3P)$, $O(^1D)$, $O(^1S)$, O^*, $O_3(^1A_1)$ and O_3^*, the positive ions O_2^+, O^+ and O_3^+, the negative ions O_2^-, O^- and O_3^- as well as electrons. About 180 reactions are taken into account. In addition to various electron heavy-particle collision processes, collisional quenching and negative ion detachment in heavy particle collisions, charge exchange reactions, ion-ion recombination and radiative processes are included. In particular, the rate and transport coefficients of the electrons involved in the model have been obtained from the solution of the steady-state, spatially homogeneous Boltzmann equation for the electron velocity distribution function. This electron kinetic equation has been solved for given reduced electric field and atomic data by means of a generalized version of the multiterm technique [22] adapted to account for non-conservative electron collision processes. Then, the electron coefficients have been generated and used in the fluid model calculations. At the electrodes, flux boundary conditions have been employed for the heavy particles, electrons and mean electron energy density, which include terms due to drift and

Contrib. Plasma Phys. **52**, No. 10 (2012) / www.cpp-journal.org

random motion as well as the influence of partial reflection and secondary electron emission [23, 24]. Here, 0.3 was used for the reflection coefficient of electrons and neutral species, and the reflection coefficient of ions was set to 0.0005 [25]. Electrons leaving the cathode as a result of ion bombardment were assumed to have a mean energy of 2 eV at a secondary electron emission coefficient of 0.04 [26].

3 Results and discussion

3.1 Oxygen plasma at low and high electronegativity

The MWI provides line integrated electron densities along the Gaussian beam axis. To give an impression on the radial plasma density distribution in the used discharge configuration, the normalized radial profiles of the electron and positive ion density along the microwave optical axis are shown in figure 2 in the argon rf-plasma at 10 Pa, 10 W. The absolute electron and positive ion densities were determined using the Druyvesteyn [27] and the Sonin [28, 29] method, respectively. By use of the Sonin method an effective electron temperature was taken into calculation which was in the order of 2.4×10^4 K in the active plasma region. It is to note that the probe measurements were performed in a transition regime with Knudsen number ($Kn = \lambda / r_\mathrm{p}$) of 32 and 8 for electrons and positive ions, respectively, and the condition $\lambda_\mathrm{e} > \lambda_+ \gtrsim \lambda_\mathrm{D}$. The relation $\xi = r_\mathrm{p}/\lambda_\mathrm{D}$ changes from 0.6 at the discharge center ($r = 0$ mm) over 0.4 at the electrode edge ($r = 50$ mm) to 0.14 at the position $r = 100$ mm. Nevertheless, the normalized density profiles of electrons and positive ions in figure 1 are in good agreement within the measurement errors. The calculated absolute density values from probe measurements at the discharge axis ($r = 0$ mm, $a = 20$ mm) amount to $3.5 \times 10^{15}\,\mathrm{m}^{-3}$ and $2.5 \times 10^{15}\,\mathrm{m}^{-3}$ for electrons and positive ions, respectively. The lower ion density by the factor 1.4 is tolerable taking into account the assumption of an effective electron temperature and the influence of ion collisions in the sheath.

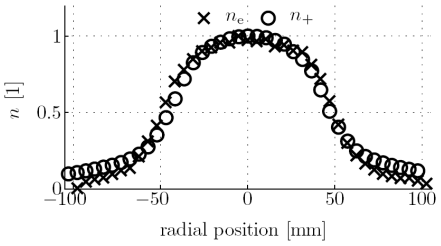

Fig. 2 Normalized radial plasma density distribution from probe measurements in argon rf plasma (10 Pa, 10 W) at the axial position $a = 20$ mm, using the electron density (×) and the positive ion density (○) calculated by the Druyvesteyn and Sonin method, respectively. The corresponding maximum densities on the axis amount to $3.5 \times 10^{15}\,\mathrm{m}^{-3}$ for electrons and $2.5 \times 10^{15}\,\mathrm{m}^{-3}$ for positive ions.

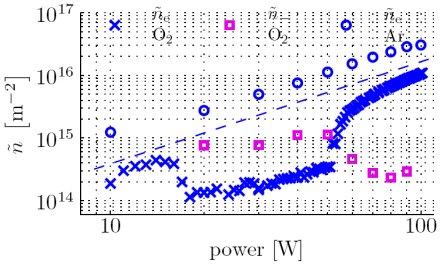

Fig. 3 Comparison of the line integrated electron density (MWI) in argon (○) and oxygen (×) plasma as well as the line integrated negative ion density (□) at 40 Pa total gas pressure and rf power variation.

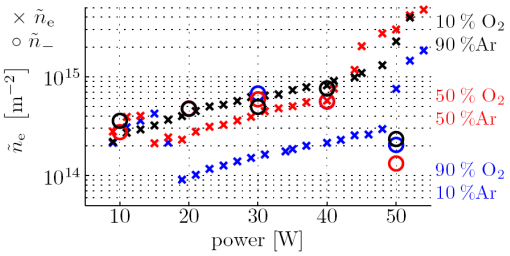

Fig. 4 Line integrated electron (×) and negative oxygen ion density (○) for different admixtures of argon and oxygen at 40 Pa total gas pressure and rf power variation.

The numerical calculation of the line integrated electron density from the radial electron density profile provides a value of about $3.5 \times 10^{14}\,\mathrm{m}^{-2}$. In comparison with the directly measured line integrated electron density of about $9.5 \times 10^{14}\,\mathrm{m}^{-2}$ from MWI, the probe measurement provides a value which is by a factor of 2.7 lower. Such differences in the electron density determination, comparing interferometry and electric probe diagnostics, were also reported in the literature [30–33]. Moreover, the Druyvesteyn method assumes an isotropic electron energy distribution function and the transition of the electrons towards the probe as collision-free. One reason

might be that for highly non-Maxwellian EEDF the cylindrical probe geometry has to be taken into account because of deviations in electron density calculation using the Druyvesteyn method [34].

In the following, the focus is directed on the electron density analysis by the MWI. The line integrated electron density in the electropositive gas argon rises continuously with increasing rf power and self-bias voltage, respectively, as expected, see figure 3. In contrast to argon, the line integrated electron density in pure oxygen offers an abnormal behavior, characterized by a lower electron density in total, and additionally by a significant electron density drop within a characteristic rf power range, see figure 3. It has to be noted, that the line integrated electron densities in oxygen are time averaged values. At low and high rf power, in particular for higher pressure, electron density fluctuations appear in the oxygen plasma, see section 3.4. Nevertheless, the regions of lower and higher line integrated electron density in figure 3 reveal different operation modes of the rf discharge. Using the MWI together with laser photodetachment at conditions for stable oxygen rf plasma, both the background and the laser detached additional electrons can be detected simultaneously. From the temporary electron density peak over the background electron density the amount of negative ions was determined. The range from 20 to 50 W with low line integrated electron density of about $2 \times 10^{14}\,\mathrm{m}^{-2}$ is combined with significantly higher line integrated negative oxygen ion density of up to $10^{15}\,\mathrm{m}^{-2}$. At rf power higher than 50 W a strong increase in the electron density is observed up to $10^{16}\,\mathrm{m}^{-2}$ with simultaneous decrease of the negative ion density, which is shown in figure 3. Unfortunately, the negative ion density could not be measured at rf power lower than 20 W due to plasma instabilities. Nevertheless, two operation modes exist at different electronegativity, the low electronegative mode ($\tilde{n}_-/\tilde{n}_\mathrm{e} \propto 0.01$) and high electronegative mode ($\tilde{n}_-/\tilde{n}_\mathrm{e} > 2$).

Using different mixtures of argon and oxygen a transient behavior of the line integrated electron density is observed (fig. 4). At relatively low oxygen admixture (10 %) in argon the electron density is already reduced and the discharge behaves like an electronegative plasma with an electronegativity of about 1, compare figures 3 and 4. With increasing oxygen admixture the two modes of electronegativity, observed in pure oxygen plasmas, are clearly visible in argon-oxygen rf plasma, see figure 4. In the case of 90 % oxygen admixture the negative ion density in the high electronegative mode (< 50 W) exceeds the electron density by the factor of about 4. At rf power higher than about 50 W the transition into the low electronegative mode takes place.

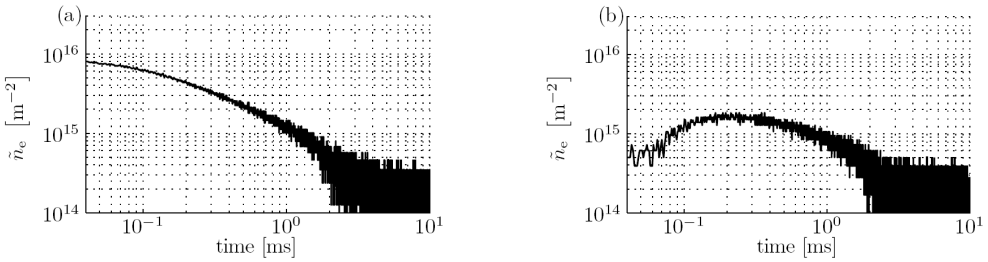

Fig. 5 Afterglow behavior of the line integrated electron density over time for (a) low electronegative mode (85 W) and (b) high electronegative mode (35 W) in oxygen rf plasma at 40 Pa.

Moreover, a different afterglow behavior of the electron density was observed for these modes, as shown for a 10 Hz (50 % duty cylce) pulsed oxygen rf plasma, see figure 5. At low electronegativity the electron density decreases immediately in the afterglow plasma like an electropositive gas, see figure 5(a). However, the afterglow behavior differs considerably in the high electronegative mode. In particular, an electron density increase is observed in the early afterglow, see figure 5(b). The maximum value can be up to six times larger than the mean on phase line integrated electron density. Obviously, this behavior is in connection with electron detachment from negative atomic oxygen ions due to collisions with atomic oxygen O as well as ground state $\mathrm{O}_2\left(\mathrm{X}^3\Sigma_\mathrm{g}^-\right)$ and metastable $\mathrm{O}_2\left(\mathrm{a}^1\Delta_\mathrm{g}\right)$ molecular oxygen, respectively. Especially, the electron detachment from negative ions due to collisions with metastable oxygen molecules is an important electron production channel [35].

3.2 The high electronegative mode of cc-rf oxygen plasma

In the special case of high electronegativity and short relaxation time of the additional produced electrons in the laser photodetachment experiment a simple 0d attachment-detachment model was applied to describe the

Contrib. Plasma Phys. **52**, No. 10 (2012) / www.cpp-journal.org

detachment signal analytically and to estimate the effective rate coefficients for dissociative electron attachment $\tilde{K}_\mathrm{a}$ and negative ion detachment $\tilde{K}_\mathrm{d}$, [2]. Here, two electron attachment reactions with ground and metastable state molecular oxygen as well as three negative ion detachment reactions with the corresponding molecular oxygen and the atomic oxygen are involved, respectively, (1)

$$\frac{\mathrm{d}n_\mathrm{e}}{\mathrm{d}t} = -\left(k_\mathrm{aX}\left(T_\mathrm{e}\right)n_\mathrm{X} + k_\mathrm{a\Delta}\left(T_\mathrm{e}\right)n_\Delta\right)n_\mathrm{e} + \left(k_\mathrm{dX}n_\mathrm{X} + k_\mathrm{d\Delta}n_\Delta + k_\mathrm{dO}n_\mathrm{O}\right)n_- = -\tilde{K}_\mathrm{a}n_\mathrm{e} + \tilde{K}_\mathrm{d}n_- \quad (1)$$

Using the steady state solution with $n_\mathrm{e}+n_- = n_{+,0} = const$ and the initial conditions $n_\mathrm{e}(t=0) = n_{\mathrm{e},0}+n_{-,0} = n_{+,0}$, the decay of the detachment signal is described by a single exponential decay function:

$$\Delta n_\mathrm{e}(t) = \left(n_\mathrm{e}(t) - n_{\mathrm{e},0}\right) = n_{-,0}\cdot\exp\left[-\left(\tilde{K}_\mathrm{a}+\tilde{K}_\mathrm{d}\right)\cdot t\right] \quad (2)$$

The effective attachment ($\tilde{K}_\mathrm{a}$) and detachment ($\tilde{K}_\mathrm{d}$) coefficients were evaluated from the measured decay time constant of the detachment signal τ and the line integrated electron and negative ion density expressed by the electronegativity $\alpha = n_-/n_\mathrm{e}$, see (3) and (4) and the experimental data in table 1.

$$\tilde{K}_\mathrm{a} = \frac{1}{\tau}\cdot\frac{1}{1+\frac{1}{\alpha}} \quad (3) \qquad \tilde{K}_\mathrm{d} = \frac{1}{\tau}\cdot\frac{1}{1+\alpha} \quad (4)$$

Table 1 Experimental data and results of the 0d attachment-detachment model for the high electronegative mode at 40 Pa. Effective rate coefficients $\tilde{K}_\mathrm{a}$ and $\tilde{K}_\mathrm{d}$ from experiment ($\tilde{n}_\mathrm{e}$, $\tilde{n}_-$, α, τ) and estimated molecular oxygen metastable (n_Δ) and ground state (n_X) density from model.

P [W]	$\tilde{n}_\mathrm{e}$ $[10^{14}\,\mathrm{m}^{-2}]$	$\tilde{n}_-$ $[10^{14}\,\mathrm{m}^{-2}]$	α [1]	τ $[10^{-6}\,\mathrm{s}]$	$\tilde{K}_\mathrm{a}$ $[10^{5}\,\mathrm{s}^{-1}]$	$\tilde{K}_\mathrm{d}$ $[10^{4}\,\mathrm{s}^{-1}]$	n_Δ $[10^{20}\,\mathrm{m}^{-3}]$	n_X $[10^{21}\,\mathrm{m}^{-3}]$
20	1.3±0.3	7.6±0.1	5.8±0.5	3.2±1	2.5±0.5	4.6±0.5	4.6±1	8.9±0.5
30	1.5±0.1	7.7±0.2	5.1±0.2	1.9±1	4.3±0.4	8.2±0.5	8.2±1	8.8±0.5
40	2.3±0.1	11.1±0.1	4.8±0.1	2.4±1	3.4±0.3	7.2±0.4	7.2±1	8.9±0.5
50	3.5±0.1	11.4±0.1	3.3±0.2	2.9±1	2.6±0.3	8.0±0.3	8.0±1	8.9±0.5

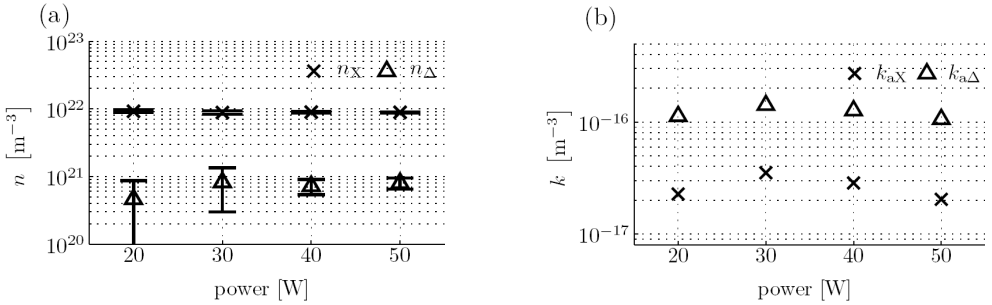

Fig. 6 (a) The experimentally determined density of ground state $\mathrm{O}_2\left(\mathrm{X}^3\Sigma_\mathrm{g}^-\right)$ (×) and metastable molecular oxygen $\mathrm{O}_2\left(\mathrm{a}^1\Delta_\mathrm{g}\right)$ (△) from the detachment reaction with metastable molecular oxygen and total particle density at 40 Pa and 300 K. (b) The attachment rate coefficient for ground state (×) and metastable molecular oxygen (△) over the rf power, evaluated from the experimentally determined effective rate coefficient.

In Küllig et al. [2] it is discussed that the main loss channel of negative ions is the detachment by molecular metastable oxygen $\mathrm{O}_2\left(\mathrm{a}^1\Delta_\mathrm{g}\right)$. The detachment of the negative ions by atomic oxygen can be neglected because of its low density in the range of only $10^{19}\,\mathrm{m}^{-3}$ measured by two photon laser-induced fluorescence spectroscopy [36–38] and calculated by FMC. For the given experimental conditions the negative ion detachment by ground state molecular oxygen can also be neglected because of the low rate coefficient [19]. Hence, the effective detachment coefficient $\tilde{K}_\mathrm{d}$ (table 1) can be used to estimate the metastable density n_Δ for different rf power values applied $\tilde{K}_\mathrm{d} = k_\mathrm{d\Delta}n_\Delta$ for total particle density at 40 Pa and 300 K. The estimated molecular ground

state $O_2\left(X^3\Sigma_g^-\right)$ and the metastable oxygen $O_2\left(a^1\Delta_g\right)$ density is shown in dependence on the rf power in figure 6(a). The relative molecular metastable density is in the order of $10\,\%$ of the molecular ground state density and is in good accordance to the literature [39, 40]. With the effective attachment rate coefficient $\tilde{K}_a$ it was calculated the attachment rate coefficients for the molecular ground state k_{aX} and the molecular metastable state $k_{a\Delta}$ by use of the estimated molecular ground state n_X and molecular metastable density n_Δ, see figure 6(b). The estimated attachment rate coefficients slightly decreases with increasing rf power due to the decrease in the electron temperature from 5 to 2 eV. These estimated values are also good in agreement with literature values [19,41]. Additionally, it shows that the dissociative attachment reaction with metastable molecular oxygen $O_2\left(a^1\Delta_g\right)$ is an important reaction channel to explain the effective attachment rate coefficient $\tilde{K}_a$.

The fluid model calculation at similar plasma processing parameter as the experiment (30 Pa, 1000 V peak-to-peak voltage) also reveals a high electronegative mode. Thereby, the temporally averaged axial profiles of charged particles are shown in figure 8(b). In the discharge center, the negative ion and electron density amounts to $3.36 \times 10^{16}\,m^{-3}$ as well as $1.27 \times 10^{15}\,m^{-3}$, respectively. Hence the electronegativity is of about 26. Using the estimated absolute electron and negative ion density from the experiment (30 Pa, 50 W, 900 V peak-to-peak voltage) the electronegativity amounts to about 4 which is significantly lower compared with the fluid model calculation. One reason may be the different discharge geometry in the experiment (asymmetric rf discharge) and the model calculation (symmetric rf discharge). Nevertheless, the dominance of the negative atomic oxygen ions in the plasma bulk is confirmed by the model. In particular, the opposite grounded electrode in the parallel plate electrode configuration in the symmetric model represents a specific boundary condition for charged as well as neutral particles, and influences the transport processes in axial and radial direction compared with the rather open geometry with one planar rf powered electrode in the asymmetric discharge. It is obvious that the density distribution in the bulk (discharge center) will be influenced. But, the physics in the rf boundary sheath and the plasma near the sheath edge should be adequately described. The development of a 2D model for the asymmetric rf discharge in oxygen will be a task for future investigations. Thereby, the existing 2D model for an argon rf discharge [42] has to be extended by inclusion of the specific elementary processes in oxygen.

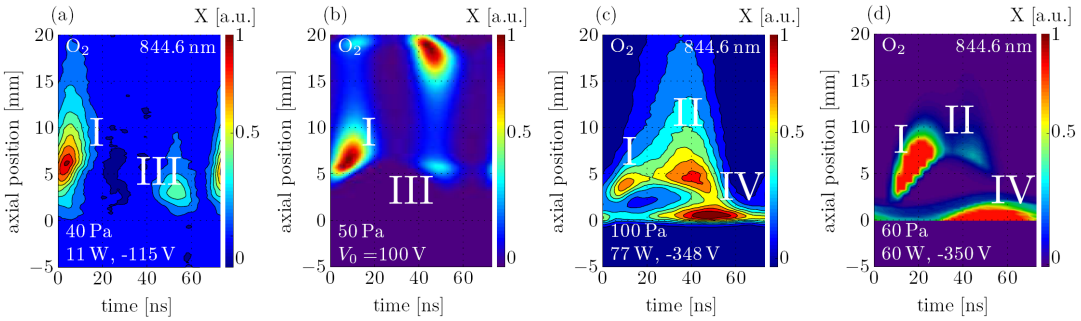

Fig. 7 Axially and rf phase resolved excitation rate X for the corresponding atomic oxygen emission at 844.6 nm in oxygen rf plasma [3, 16]: Agreement of significant excitation pattern between (a) PROES measurement and (b) FMC at low rf power, as well as (c) PROES measurement and (d) PIC-MCC simulation at high rf power, respectively. Excitation by electrons during rf sheath expansion (I), secondary electrons (II), electric field reversal during sheath collapse (III), and by heavy particle excitation (IV).

3.3 The transition into the low electronegative mode at higher rf power

The PROES was taken into account which provides information about the rf sheath dynamics and the electron heating mechanisms [3]. The spatio-temporally resolved excitation rate pattern of atomic oxygen at 844 nm, calculated from PROES data, reveals that the discharge operates in the alpha mode at high electronegativity, see figure 7(a). The pattern I has its origin in the usual electron heating during the sheath expansion phase. Generally, the alpha mode is characterized by higher electron temperature at rather low electron density. The higher electron temperature may be an explanation of the high content of negative ions due to the strongly increasing attachment rate coefficient with rising electron temperature [19, 41]. Furthermore, the excitation pattern III reveals another

important electron heating mechanism due to the electric field reversal, as shown in the experiment (fig. 7(a)) and in the FMC (figs. 7(b) and 8(a)). With increasing rf power the onset for the transition into the low electronegative mode is between 50 and 60 W at the pressure of 40 Pa, or at self-bias voltage more negative than −200 V, (fig. 3) [2]. Thereby, the line integrated electron density increases significantly from about 3×10^{14} to $5 \times 10^{15}\,\mathrm{m}^{-2}$, whereas the line integrated negative ion density decreases from about 10^{15} down to $3 \times 10^{14}\,\mathrm{m}^{-2}$.

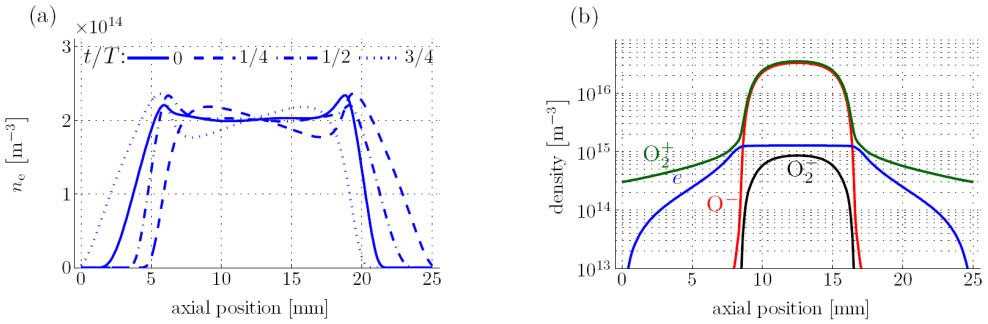

Fig. 8 Results of FMC are shown for (a) the axial electron density at four different rf phase positions at 50 Pa, $V_0 = 100$ V and (b) temporally averaged axial charge carrier densities at 30 Pa, $V_0 = 500$ V.

The electronegativity, calculated from the ratio between line integrated densities $\tilde{n}_-/\tilde{n}_\mathrm{e}$, decreases by the factor of 50. That means the oxygen discharge changes in the gamma mode [43] and secondary electrons are generated from the detachment of negative ions within the rf sheath ("pseudo-secondary electrons"), and the energetic heavy particle bombardment at the rf electrode (gamma process). These electrons are accelerated in the rf sheath and generate the excitation pattern II [3, 16], see figures 7(c) and (d). Additionally, the excitation pattern IV close to the powered electrode appears which is reproduced in the PIC-MCC simulation taking into account the dissociative excitation of atomic oxygen in collision between neutral oxygen molecules and energetic O_2^+ ions.

3.4 Plasma instabilities in oxygen cc-rf plasma

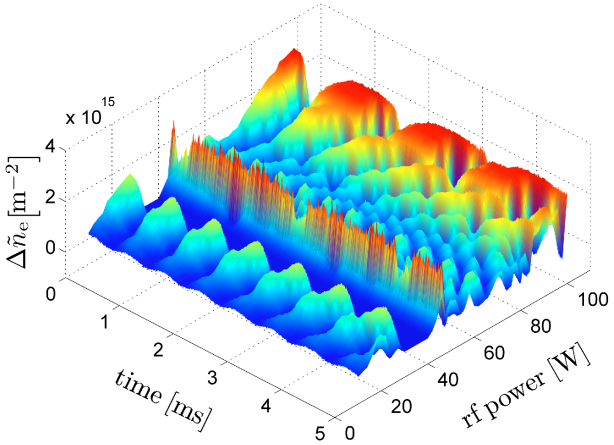

Fig. 9 Line integrated electron density fluctuations in dependence on rf power and time for process pressure of 60 Pa. The mean line integrated electron density is subtracted.

Plasma instabilities are found over wide field of processing parameters, which may be driven by attachment-induced ionization instabilities [5]. These instabilities could be measured as electron density fluctuations by microwave interferometry (figs. 9 and 10(a)), as fluctuations of the floating potential and ion saturation current by electric probe measurements, and as fluctuations in the excitation rate by temporally resolved optical emission spectroscopy (TROES). Generally, the instabilities appear within a specific rf power range at all investigated pressure values from 10 to 100 Pa. Above 60 Pa the rf oxygen discharge is dominated by instabilities. The

line integrated electron density fluctuations have peak-to-peak values from 0.2×10^{15} to $3.5 \times 10^{15}\,\mathrm{m}^{-2}$ and frequencies from 0.3 to 3 kHz, see figure 9. The start-up times of the instability are in the millisecond time scale measured in the plasma-on phase of a pulsed cc-rf discharge. In agreement with the MWI, the electron density fluctuations are also observed in the floating potential of probe measurements, shown in figure 10(b) for 20 Pa and 20 W.

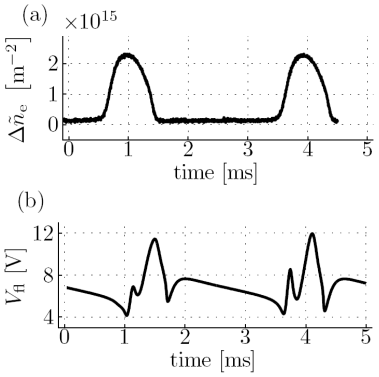

Fig. 10 Plasma instabilities are shown as temporal fluctuations of the line integrated electron density (a) and the radially averaged floating potential (b) at 20 Pa and 20 W (axial position $a = 20$ mm). The range between 1 and 2 ms in (b) is in relation to selected phase positions in fig. 11.

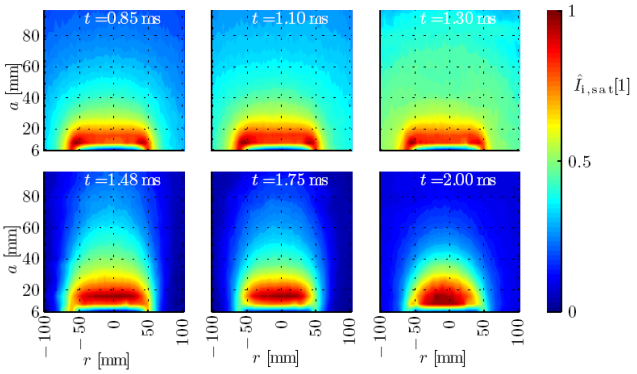

Fig. 11 Spatially resolved pattern of the normalized ion saturation current above the rf electrode at different phase positions of the floating potential fluctuation in figure 10(b) at 20 Pa and 20 W (a: axial and r: radial position).

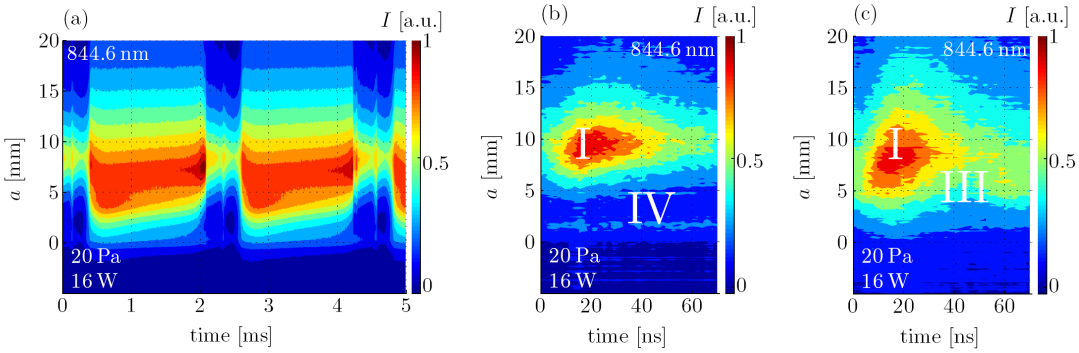

Fig. 12 TROES and PROES of atomic oxygen at 844.6 nm for an oxygen cc-rf discharge at 20 Pa and 16 W. (a) Temporally and axially resolved optical emission intensity over about two periods of the instability. Rf-phase and axially resolved optical emission intensity at the phase position of 1 ms (b) and 2.5 ms (c) within the instability.

The spatially (axial and radial) resolved ion saturation current is plotted in figure 11 at selected phase positions of the instability (cp. figures 10(a, b)). In all cases the relative current maximum is observed near the rf sheath edge as expected. But, significant differences are seen in the bulk plasma by comparison the more confined discharge before and after the electron density drop (fig. 10(a)) between about 1 and 1.5 ms with the rather extended plasma at other phase positions, see figure 11. Additionally, the temporally resolved optical emission spectroscopy (TROES) was applied to measure the fluctuation of the optical emission during the instability, see figure 12(a). Furthermore, as a highlight, it could be measured the rf phase resolved optical emission intensity (PROES, ns-scale) at selected phase positions of the instability, namely at 1 ms and 2.5 ms in figure 10(a), see figure 12. The optical emission patterns changes during the instability (cp. figures 12(b) and (c)). In particular, the

characteristic heavy particle emission pattern IV of atomic oxygen in front of the rf electrode appears (fig. 12(b)) when the electron density is high, and disappears when the electron density drops. Furthermore, at low electron density the emission pattern III appears which is connected with the electric field reversal, see figure 12(c). These effects are associated with fluctuations of the mean sheath potential and therefore with the change in the heating mechanisms and particle fluxes towards the powered electrode which have considerable influence on surface processes.

4 Conclusions and outlook

The low pressure capacitively coupled radio-frequency plasma (cc-rf plasma) in oxygen was systematically studied using high-end plasma diagnostics, the Gaussian beam microwave interferometry at 160 GHz and simultaneous laser photodetachment for the electron and negative ion density analysis in the bulk plasma, and the phase resolved optical emission spectroscopy (PROES) for detailed investigations of the rf sheath dynamics in asymmetric rf discharges. Furthermore, the Langmuir probe technique was involved in selected experiments to verify experimental results from microwave interferometry concerning the spatial plasma density distribution and the plasma instabilities. The Particle-in-Cell method combined with Monte-Carlo collisions (PIC-MCC) and Fluid Model Calculations (FMC) were successfully applied to study specific discharge modes of the cc-rf plasma in oxygen at different plasma processing parameters in close connection to the experiments. Thereby, a symmetric rf discharge was modeled, 1d spatially axial and full 3d in velocity.

The asymmetric cc-rf plasma in oxygen can operate at different discharge modes depending on the content of negative ions as well as the secondary electron emission. Two operation modes at different electronegativity (α) were found, the high electronegative mode with $\alpha > 2$ and the low electronegative mode with $\alpha < 0.01$. The stable high electronegative mode was also reproduced in the FMC. Both, the PROES and FMC reveal the electron heating due to the electric field reversal during the sheath collapse phase. The transition from the high into the low electronegative mode was found at rising rf power in connection with the alpha to gamma mode transition of the rf discharge. Thereby, PROES and PIC-MCC simulation have been shown the influence of "pseudo secondary electrons", produced by the detachment of negative ions in the rf sheath. The oxygen rf plasma is characterized by plasma instabilities over wide field of plasma processing parameters, that means fluctuations in the plasma parameters (e.g. electron density, ion saturation current, floating potential) and the optical emission intensity.

Further investigations are necessary to study in detail the small range in rf power observed for the transition between the two electronegative modes. In particular, the transition into the stable high electronegative mode coming from low rf power with plasma instabilities is an interesting topic. Thereby, the measurement of the negative ion density fluctuations is a real challenge. The laser photodetachment experiment has to be phase triggered with the instability. Furthermore, the fundamental investigation will be extended on the model system tetrafluoromethane. The different electron heating mechanisms as well as the electron and negative ion density will be studied more in detail by combined diagnostics using PROES, MWI and laser photodetachment. Thereby, the symmetric rf discharge at single and two frequency excitation is of interest concerning the electrical asymmetry effect and the recently discovered electron heating in drift and ambipolar electric fields [17].

Within the collaborative research center, the developed Gaussian beam MWI offers additionally the possibility of electron density diagnosis at other reactive plasmas and plasma sources (e.g. atmospheric pressure plasma jet, Schäfer et al. in this issue). Furthermore, the contribution of negative ions in barrier discharges at atmospheric pressure, containing oxygen, is of interest (a) in generation of secondary electrons by collisional detachment of negative ions produced at dielectric/metallic surfaces, Bronold et al. in this issue, or (b) in the spatio-temporal discharge development, Bogaczyk et al. in this issue.

Acknowledgements This work was supported by the Deutsche Forschungsgemeinschaft (DFG) in the framework of the Sonderforschungsbereich Transregio 24 "Fundamentals of Complex Plasmas", project B5 & B3.

References

[1] E. Stoffels, W.W. Stoffels, and G.M.W. Kroesen, Plasma Sources Sci. Technol. **10**, 311-317 (2001).
[2] C. Küllig, K. Dittmann, and J. Meichsner, Plasma Sources Sci. Technol. **19**, 065011 (2010).

[3] K. Dittmann, K. Matyash, S. Nemschokmichal, J. Meichsner, and R. Schneider, Contrib. Plasma Phys. **50**, 942-953 (2010).
[4] H.-M. Katsch, A. Goehlich T. Kawetzki, E. Quandt, and H.-F. Döbele, Appl. Phys. Lett. **75**, 2023-2025 (1999).
[5] C. Küllig, K. Dittmann and J. Meichsner, IEEE Trans. Plasma Science **39**, 2564 (2011).
[6] N.St.J. Braithwaite and J.E. Allen, J. Phys. D: Appl. Phys. **21**, 1733-1737 (1988).
[7] R.L.F. Boyd and J.B. Thompson, Proc. R. Soc. Lond. A **252**, 102 (1959).
[8] Ch. Hollenstein, W. Schwarzenbach, A.A. Howling, C Courteille, J.L. Dorier, and L. Sansonnens, J. Vac. Sci. Technol. A **14**, 535 (1996).
[9] U. Kogelschatz, Plasma Sources Sci. Technol. **11**, A1A6 (2002).
[10] G. Fridman, G. Friedman, A. Gutsol, A.B. Shekhter, V.N. Vasilets, and A. Fridman, Plasma Process. Polym. **5**, 503-533 (2008).
[11] F.X. Bronold, K. Matyash, D. Tskhakaya, R. Schneider, and H. Fehske, J. Phys. D: Applied Physics **40**, 6583 (2007).
[12] M.M. Becker, D. Loffhagen, and W. Schmidt, Comput. Phys. Commun. **180**, 1230-1241 (2009).
[13] W.L. Nighan and W.J. Wiegand, Phys. Rev. A **10**, 922-945 (1974).
[14] K. Dittmann, C. Küllig, and J. Meichsner, Plasma Sources Sci. Technol. **21**, 024001 (2012).
[15] U. Flenders, B.H. Nguyen Thi, K. Wiesemann, N.A. Khromov, and N.B. Kolokolov, Plasma Sources Sci. Technol. **5**, 61-69 (1996).
[16] K. Dittmann, D. Drozdov, B. Krames, and J. Meichsner, J. Phys. D: Appl. Phys. **40**, 6593-6600 (2007).
[17] J. Schulze, A. Derzsi, K. Dittmann, T. Hemke, J. Meichsner, and Z. Donko, Phys. Rev. Lett. **107**, 275001 (2011).
[18] G.J.M. Hagelaar and L.C. Pitchford, Plasma Sources Sci. Technol. **14**, 722-733 (2005).
[19] B. Eliasson and U. Kogelschatz, Basic data for modelling of electrical discharges in gases: oxygen, Tech. rep., Brown Boveri Forschungszentrum CH-5405 Baden, 1986.
[20] M. Hayashi, Electron collision cross sections, in: Plasma Material Science Handbook, edited by Japan Society for the Promotion of Science (Ohmsha, Ltd, Tokyo, 1992), pp. 748-766.
[21] A. V. Phelps, http://jilawww.colorado.edu/∼avp/.
[22] H. Leyh, D. Loffhagen, and R. Winkler, Comput. Phys. Commun. **113**, 33-48 (1998).
[23] G.J.M. Hagelaar, F.J. de Hoog G.M.W., and Kroesen, Phys. Rev. E **62**, 1452-1454 (2000).
[24] W.J.M. Brok, J. van Dijk, M.D. Bowden, J.J.A.M. van der Mullen, and G.M.W. Kroesen, J. Phys. D: Appl. Phys. **36**, 1967-1979 (2003).
[25] V.E. Golant, A.P. Zhilinsky, and I.E. Sakharov, Fundamentals of Plasma Physics (John Wiley, New York, 1980).
[26] J.H. Parker, Phys. Rev. **93**, 1148-1156 (1954).
[27] M.J. Druyvesteyn, Zeitschrift für Physik A Hadrons and Nuclei **64**, 781-798 (1930).
[28] A.A. Sonin, AIAA Journal **4**, 1588-1596 (1966).
[29] S. Klagge and M. Tichý, Czech. J. Phys. **35**, 988-1006 (1985).
[30] P.A. Miller, G.A. Hebner, K.E. Greenberg, and P.D. Pachan, J. Res. Natl. Inst. Stand. Technol. **100**, 427 (1995).
[31] C. Pargmann, S.V. Singh, and H. Soltwisch, Rev. Sci. Instrum. **76**, 113506 (2005).
[32] F. Mackel, P. Kempkes, H. Stein, J. Tenfelde, and H. Soltwisch, Meas. Sci. Technol. **22** (2011) 055705 (11pp), doi:10.1088/0957-0233/22/5/055705.
[33] C. Deline, B.E. Gilchrist, C. Dobson, J.E. Jones, and D.G. Chavers, Rev. Sci. Instrum. **78**, 113504 (2007); doi: 10.1063/1.2813885.
[34] A. El Saghir and S. Shannon, Plasma Sources Sci. Technol. **21**, 025003 (2012).
[35] C. Küllig, K. Dittmann, and J. Meichsner, Phys. Plasmas **19**, 073517 (2012).
[36] M. Geigl, S. Peters, O. Gabriel, B. Krames, and J. Meichsner, Contrib. Plasma Phys. **45**, 369-377 (2005).
[37] A. Goehlich, T. Kawetzki, and H.F. Döbele, J. Chem. Phys. **108**, 9362-9370 (1998).
[38] H.M. Katsch, A. Tewes, E. Quandt, A. Goehlich, T. Kawetzki, and H.F. Döbele, J. App. Phys. **88**, 6232-6238 (2000).
[39] S.G. Belostotsky, D.J. Economou, D.V. Lopaev, and T.V. Rakhimova, Plasma Sources Sci. Technol. **14**, 532-542 (2005).
[40] M. Shibata, N. Nakano, and T. Makabe, J. Appl. Phys. **80**, 6142-6147 (1996).
[41] J.T. Gudmundsson, A.M. Marakhtanov, K.K. Patel, V.P. Gopinath, and M.A. Lieberman, J. Phys. D: Appl. Phys. **33**, 1323-1331 (2000).
[42] R. Basner, F. Sigeneger, D. Loffhagen, G. Schubert, H. Fehske, and H. Kersten, New J. Phys. **11**, 013041 (2009).
[43] Ph. Belenguer and J.P. Boeuf, Phys. Rev. A **41**, 4447-4459 (1990).

Appendix A.

A.1. Derivation of the detachment ration

The ratio of the detached electrons to the total number of negative ions depends on the laser power [55, 72, 83] and can be deduced by.

$$\frac{\mathrm{d}\delta n_\mathrm{e}}{\mathrm{d}t} = \frac{\sigma I_\mathrm{l}(t)}{h\nu_\mathrm{l}} \left(n_{-0} - \delta n_\mathrm{e}\right) \tag{A.1}$$

I is the laser intensity, $h\nu_\mathrm{l}$ the photon energy of the laser and $\sigma = 6.4 \times 10^{-22}\,\mathrm{m}^2$ the photodetachment cross section [119, 120]. Moreover, it is $n_{-0} = \delta n_\mathrm{e} + n_-$ the steady state negative ion density, which is the sum of detached electrons δn_e and the remaining negative oxygen ions n_-. This differential equation (A.1) can be solved by introducing the following substitution:

$$\xi(t) = n_{-0} - \delta n_\mathrm{e} \tag{A.2}$$

$$\frac{\mathrm{d}\xi}{\mathrm{d}\delta n_\mathrm{e}} = -1 \tag{A.3}$$

$$\mathrm{d}\xi = -\mathrm{d}\delta n_\mathrm{e} \tag{A.4}$$

Hence, the differential equations (A.1) can be rewritten to and subsequently solved.

$$\begin{aligned}
\frac{\mathrm{d}\xi}{\xi} &= -\frac{\sigma I_\mathrm{l}(t)}{h\nu_\mathrm{l}}\mathrm{d}t \\
\int_{\xi_0}^{\xi} \frac{\mathrm{d}\xi}{\xi} &= -\frac{\sigma}{h\nu_\mathrm{l}} \int I_\mathrm{l}(t)\mathrm{d}t \\
\ln\frac{\xi}{\xi_0} &= -\frac{\sigma}{h\nu_\mathrm{l}} \int I_\mathrm{l}(t)\mathrm{d}t \\
\frac{\xi}{\xi_0} &= \exp\left(-\frac{\sigma}{h\nu_\mathrm{l}} \int I_\mathrm{l}(t)\mathrm{d}t\right)
\end{aligned} \tag{A.5}$$

The initial parameter ξ_0 has to be determined by the knowledge of that $\delta n_\mathrm{e} = 0$ at $t = 0$ just before the laser shot.

$$\begin{aligned}
\xi(t) &= n_{-0} - \delta n_\mathrm{e} \\
\xi(t=0) &= n_{-0}
\end{aligned} \tag{A.6}$$

Consequently, it can be (A.5) rewritten to:

$$\begin{aligned}
\frac{n_{-0} - \delta n_{\mathrm{e}}}{n_{-0}} &= \exp\left(-\frac{\sigma}{h\nu_{\mathrm{l}}}\int I_{\mathrm{l}}(t)\mathrm{d}t\right) \\
n_{-0} - \delta n_{\mathrm{e}} &= n_{-0}\cdot\exp\left(-\frac{\sigma}{h\nu_{\mathrm{l}}}\int I_{\mathrm{l}}(t)\mathrm{d}t\right) \\
\delta n_{\mathrm{e}} &= n_{-0} - n_{-0}\cdot\exp\left(-\frac{\sigma}{h\nu_{\mathrm{l}}}\int I_{\mathrm{l}}(t)\mathrm{d}t\right) \\
\delta n_{\mathrm{e}} &= n_{-0}\left[1 - \exp\left(-\frac{\sigma}{h\nu_{\mathrm{l}}}\int I_{\mathrm{l}}(t)\mathrm{d}t\right)\right] \\
\frac{\delta n_{\mathrm{e}}}{n_{-0}} &= 1 - \exp\left(-\frac{\sigma}{h\nu_{\mathrm{l}}}\int I_{\mathrm{l}}(t)\mathrm{d}t\right)
\end{aligned} \tag{A.7}$$

The equation (A.7) defines the ratio of the detached electrons to the total amount of the negative ions and can be estimated for a short-pulsed laser system, by using $\int I_{\mathrm{l}}\ \mathrm{d}t \equiv E_{\mathrm{l}}/A_{\mathrm{l}}$ where E is the laser energy and $A_{\mathrm{l}} = \pi R_{\mathrm{l}}^2$ the laser beam cross section.

$$\frac{\delta n_{\mathrm{e}}}{n_{-0}} = \left[1 - \exp\left(-\frac{\sigma}{h\nu_{\mathrm{l}}}\frac{E_{\mathrm{l}}}{A_{\mathrm{l}}}\right)\right] \tag{A.8}$$

Bibliography

[1] M Schmidt R Schneider J Meichsner and H-E Wagner. *Nonthermal Plasma Chemistry and Physics*. CRC Press Taylor & Francis Group, LLC, 2012.

[2] P Chabert and N St J Braithwaite. *Physics of Radio-Frequency Plasmas*. Cambridge University Press, New York, 2011.

[3] M A Lieberman and A J Lichtenberg. *Principles of Plasma Discharges and Materials Processing*. New York: Wiley, 2005.

[4] B G Heil, U Czarnetzki, R P Brinkmann and T Mussenbrock. On the possibility of making a geometrically symmetric RF-CCP discharge electrically asymmetric. *J. Phys. D: Appl. Phys.*, **41**:165202, 2008.

[5] Z Donko, J Schulze, B G Heil and U Czarnetzki. PIC simulations of the separate control of ion flux and energy in CCRF discharges via the electrical asymmetry effect. *J. Phys. D: Appl. Phys.*, **42**:025205, 2009.

[6] J Schulze, E Schüngel and U Czarnetzki. The electrical asymmetry effect in capacitively coupled radio frequency discharges measurements of dc self bias, ion energy and ion flux. *J. Phys. D: Appl. Phys.*, **42**:092005, 2009.

[7] H Sabadil, S Klagge and M Kammeyer. Langmuir Probe Measurements of Axial Variation of Plasma Parameters in 27.1 MHz rf Oxygen Planar Discharges. *Plasma Chem. Plasma Process*, **8**(4):425–444, 1988.

[8] D A Carl, D W Hess and M A Lieberman. Kinetics of photoresist etching in an electron cyclotron resonance plasma. *J. Vac. Sci. Technol.*, **68**:2924, 1990.

[9] M Kitajima, H Kuroki, H Shinno and K G Nakamura. Growth of silicon oxide on silicon in the thin film region in an oxygen plasma. *Solid State Commun.*, **83**:385, 1992.

[10] U Kogelschatz. Advanced Ozone Generation. *Process Technologies for Water Treatment*, pages 87–120, 1988.

[11] U Kogelschatz. Dielectric-barrier Discharges: Their History, Discharge Physics, and Industrial Applications. *Process Technologies for Water Treatment*, **23**:1–46, 2003.

[12] K H Becker, U Kogelschatz, K H Schoenbach and R J Barker. *Non-Equilibrium Air Plasmas at Atmospheric Pressure*. Institute of Physics Publishing, Bristol and Philadelphia, 2005.

[13] U Kogelschatz. Industrial innovation based on fundamental physics. *Plasma Sources Sci. Technol.*, **11**:A1–A6, 2002.

[14] E Stoffels, W W Stoffels and G M W Kroesen. Plasma chemistry and surface processes of negative ions. *Plasma Sources Sci. Technol.*, **10**:311–317, 2001.

[15] K Dittmann, D Drozdov, B Krames and J Meichsner. Radio-frequency discharges in oxygen: II. Spatio-temporally resolved optical emission pattern. *J. Phys. D: Appl. Phys.*, **40**:6593–6600, 2007.

[16] S Nemschokmichal, K Dittmann and J Meichsner. Spatial and Phase Resolved Optical Emission Pattern in Capacitively Coupled Radio-Frequency Plasmas. *IEEE Transactions on Plasma Science*, **36**:1360, 2008.

[17] K Dittmann. *Detailed Investigations of the Sheath Dynamics and Elementary Processes in Capacitively Coupled RF Plasmas*. PhD thesis, Institute of Physics, Ernst-Moritz-Arndt University of Greifswald, 2009.

[18] K Dittmann, K Matyash, S Nemschokmichal, J Meichsner and R Schneider. Excitation Mechanisms and Sheath Dynamics in Capacitively Coupled Radio-Frequency Oxygen Plasmas. *Contrib. Plasma Phys.*, **50**:942–953, 2010.

[19] H M Mott-Smith and I Langmuir. The theory of collectors in gaseous discharges. *Phys. Rev.*, **28**:727–763, 1926.

[20] V I Demidov, S V Ratynskaia and K Rypdal. Electric probes for plasmas: The link between theory and instrument. *Rev. Sci. Instrum.*, **73**:3409, 2002.

[21] S Arndt, F Sigeneger, H Testrich and C Brandt. Self-Consistent Analysis of the Spatial Relaxation of a Disturbed Neon Glow Discharge. *Plasma Chemistry and Plasma Processing*, **25**:567–594, 2005.

[22] C Brandt, H Testrich, R Kozakov and C Wilke. Investigation of the disturbance of a Langmuir probe and its influence on measurement results. *Rev. Sci. Instrum.*, **77**:023504, 2006.

[23] M B Hopkins and W G Graham. Langmuir probe technique for plasma parameter measurement in a medium density discharge. *Rev. Sci. Instrum.*, **57**:2210–2217, 1986.

[24] V A Godyak, R B Piejak and B M Alexandrovich. Measurements of electron energy distribution in low-pressure RF discharges. *Plasma Sources Sci. Technol.*, **1**:36–58, 1992.

[25] V A Godyak, R B Piejak and B M Alexandrovich. Probe diagnostics of non-Maxwellian plasmas. *J. Appl. Phys.*, **73**:3657–3663, 1993.

[26] S Klagge. Sondendiagnostik, Weiterbildungskurs Plasmaphysik. *Vorlesungsmanuskript Sektion Physik/Elektronik, Universität Greifswald*, 1993.

[27] G Wehner and G Medicus. Reliability of Probe Measurements in Hot Cathode Gas Diodes. *J. Appl. Phys.*, **23**:1035, 1952.

[28] T L Thomas and E L Battle. Effects of Contamination on Langmuir Probe Measurements in Glow Discharge Plasmas. *J. Appl. Phys.*, **41**:3428, 1970.

[29] R A Olson and D R Nordlund. Automatic Plotting of Langmuir Probe Susceptance and Conductance Voltage Curves. *J. Appl. Phys.*, **43**:2780, 1972.

[30] U Buddemeier. *Experimentelle Untersuchung einer kapazitiv gekoppelten HF-Entladung in Sauerstoff*. PhD thesis, Ruhr-Universität Bochum, 1997.

[31] H Amemiya, N Yasuda and M Endou. Negative Ion-Containing Plasma in Parallel-Plate Radio-Frequency Discharge Oxygen. *Plasma Chem. Plasma Process*, **14**:209–227, 1994.

[32] A Kono. Negative ions in processing plasmas and their effect on the plasma structure. *Applied Surface Science*, **192**:115–134, 2002.

[33] H Kersten, R Wiese, G Thieme, M Fröhlich, A Kopitov, D Bojic, F Scholze, H Neumann, M Quaas, H Wulff and R Hippler. Examples for application and diagnostics in plasmapowder interaction. *New Journal of Physics*, **5**:93.1–93.15, 2003.

[34] R L Merlino and S-H Kim. Charge neutralization of dust particles in a plasma with negative ions. *Appl. Phys. Lett.*, **89**:091501, 2006.

[35] M Bacal. Volume Production of Hydrogen Negative Ions. *Nucl. Instrum. Methods Phys. Res. B*, **37-38**:29–32, 1989.

[36] G W Hamilton and M Bacal. Physics and applications of charged particle beam sources. *IEEE Trans. Plasma Sci.*, **19**:1143, 1991.

[37] R Gutser, D Wünderlich, U Fantz and the NNBI-Team. Transport of negative hydrogen and deuterium ions in RF-driven ion sources. *Plasma Phys. Control. Fusion*, **52**:045017, 2010.

[38] A Descoeudres, L Sansonnens and Ch Hollenstein. Attachment-induced ionization instability in electronegative capacitive RF discharge. *Plasma Sources Sci. Technol.*, **12**:152–157, 2003.

[39] H-M Katsch, A Goehlich T Kawetzki, E Quandt and H-F Döbele. Attachment-induced ionization instability of a radio frequency excited discharge in oxygen. *Appl. Phys. Lett.*, **75**:2023–2025, 1999.

[40] W L Nighan and W J Wiegand. Influence of negative-ion processes on steady-state properties and striations in molecular gas discharges. *Physical Review A*, **10**:922–945, 1974.

[41] M A Lieberman, A J Lichtenberg and A M Marakhtanov. Instabilities in low-pressure inductive discharge with attaching gases. *Appl. Phys. Lett.*, **75**:3617–3619, 1999.

[42] P Chabert, A J Lichtenberg, M A Lieberman and A M Marakhtanov. Instabilities in low-pressure electronegative inductive discharges. *Plasma Sources Sci. Technol.*, **10**:478–489, 2001.

[43] C S Corr, P G Steen and W G Graham. Instabilities in an inductively coupled oxygen plasma. *Plasma Sources Sci. Technol.*, **12**:265–272, 2003.

[44] B Bruhn, A Richter and B May. On the stability of a dc-driven oxygen discharge in cylindrical geometry. *Phys. Plasmas*, **15**:053505, 2008.

[45] C Küllig, K Dittmann and J Meichsner. Electron Density Oscillations in CC-RF Oxygen Plasma Investigated by Gaussian Beam Microwave Interferometry. *IEEE Trans. Plasma Science*, **39**:2564, 2011.

[46] C Küllig, K Dittmann and J Meichsner. A novel approach for negative ion analysis using 160 GHz microwave interferometry and laser photodetachment in oxygen cc-rf plasmas. *Plasma Sources Sci. Technol.*, **19**:065011, 2010.

[47] R L F Boyd and J B Thompson. The operation of Langmuir probes in electronegative plasmas. *Proc. R. Soc. Lond. A*, **252**:102–119, 1959.

[48] N St J Braithwaite and J E Allen. Boundaries and probes in electronegative plasmas. *J. Phys. D: Appl. Phys.*, **21**:1733–1737, 1988.

[49] N Plihon, C S Corr, P Chabert and J-L Raimbault. Periodic formation and propagation of double layers in the expanding chamber of an inductive discharge operating in Ar/SF_6 mixtures. *J. Appl. Phys.*, **98**:023306, 2005.

[50] N Plihon, P Chabert and C S Corr. Experimental investigation of double layers in expanding plasmas. *Phys. Plasmas*, **14**:013506, 2007.

[51] A Meige, N Plihon, G J M Hagelaar, J-P Boeuf, P Chabert and R W Boswell. Propagating double layers in electronegative plasmas. *Phys. Plasmas*, **14**:053508, 2007.

[52] M Zeuner, J Meichsner and J A Rees. High energy negative ions in a radio-frequency discharge. *J. Appl. Phys.*, **79**:9379, 1996.

[53] Ch Hollenstein, W Schwarzenbach, A A Howling, C Courteille, J L Dorier, and L Sansonnens. Anionic clusters in dusty hydrocarbon and silane plasmas. *J. Vac. Sci. Technol. A*, **14**:535–539, 1996.

[54] M Bacal, G W Hamilton, A M Bruneteau, H J Doucet, and J Taillet. Measurement of H^- density in plasma by photodetachment. *Rev. Sci. Instrum.*, **50**:719–721, 1979.

[55] K E Greenberg, G A Hebner and J T Verdeyen. Negative ion densities in NF_3 discharges. *Appl. Phys. Lett.*, **44**:299–300, 1984.

[56] P Devynck, J Auvray, M Bacal, P Berlemont, J Bruneteau, R Leroy and R A Stern. Photodetachment technique for measuring H^- velocities in a hydrogen plasma. *Rev. Sci. Instrum.*, **60**:2873–2878, 1989.

[57] H Amemiya. Plasmas with negative ions-probe measurements and charge equilibrium. *J. Phys. D: Appl. Phys.*, **23**:999–1014, 1990.

[58] M B Hopkins, M Bacal and W G Graham. Enhanced volume production of negative ions in the post discharge of a multicusp hydrogen discharge. *J. Appl. Phys.*, **70**:2009–2014, 1991.

[59] M Bacal. Plasma diagnostics in negative ion sources. *Plasma Sources Sci. Technol.*, **2**:190–197, 1993.

[60] E Stoffels, W W Stoffels, D Vender, M Kando, G M W Kroesen and F J de Hoog. Negative ions in a radio-frequency oxygen plasma. *Physical Review E*, **51**(3):2425–2435, 1995.

[61] F El Balghiti-Sube, F G Baksht and M Bacal. Photodetachment diagnostics of plasma with a high n_-/n_e ratio. *Rev. Sci. Instrum.*, **67**:2221–2227, 1996.

[62] M Nishiura, M Sasao and M Bacal. H^- laser photodetachment at 1064, 532, and 355 nm in plasma. *J. Appl. Phys.*, **83**:2944, 1998.

[63] D Hayashi and K Kadota. Measurements of negative ion density in high-density oxygen plasmas by probe-assisted laser photodetachment. *J. Appl. Phys.*, **83**:703, 1998.

[64] E Quandt, H F Döbele and W G Graham. Measurements of negative ion densities by absorption spectroscopy. *Appl. Phys. Lett.*, **72**:2394, 1998.

[65] T Mosbach, H-M Katsch and H F Döbele. Temporal behaviour of the H-minus density in a pulsed multipole discharge investigated by the photodetachment technique. *Plasma Sources Sci. Technol.*, **7**:75–81, 1998.

[66] W Ding, D L McCorkle and L A Pinnaduwage. Enhanced formation of negative ions by electron attachment to highly excited molecules in a flowing afterglow plasma. *J. Appl. Phys.*, **84**:3051–3058, 1998.

[67] M Bacal. Photodetachment diagnostic techniques for measuring negative ion densities and temperatures in plasmas. *Rev. Sci. Instrum.*, **71**:3981–4006, 2000.

[68] H M Katsch, T Sturm, E Quandt and H F Döbele. Negative Ions and the role of metastable molecules in a capacitively coupled radiofrequency excited discharge in oxygen. *Plasma Sources Sci. Technol.*, **9**:323–330, 2000.

[69] M Shindo, S Uchino, R Ichiki, S Yoshimura and Y Kawai. Measurements of the negative ion density in SF6/Ar plasma using a plane electrostatic probe. *Rev. Sci. Instrum.*, **72**:2288–2293, 2001.

[70] F M Dias, E Tatarova, H Crespo and C M Ferreira. A laser photodetachment technique for the measurement of H^- in a high frequency traveling wave discharge. *Rev. Sci. Instrum.*, **72**:1680–1687, 2001.

[71] T K Popov and S V Gateva. Second derivative Langmuir probe measurements of negative oxygen ion concentration taking into account the plasma depletion caused by negative ion sink on the probe surface. *Plasma Sources Sci. Technol.*, **10**:614–620, 2001.

[72] J A Wagner and H-M Katsch. Negative oxygen ions in a pulsed RF-discharge with inductive coupling in mixtures of noble gases and oxygen. *Plasma Sources Sci. Technol.*, **15**:156–169, 2006.

[73] S Christ-Koch, U Fantz, M Berger and NNBI Team. Laser photodetachment on a high power, low pressure rf-driven negative hydrogen ion source. *Plasma Sources Sci. Technol.*, **18**:025003, 2009.

[74] P Svarnas, B M Annaratone, S Béchu, J Pelletier and M Bacal. Study of hydrogen plasma in the negative-ion extraction region. *Plasma Sources Sci. Technol.*, **18**:045010, 2009.

[75] Z Kiss'ovski, S Kolev, S Müller, T Paunska, A Shivarova and T Tsankov. Expanding hydrogen plasmas: photodetachmenttechnique diagnostics. *Plasma Phys. Control. Fusion*, **51**:015007, 2009.

[76] S D You, R Dodd, A Edwards and J W Bradley. A study of the plasma electronegativity in an argonoxygen pulsed-dc sputter magnetron. *J. Phys. D: Appl. Phys.*, **43**:505205, 2010.

[77] R Dodd, S-D You, P M Bryant and J W Bradley. Negative ion density measurements in a reactive dc magnetron using the eclipse photodetachment method. *Plasma Sources Sci. Technol.*, **19**:015021, 2010.

[78] C S Corr, S Gomez and W G Graham. Discharge kinetics of inductively coupled oxygen plasmas: experiment and model. *Plasma Sources Sci. Technol.*, **21**:055024, 2012.

[79] S Kajita, S Kado, T Shikama, B Xiao and S Tanaka. Effect of Probe Surface Ablation on Laser Photodetachment Signals. *Contrib. Plasma Phys.*, **44**:607–612, 2004.

[80] S Kajita, S Kado and S Tanaka. Eclipse laser photodetachment method for avoiding probe surface ablation in negative ion measurement. *Plasma Sources Sci. Technol.*, **14**:566–575, 2005.

[81] M Bacal, A M Bruneteau and M Nachman. Electron collection radius of an electrostatic probe immersed in a low-pressure plasma. *J. Phys. Lett.*, **42**:5–7, 1981.

[82] C E Gaebe, T R Hayes and R A Gottscho. Effect of photodetachment on a radio-frequency discharge through BCl_3. *Phys. Rev. A*, **35**:2993–3000, 1987.

[83] C Schiffer and J Uhlenbusch. Negative-oxygen-ion detection by a crossed-beam photodetachment technique. *Plasma Sources Sci. Technol.*, **4**:345–352, 1995.

[84] D Vender, W W Stoffels, E Stoffels, G M W Kroesen and F J de Hoog. Charged-species profiles in electronegative radio-frequency plasmas. *Physical Review E*, **51**:2436–2444, 1995.

[85] J Conway, N Sirse, S K Karkari and M M Turner. Using the resonance hairpin probe and pulsed photodetachment technique as a diagnostic for negative ions in oxygen plasma. *Plasma Sources Sci. Technol.*, **19**:065002, 2010.

[86] V Schulz-von der Gathen, J Röpcke, T Gans, M Käning, C Lukas and H F Döbele. Diagnostic studies of species concentrations in a capacitively coupled RF plasma containing CH_4-H_2-Ar. *Plasma Sources Sci. Technol.*, **10**:530–539, 2001.

[87] D Véron. Submillimeter interferometry of high-density plasmas. *Infrared and millimeter waves*, **2**:67–135, 1979.

[88] H K Park. A new asymmetric Abel-inversion method for plasma interferometry in tokamaks. *Plasma Phys. Control. Fusion*, **31**:2035, 1989.

[89] P C Efthimion, G Taylor, W Ernst, M Goldman, M McCarthy and H Anderson. 1-millimeter wave interferometer for the measurement of line integral electron density on TFTR. *Rev. Sci. Instrum.*, **56**:908–910, 1985.

[90] J A Fessey, C W Gowers, C A J Hugenholtz and K Slavin. Plasma electron density measurements from the JET 2 mm wave interferometer. *J. Phys. E*, **20**:169–174, 1987.

[91] H J Hartfuss, T Geist and M Hirsch. Heterodyne methods in millimetre wave plasma diagnostics with applications to ECE, interferometry and reflectometry. *Plasma Phys. Control. Fusion*, **39**:1693, 1997.

[92] S E Sharapov, B Alper, J Fessey, N C Hawkes, N P Young, R Nazikian, G J Kramer, D N Borba, S. Hacquin, E De La Luna, S D Pinches, J Rapp, D Testa and JET-EFDA. Monitoring Alfvén Cascades with Interferometry on the JET Tokamak. *Phys. Rev. Lett.*, **93**:165001, 2004.

[93] M A Cappelli, N Gascon, W A Hargus Jr. Millimetre wave plasma interferometry in the near field of a Hall plasma accelerator. *J. Phys. D: Appl. Phys.*, **39**:4582–4588, 2006.

[94] J Lee and M A Cappelli. An analysis of millimetre-wave interferometry on Hall thruster plumes by finite difference time domain simulations. *J. Phys. D: Appl. Phys.*, **41**:185205 (5pp), 2008.

[95] N Niemöller, V Schulz-von der Gathen, A Stampa and H F Döbele. A quasi-optical 1 mm microwave heterodyne interferometer for plasma diagnostics using a frequency-tripled Gunn oscillator. *Plasma Sources Sci. Technol.*, **6**:478–483, 1997.

[96] Ch Lukas, M Müller, V Schulz-von der Gathen and H F Döbele. Spatially resolved electron density distribution in an RF excited parallel plate plasma reactor by 1 mm microwave interferometry. *Plasma Sources Sci. Technol.*, **8**:94–99, 1999.

[97] M Krämer, B Clarenbach and W Kaiser. A 1 mm interferometer for time and space resolved electron density measurements on pulsed plasmas. *Plasma Sources Sci. Technol.*, **15**:332–337, 2006.

[98] G A Hebner, J T Verdeyen and M J Kushner. An experimental study of a parallel plate radio frequency discharge: Measurements of the radiation temperature and electron density. *J. Appl. Phys.*, **63**(7):2226–2236, 1988.

[99] K E Greenberg and G A Hebner. Electron and metastable densities in parallel-plate radio-frequency discharges. *J. Appl. Phys.*, **73**(12):8126–8133, 1993.

[100] L J Overzet. Microwave diagnostic results form the gaseous electronics conference RF reference cell. *J. Res. Natl. Inst. Stand. Technol.*, **100**:401–414, 1995.

[101] W F Cummins. A Stabilized 70 Gc Plasma Interferometer. *Rev. Sci. Instrum.*, **41**:234–237, 1970.

[102] A Pearson, G A Campbell, C W Domier and P C Efthimion. A Microwave Interferometer for Density Measurement and Stabilization in Process Plasmas. *Mater. Res. Soc. Symp. Proc.*, **117**:311, 1988.

[103] M Haverlag, A Kono, D Passchier, G M W Kroesen, W J Goedheer and FJ de Hoog. Measurements of negative ion densities in 13.56-MHz rf plasmas of CF_4, C_2F_6, CHF_3, and C_3F_8 using microwave resonance and the photodetachment effect. *J. Appl. Phys.*, **70**(7):3472–3480, 1991.

[104] A Kono, M Endo, K Ohata, S Kishimoto and T Goto. Charged particle densities and kinetics in a radio-frequency SF_6 plasma. *J. Appl. Phys.*, **76**:7221–7230, 1994.

[105] G A Hebner. Negative ion density in inductively coupled chlorine plasmas. *J. Vac. Sci. Technol. A*, **14**:2158–2162, 1996.

[106] G A Hebner, M G Blain, T W Hamilton, C A Nichols and R L Jarecki. Surface dependent electron and negative ion density in inductively coupled discharges. *J. Vac. Sci. Technol. A*, **17**:3172–3178, 1999.

[107] S Rauf, P L G Ventzek, I C Abraham, G A Hebner and J R Woodworth. Charged species dynamics in an inductively coupled Ar/SF_6 plasma discharge. *J. Appl. Phys.*, **92**(12):6998–7007, 2002.

[108] G A Hebner and I C Abraham. Characterization of electron and negative ion densities in fluorocarbon containing inductively driven plasmas. *J. Appl. Phys.*, **90**(10):4929–4937, 2001.

[109] Z Chen, V M Donnelly and D J Economou. Measurement of electron temperatures and electron energy distribution functions in dual frequency capacitively coupled CF_4/O_2 plasmas using trace rare gases optical emission spectroscopy. *J. Vac. Sci. Technol. A*, **27**:1159–1165, 2009.

[110] H Park, S J You, and W Choe. Correlation between excitation temperature and electron temperature with two groups of electron energy distributions. *Phys. Plasmas*, **17**:103501, 2010.

[111] M A Heald and C B Wharton. *Plasma Diagnostics with microwaves.* John Wiley & Sons Inc., New York • London • Sydney, 1965.

[112] A Brockhaus, G F Leu, V Selenin, Kh Tarnev and J Engemann. Electron release in the afterglow of a pulsed inductively-coupled radiofrequency oxygen plasma. *Plasma Sources Sci. Technol.*, **15**:171–177, 2006.

[113] G Neumann, U Bänziger, M Kammeyer and M Lange. Plasma-density measurements by microwave interferometry and Langmuir probes in an rf discharge. *Rev. Sci. Instrum.*, **64**:19–25, 1993.

[114] E E Scime, R F Boivin J L Kline and M M Balkey. Microwave interferometer for steadystate plasmas. *Rev. Sci. Instrum.*, **72**:1672–1676, 2001.

[115] L J Overzet and M B Hopkins. Comparison of electron-density measuremets made using a Langmuir probe and microwave interfermoter in the Gaseous Electronics Conference reference reactor. *J. Appl. Phys.*, **74**(7):4323–4330, 1993.

[116] P F Goldsmith. *Quasioptical Systems.* Wiley-IEEE Press, 1998.

[117] M Shibata, N Nakano and T Makabe. The effect of laser-induced photodetachment in O_2 rf discharges. *J. Phys. D: Appl. Phys.*, **30**:1219–1224, 1997.

[118] T Suzuki and T Kasuya. Optogalvanic study of photodetachment of O^- near threshold. *Phys. Rev. A*, **36**(5):2129–2133, 1987.

[119] L M Branscomb, D S Burch, S J Smith and S Geltman. Photodetachment Cross Section and the Electron Affinity of Atomic Oxygen. *Phys. Rev.*, **111**:504–513, 1958.

[120] D S Burch, S J Smith and L M Branscomb. Photodetachment of O_2^-. *Phys. Rev.*, **112**(1):171–175, Oct 1958.

[121] J W Cooper and J B Martin. Electron Photodetachment from Ions and Elastic Collision Cross Sections for O, C, Cl, and F. *Phys. Rev.*, **126**:1482–1488, 1962.

[122] U Flenders, B H Nguyen Thi, K Wiesemann, N A Khromov and N B Kolokov. RF harmonic suppression in Langmuir probe measurements in RF discharges. *Plasma Sources Sci. Technol.*, **5**:61–69, 1996.

[123] M J Druyvesteyn. Der Niedervoltbogen. *Zeitschrift für Physik A Hadrons and Nuclei*, **64**:781–798, 1930.

[124] J M Anderson. Ultimate and Secondary Electron Energies in the Negative Glow of a Cold Cathode Discharge in Helium. *J. Appl. Phys.*, **31**:511–515, 1960.

[125] P A Miller, G A Hebner, K E Greenberg and P D Pochan. An Inductively Coupled Plasma Source for the Gaseous Electronics Conference RF Reference Cell. *J. Res. Natl. Inst. Stand. Technol.*, **100**:427, 1995.

[126] C Pargmann, S V Singh and H Soltwisch. A simple far-infrared laser interferometer for measuring electron densities in reactive low-temperature plasmas. *Rev. Sci. Instrum.*, **76**:113506, 2005.

[127] C Deline, B E Gilchrist, C Dobson, J E Jones and D G Chavers. High accuracy plasma density measurement using hybrid Langmuir probe and microwave interferometer method. *Rev. Sci. Instrum.*, **78**:113504, 2007.

[128] P Kempkes, F Mackel, H Stein, J Tenfelde and H Soltwisch. Electron density measurements in rapidly moving pulsed-power plasmas by means of a CO_2 laser interferometer. *Meas. Sci. Technol.*, **21**:125701, 2010.

[129] F Mackel, P Kempkes, H Stein, J Tenfelde and H Soltwisch. Electrostatic probe measurements in a pulsed-power plasma and comparison with interferometry. *Meas. Sci. Technol.*, **22**:055705, 2011.

[130] A El Saghir and S Shannon. The impact of Langmuir probe geometries on electron current collection and the integral relation for obtaining electron energy distribution functions. *Plasma Sources Sci. Technol.*, **21**:025003, 2012.

[131] J Meichsner, M Zeuner, B Krames, M Nitschke, R Rochotzki and K Barucki. Plasma diagnostics for surface modification of polymers. *Surf. Coat. Technol.*, **98**(1):1565–1571, 1998.

[132] N Mutsukura, K Kobayashi and Y Machi. Plasma sheath thickness in radio-frequency discharges. *J. Appl. Phys.*, **68**:2657–2660, 1990.

[133] S Klagge. Space- and Direction-Resolved Langmuir Probe Diagnostic in RF Planar Discharges. *Plasma Chemistry and Plasma Processing*, **12**(2):103–128, 1992.

[134] M M Becker, D Loffhagen and W Schmidt. A stabilized finite element method for modeling of gas discharges. *Comput. Phys. Commun.*, **180**:1230–1241, 2009.

[135] V A Godyak, R B Piejak and B M Alexandrovich. Evolution of the electron-energy-distribution function during rf discharge transition to the high-voltage mode. *Phys. Rev. Lett.*, **68**:40–43, 1992.

[136] A Melzer, R Flohr and A Piel. Comparison of probe measurements and emission spectroscopy in a radiofrequency discharge. *Plasma Sources Sci. Technol.*, **4**:424–431, 1995.

[137] B Eliasson and U Kogelschatz. Basic data for modelling of electrical discharges in gases: oxygen. Technical report, Brown Boveri Forschungszentrum CH-5405 Baden, 1986.

[138] J T Gudmundsson, A M Marakhtanov, K K Patel, V P Gopinath and M A Lieberman. On the plasma parameters of a planar inductive oxygen discharge. *J. Phys. D: Appl. Phys.*, **33**:1323–1331, 2000.

[139] Ph Belenguer and J P Boeuf. Transition between different regimes of rf glow discharges. *Phys. Rev. A*, **41**:4447–4459, 1990.

[140] F X Bronold, K Matyash, D Tskhakaya, R Schneider and H Fehske. Radio-frequency discharges in oxygen. I: Particle-based Modeling. *J. Phys. D: Applied Physics*, **40**:6583, 2007.

[141] K Matyash, R Schneider, K Dittmann, J Meichsner, F X Bronold and D Tskhakaya. Radio-frequency discharges in oxygen: III. Comparison of modelling and experiment. *J. Phys. D: Appl. Phys.*, **40**:6601–6607, 2007.

[142] M Geigl, S Peters, O Gabriel, B Krames and J Meichsner. Analysis and kinetics of transient species in electrode near plasma and plasma boundary sheath of rf plasmas in molecular gases. *Contrib. Plasma Phys.*, **45**:369–377, 2005.

[143] A Goehlich, T Kawetzki and H F Döbele. On absolute calibration with xenon of laser diagnostic methods based on two-photon absorption. *J. Chem. Phys.*, **108**:9362–9370, 1998.

[144] H M Katsch, A Tewes, E Quandt, A Goehlich, T Kawetzki and H F Döbele. Detection of atomic oxygen: Improvement of actinometry and comparison with laser spectroscopy. *J. App. Phys.*, **88**:6232–6238, 2000.

[145] S G Belostotsky, D J Economou, D V Lopaev and T V Rakhimova. Negative ion destruction by $O(^3P)$ atoms and $O_2(a^1\Delta_g)$ molecules in an oxygen plasma. *Plasma Sources Sci. Technol.*, **14**:532–542, 2005.

[146] M Shibata, N Nakano and T Makabe. Effect of $O_2(a^1\Delta_g)$ on plasma structures in oxygen radio frequency discharges. *J. Appl. Phys.*, **80**:6142–6147, 1996.

[147] J T Gudmundsson. Recombination and detachment in oxygen discharges: the role of metastable oxygen molecules. *J. Phys. D: Appl. Phys.*, **37**:2073–2081, 2004.

[148] A Midey, I Dotan, S Lee, W T Rawlins, M A Johnson and A A Viggiano. Kinetics for the Reactions of O^- and O_2^- with $O_2(a^1\Delta_g)$ Measured in a Selected Ion Flow Tube at 300 K. *J. Phys. Chem.*, **111**:5218–5222, 2007.

[149] A Midey, I Dotan and A A Viggiano. Temperature Dependences for the Reactions of O^- and O_2^- with $O_2(a^1\Delta_g)$ from 200 to 700 K. *J. Phys. Chem.*, **112**(14):340–3045, 2008.

[150] F C Fehsenfeld, D L Albritton, J A Burt and H I Schiff. Associative-detachment reactions of O^- and O_2^- by $O_2(^1\Delta_g)$. *Can. J. Chem.*, **47**:1793–1795, 1969.

[151] G G Arutunyan and L P Babalyants. Energetic Characteristics of Oxygen Plasma. *Contrib. Plasma Phys.*, **30**:733–747, 1990.

[152] M Tuszewski and R R White. Instabilities of Ar/SF_6 inductive plasma discharge. *J. Appl. Phys.*, **94**:2858–2863, 2003.

[153] H Kersten, U H Deutsch, M Otte, G H P M Swinkels, G M W Kroesen. Microdisperse particles as probes for plasma surface interaction. *Thin Solid Films*, **377–378**:530–536, 2000.

[154] M Mikikian, L Couedel, M Cavarroc, Y Tessier, and L Boufendi. Plasma Emission Modifications and Instabilities Induced by the Presence of Growing Dust Particles. *IEEE Transactions on Plasma Science*, **36**:1012–1013, 2008.

[155] M Mikikian and L Boufendi. Experimental investigations of void dynamics in a dusty discharge. *Phys. Plasmas*, **11**:3733–3737, 2004.

[156] M Cavarroc, M C Jouanny, K Radouane, M Mikikian und L Boufendi. Self-excited instability occurring during the nanoparticle formation in an Ar- SiH_4 low pressure radio frequency plasma. *J. Appl. Phys.*, **99**:064301, 2006.

[157] J Schulze, A Derzsi, K Dittmann, T Hemke, J Meichsner and Z Donko. Ionization by Drift and Ambipolar Electric Fields in Electronegative Capacitive Radio Frequency Plasmas. *Phys. Rev. Lett.*, **107**:275001, 2011.

[158] K Dittmann, C Küllig and J Meichsner. Electron and negative ion dynamics in electronegative cc-rf plasmas. *Plasma Phys. Control. Fusion*, **54**:124038, 2012.

[159] J L Jauberteau, G J Meeusen, M Haverlag, G M W Kroesen and F J de Hoog. Photodetachment effect in a radio frequency plasma in CF_4. *Appl. Phys. Lett.*, **55**:2597–2599, 1989.

[160] J L Jauberteau, G J Meeusen, M Haverlag, G M W Kroesen and F J de Hoog. Negative ions in a radio-frequency plasma in CF_4. *J. Phys. D: Appl. Phys.*, **24**:261–267, 1991.

List of Publications and Contributions to Conferences

Publication in Scientific Journals

2012:

K Dittmann, C Küllig, J Meichsner, "160 GHz Gaussian beam microwave interferometry in low-density rf plasmas", *Plasma Sources Sci. Technol.* **21** (2012) 024001 (7pp)

J Meichsner, K Dittmann, C Küllig, "Electron and Negative Ion Analysis in Oxygen Capacitively Coupled Radio Frequency Plasma", *Contrib. Plasma Phys.* **52** (2012) 561–570

C Küllig, K Dittmann, J Meichsner, "Detachment-induced electron production in the early afterglow of pulsed cc-rf oxygen plasmas", *Phys. Plasmas* **19** (2012) 073517

C Küllig, K Dittmann, T Wegner, I Shykin, K Matyash, D Loffhagen, R Schneider, J Meichsner, "Dynamics and electronegativity of oxygen rf plasmas", *Contrib. Plasma Phys.* **52** (2012) 836–846

K Dittmann, C Küllig, J Meichsner, "Electron and negative ion dynamics in electronegative CCRF plasmas", *Plasma Phys. Control. Fusion* **54** (2012) 124038

2011:

C Küllig, K Dittmann, J Meichsner, "Electron Density Oscillations in CC-RF Oxygen Plasma Investigated by Gaussian Beam Microwave Interferometry", *IEEE Transactions on Plasma Science,* **39** (2011) 2564-2565

2010:

C Küllig, K Dittmann, J Meichsner, "A novel approach for negative ion analysis using 160 GHz microwave interferometry and laser photodetachment in oxygen cc-rf plasmas", *Plasma Sources Sci. Technol.* **19** (2010) 065011 (10pp)

Talks at Conferences

[1] C Küllig, "Mode transitions in low pressure discharges"
DPG Spring Meeting,
25.02. - 01.03.2013, Jena, Germany

[2] C Küllig, "High and low electronegative mode in cc-rf oxygen plasmas",
3nd Graduate Summer Institute "Complex Plasmas",
29.07. - 09.08.2012, Seton Hall University, South Orange, NJ (USA)

[3] C Küllig, "Electron kinetics in 10 Hz pulsed cc-rf plasmas studied by 160 GHz Gaussian beam microwave interferometry",
DPG Spring Meeting,
11.03. - 16.03.2012, Stuttgart, Germany

[4] C Küllig, "Analysis of electron densities in low pressure rf plasmas by means of 160 GHz microwave interferometry",
XVIII. International Conference on Gas Discharges and Their Applications,
05.09. - 10.09.2010, Greifswald, Germany

[5] C Küllig, "Analysis of electron density in oxygen rf plasma by 160 GHz microwave interferometry: instabilities and laser photodetachment of negative ions",
2nd Graduate Summer Institute "Complex Plasmas",
05.08. - 13.08.2010, Greifswald, Germany

[6] C Küllig, "Time resolved analysis of electron density and instabilities in oxygen rf plasma (CCP) with 160 GHz microwave interferometry",
DPG Spring Meeting,
08.03. - 12.03.2010, Hannover, Germany

Talks at Workshops

[1] C Küllig, "Mode transitions in low pressure RF discharges",
XX. Erfahrungsaustausch, "Oberflächentechnologie mit Plasma- und Ionenstrahlprozesse",
04.03. - 08.03.2013, Mühlleithen, Germany

[2] C Küllig, "Electron and negative ion dynamics in electronegative rf plasmas",
Physics of Complex Plasmas, International Workshop, TRR24,
26.09. - 28.09.2011, Potsdam, Germany

[3] C Küllig, "Analysis of negative ion density by means of microwave interferometry and laser photodetachment",
XVIII. Erfahrungsaustausch, "Oberflächentechnologie mit Plasma- und Ionenstrahlprozessen",
08.03. - 10.03.2011, Mühlleithen, Germany

[4] C Küllig, "Zeitaufgelöste Analyse von Elektronendichten und Instabilitäten mittels 160 GHz Mikrowellen-Interferometrie",
XVII. Erfahrungsaustausch, "Oberflächentechnologie mit Plasma- und Ionenstrahl-

prozessen",
02.03. - 04.03.2010, Mühlleithen, Germany

[5] C Küllig, "160 GHz Interferometrie & Sondenmessung in O_2"
XVI. Erfahrungsaustausch, "Oberflächentechnologie mit Plasma- und Ionenstrahl-prozessen",
10.03. - 12.03.2009, Mühlleithen, Germany

Poster at Conferences

[1] C Küllig, T Wegner, J Meichsner, "Comparative electron density measurements on microwave interferometry and Langmuir probe diagnostics",
DPG Spring Meeting,
25.02. - 01.03.2013, Jena, Germany

[2] T Wegner, C Küllig, J Meichsner, "Mode transitions in inductively coupled RF discharges",
DPG Spring Meeting,
25.02. - 01.03.2013, Jena, Germany

[3] C Küllig, T Wegner, J Meichsner, "Spatially and temporally resolved plasma density in cc-rf oxygen discharge",
16. Fachtagung Plasmatechnologie (PT-16),
18.02. - 20.02.2013, Greifswald, Germany

[4] C Küllig, K Dittmann, J Meichsner, "Instabilities in a cc-rf oxygen plasma",
XXI European Conference on the Atomic and Molecular Physics of Ionized Gases (ESCAMPIG),
10.07. - 14.07.2012, Viana do Castelo, Portugal

[5] C Küllig, K Dittmann, J Meichsner, "High and low electronegativity mode in cc-rf oxygen plasma",
XXI European Conference on the Atomic and Molecular Physics of Ionized Gases (ESCAMPIG),
10.07. - 14.07.2012, Viana do Castelo, Portugal

[6] T Wegner, C Küllig, K Dittmann, J Meichsner, "Electron density measurement in cc-rf argon plasma by 160 GHz microwave interferometer and electric probe",
DPG Spring Meeting,
11.03. - 16.03.2012, Stuttgart, Germany

[7] C Küllig, T Wegner, K Dittmann, J Meichsner, "Spatio-temporal diagnostics of instabilities in cc-rf oxygen plasma",
DPG Spring Meeting,
11.03. - 16.03.2012, Stuttgart, Germany

[8] C Küllig, K Dittmann, J Meichsner, "Electron density afterglow behavior of a cc-rf oxygen discharge: Two discharge modes",
30th International Conference on Phenomena in Ionized Gases (ICPIG),
28.08. - 03.09.2011, Belfast, Northern Ireland United Kingdom

[9] C Küllig, K Dittmann, J Meichsner, "Analysis of negative ions in a cc-rf oxygen plasma by means of laser photodetachment and microwave interferometry", (*Best Poster Prize*),
30th International Conference on Phenomena in Ionized Gases (ICPIG),
28.08. - 03.09.2011, Belfast, Northern Ireland United Kingdom

[10] C Küllig, K Dittmann, J Meichsner, "Untersuchung der Elektronenkinetik in 10 Hz gepulsten cc-rf Plasmen durch 160 GHz Mikrowellen-Interferometrie mit Gaußscher Strahlführung",
DPG Spring Meeting,
28.03. - 31.03.2011, Kiel, Germany

[11] C Küllig, K Dittmann, J Meichsner, "Analyse negativer Ionen in RF-Sauerstoffplasmen durch Laser-Photodetachment und 160 GHz Mikrowelleninterferometrie mit Gaußscher Strahlführung",
DPG Spring Meeting,
28.03. - 31.03.2011, Kiel, Germany

[12] C Küllig, K Dittmann, J Meichsner, "Laser- Photodetachment and Microwave Interferometry at cc-rf Oxygen Plasmas", (*Best Poster Prize*),
15. Fachtagung Plasmatechnologie (PT-15),
28.02. - 02.03.2011, Stuttgart, Germany

[13] C Küllig, K Dittmann, J Meichsner, "Analysis of electron and negative atomic oxygen ion density by means of 160 GHz microwave interferometry and laser photodetachment in oxygen cc-rf plasma",
63rd Gaseous Electronics Conference (GEC)/ 28th Symposium on Plasma Processing (SPP)/ 7th International Conference on Reactive Plasmas (ICRP),
04.10. - 08.10.2010, Paris, France

[14] C Küllig, K Dittmann, J Meichsner, "Analyses of electron densities with 160 GHz microwave interferometry and measurement of negative ion density by additional laser photodetachment technique",
XX European Conference on the Atomic and Molecular Physics of Ionized Gases (ESCAMPIG),
13.07. - 17.07.2010, Novi Sad, Serbia

[15] K Dittmann, C Küllig, J Meichsner, "160 GHz microwave interferometry for oxygen rf plasma (CCP) diagnostics",
DPG Spring Meeting,
30.03. - 02.04.2009, Greifswald, Germany

Danksagung

Bei Herrn Professor Dr. Jürgen Meichsner möchte ich mich für die Möglichkeit bedanken, in seiner Arbeitsgruppe diese Promotionsarbeit anzufertigen. Weiterhin gilt Ihm mein Dank, für eine sehr gute allgemeine und insbesondere fachliche Betreuung und die damit einhergehende Unterstützung während der gesamten Promotionszeit.
Ein ganz besonderer Dank gilt, Dr. Kristian Dittmann, der mich immer tatkräftig unterstützte, beriet und mir stets helfend zur Seite stand. Mit Ihm werde ich immer eine ganz besondere und erfolgreiche Zusammenarbeit und ein persönlich sehr wertvolles Verhältnis verbinden.
Peter Druckrey und Uwe Meißner schufen mit Ihrem technischen Sachverstand und Ihrer Tatkraft erst die Grundlage für die in dieser Promotion erarbeiteten Ergebnisse. Ohne Ihre Hilfe und Unterstützung, auch über das rein fachliche hinweg, wäre diese Arbeit so nicht möglich gewesen. Dafür bedanke ich mich ganz herzlich bei beiden.
Sebastian Nemschokmichal danke ich für die große Unterstützung hinsichtlich Anregungen, fachlichem Rat und zahlreichen kritischen Kontrollen und Korrekturen während der gesamten Promotionsphase. Diese brachten mich immer ein Stück weiter. Ebenfalls für den sehr wichtigen Ausgleich mit dem runden Sportgerät stand er immer zur Verfügung.
Danken möchte ich ebenfalls Thomas Wegner, der mir während des Zeitraumes der Anfertigung der Promotionsarbeit mit seiner Arbeit im Labor den Rücken frei hielt.
Bei den Kollegen, Marc Bogaczyk und Robert Wild aus dem Raum A209 möchte ich mich für die sehr gute Zusammenarbeit und Unterstützung, sowie die zahlreichen erheiternden und aufbauenden Momente, bedanken.
Abschließend möchte ich mich ganz besonders bei meiner Freundin Eileen Arndt bedanken, die immer für mich da ist, mich unterstützt und mit mir durch dick und dünn geht, auch wenn man dafür 60 m Seil benötigt.

Danke

Eileen Arndt, Oliver und Anne Arndt, Marc Bogaczyk, Vladimir Danilov, Kristian Dittmann, Peter Druckrey, Susanne Joost, Bert Krames, Peter Küllig, Jürgen Meichsner, Uwe Meißner, Vera Müller, Sebastian Nemschokmichal, Ralf Schneider, Holger Spahr, Lars Stollenwerk, Holger Testrich, Hans-Erich Wagner, Thomas Wegner, Frank Wienholtz und Robert Wild

... und allen, die ich vielleicht noch vergessen habe.